Journal of Structural Geology 126 (2019) 357–392

Contents lists available at ScienceDirect

Journal of Structural Geology

journal homepage: www.elsevier.com/locate/jsg

Opposite shear senses: Geneses, global occurrences, numerical simulations and a case study from the Indian western Himalaya

Dripta Dutta, Soumyajit Mukherjee*

Department of Earth Sciences, Indian Institute of Technology Bombay, Powai, Mumbai, 400 076, Maharashtra, India

ARTICLE INFO

Keywords:
Shear zone kinematics
Deformation mechanism
Ductile and brittle deformation of rocks
Basin inversion

ABSTRACT

Opposite shear sense (OSS) is manifested by the presence of conflicting shear sense indicators in a portion of a rock body, a shear/fault zone or across several parallel shear/fault zones. More importantly, the scale of observation may range from micro-to regional. Several terms have been used by previous workers to refer OSS, viz. conflicting shear senses, reverse shear, shear sense reversal/inversion, slip reversal/inversion, kinematic reversal, etc. Although OSS has been reported from several terrains worldwide, a review on the mechanisms and global distribution remained due. Given that shear sense indicators play a crucial role in deciphering the deformation history of a region, the presence of OSS sometimes baffles structural geologists.

In this article, we present a catalogue of 59 reports of OSS in ductile and brittle regimes from 56 locations globally, from collisional, extensional and strike-slip tectonic settings besides a few cratons, and provide the possible reasons/mechanisms proposed by the workers for each one of them. Though we primarily discuss OSS with parallel shear planes, six reports of OSS with non-parallel shear planes are also included. The origin of OSS can be attributed to either single (either ductile/brittle) or multiple (both ductile/both brittle/ductile followed by brittle) deformation phases. Most of the occurrences listed here have arisen due to multiple deformation phases, almost half of which owe their genesis to reorientation of the principal stress axes temporally. Gravitational collapse of over-thickened crust also produces OSS, especially at the orogens. Besides, less than a quarter of all the compiled examples originate during single-stage deformation by coaxial shortening, heterogeneity in strain-rate and viscosity, isoclinal folding, rotation of blocks within shear zones or differences in shortening/stretching rates across the fault/shear zone. The majority of the OSS documented so far and compiled in this study, cluster within or close to few orogens. We speculate two possibilities: *(i)* complex tectonics, and *(ii)* richness in the number of research studies undertaken in these terranes. Although orthogonal switch (~NW–SE → ~ NE-SW) of the compressive stress axes (σ_1) has been discussed for the Zagros fold-thrust belt (ZFTB) in the Paleogene, OSS has not been reported from here so far. The same holds true for the Andes that collapsed gravitationally and switched compression from~ E-W into ~ N–S in the Mid-Miocene. Reactivation of pre-Andean extensional faults as thrusts are described by previous workers, but not referred to produce OSS. Positive inversion-reverse reactivation of pre-existing extensional faults-such as those reported from the Andes and the Apennines, can either be beneficial or disadvantageous to the preservation of the hydrocarbon of the region. Identification of inversion structures would be important in hydrocarbon reserve appraisal.

Time-dependent numerical simulations using COMSOL Multiphysics v5.4 predict variation in the sense and amount of rotations of the elliptical inclusions across the matrix. However, the competency contrast between the matrix and the inclusions do not seem to affect this variation. We also provide an original report of OSS in ductile regime as observed under an optical microscope from the Lesser Himalayan rocks of the Chaura region (Himachal Pradesh state, India). Although a temporal relation between the two shear senses, in this case, could not be established owing to the absence of cross-cut relations of shear fabrics, we speculate dominance of coaxial deformation could have resulted in the near-equal abundance of OSS.

* Corresponding author.
E-mail addresses: dripta.dutta@gmail.com (D. Dutta), soumyajitm@gmail.com, smukherjee@iitb.ac.in (S. Mukherjee).

https://doi.org/10.1016/j.jsg.2019.05.008
Received 23 April 2019; Received in revised form 28 May 2019; Accepted 28 May 2019
Available online 25 June 2019

List of abbreviations

BSE	Back-scattered electron
CPO	Crystallographic Preferred Orientation
DCZJ	Dextral Closing Zipper Junction
DOZJ	Dextral Opening Zipper Junction
HGR	High-grade rocks
HHC	Higher Himalayan Crystallines
HP	High pressure
LGR	Low-grade rocks
LHS	Lesser Himalayan Sequence
LKRW	Larlji-Kulu-Rampur Window
MCT_L	Main Central Thrust Lower
PCZJ	Pure Closing Zipper Junction
POZJ	Pure Opening Zipper Junction
OOST	Out of Sequence Thrust
OSS	Opposite Shear Sense
SCZJ	Sinistral Closing Zipper Junction
SOZJ	Sinistral Opening Zipper Junction
SPO	Shape Preferred Orientation
THS	Tethyan Himalayan Sequence
UHP	Ultra-high pressure
VPP	Vorticity Profile Plane
WGC	Wangtu Gneissic Complex
ZFTB	Zagros Fold and Thrust Belt

List of symbols

σ_1	maximum principal stress axis
σ_2	intermediate principal stress axis
σ_3	minimum principal stress axis
μ	dynamic viscosity
ω	flow vorticity
U_1	velocity of upper boundary of a shear zone/channel
U_2	velocity of lower boundary of a shear zone/channel
$\partial P/\partial x$	Pressure (P) gradient along the X-direction
θ	dip amount of shear zone/channel
d	density of rocks
g	aceeleration due to gravity
y_0	thickness of subduction channel

1. Introduction

Kinematic indicators are structures that help structural geologists to construe the type of deformation of the rocks e.g., coaxial and non-coaxial, during the now frozen progressive deformation. Ductile shear-sense indicators, on the other hand, represent a set of kinematic indicators that signify the sense of non-coaxial deformation (Sander, 1911; Hanmer and Passchier, 1991), or in a technical term the “flow vorticity” or the “shear induced vorticity” (Means et al., 1980). Similarly, there are structures found in brittle shear zones that denote the sense of non-coaxiality (see Passchier, 1984; Petit, 1987; Doblas, 1998; Blenkinsop, 2002; Bigi, 2006, Mukherjee, 2012a,b, etc.). These have been widely used to deduce the sense of displacement viz. sinistral (left-lateral), dextral (right-lateral), normal and reverse in both ductile and brittle shear zones, that has decoded the tectonic history of the respective terranes (White et al., 1986; Petit, 1987; Passchier and Simpson, 1986; Bell and Johnson, 1992; Passchier and Trouw, 2005; Passchier and Coelho, 2006; Mukherjee, 2011, 2013a,b; Fossen, 2016). However, one must identify several such structures (Ramsay and Lisle, 2000) before concluding the dominant/bulk shear sense. Studying ductile and brittle shear zones’ kinematics is a fundamental exercise in structural geology since it is of great importance in earthquake and plate tectonic studies (Regenauer-Lieb and Yuen, 2003).

Several asymmetric shear sense indicators have been described and utilized by previous workers to study ductile (e.g., asymmetric boudins, mantled porphyroclasts, etc.) as well as brittle (e.g. slickenlines, secondary shear fractures, etc.) shear zones (Table 1; Figs. 1 and 2 see Fig. S1 in the supplementary file S2). Numerical models by Giorgis and Tikoff (2004) show that the shape fabric of a set of rigid porphyroclasts depends upon the non-coaxiality of the flow as well as the aspect ratio of individual porphyroclasts. Moreover, the authors also demonstrate that the shape preferred orientation (SPO) of the rigid strain markers do not unequivocally show the true shear sense because of lack of direct correlation between the strain and fabric ellipsoids, especially at high strains. Likewise, Kilian et al. (2011) report that the shape fabric of the quartz aggregates defined by the obliquity of the long axes of the quartz grains to the shear plane does not necessarily represent the bulk shear sense. The torsion experiments of Pieri et al. (2001) on calcite mylonites exhibit similar results. Although Menegon and Pennacchioni (2010), report quartz SPO aligned both antithetic and synthetic to the bulk shear direction, there are cases where the shear senses obtained from the oblique shape fabric of the grains matches with those determined through various kinematic indicators as well as CPO studies viz., van der Wal et al. (1992), Froitzheim et al. (1997), Stöckhert and Duyster (1999), Romeo et al. (2007), Xypolias et al. (2013), Spanos et al. (2015), Puelles et al. (2018) etc. Galadí-Enríquez et al. (2006) suggest that quartz SPO can preserve low-strain deformation increments, and hence could possibly aid in construing late-stage shear reversal. However, the authors also emphasize that it should be considered along with other shear indicators.

Before trying to decipher the shear sense, a geologist must choose the plane of observation that corresponds to the XZ section in the context of ductile deformation, i.e. parallel to the shear direction and perpendicular to the primary shear C-plane, of the strain ellipsoid. The XZ-section is also called the ‘*vorticity profile plane*’ (VPP) (Fig. 3) (Robin and Cruden, 1994; Passchier and Simpson, 1986; Passchier, 1998; Michels et al., 2015). In brittle shear zones, the plane of observation should be parallel to the slickenline (Grasemann et al., 2012) and perpendicular the primary shear Y-plane (or the D-plane: Ghosh, 1993). Shear senses documented from any other plane can be misleading (Hanmer and Passchier, 1991; Cladouhos, 1999; Blenkinsop, 2002; Passchier and Trouw, 2005; Bigi, 2006; Fossen and Cavalcante, 2017). It is generally assumed that the shear plane and the shear direction are parallel to the mylonitic foliation and the stretching lineation, respectively. However, these assumptions are invalid *(a)* at low shear strain, and *(b)* for pure shear-dominated transpression. In the second case, the stretching lineation and the shear direction may even be orthogonal (high strain shear zones may deform with a triclinic flow symmetry such that the lineations are oblique to the shear direction/VPP, see Passchier and Coelho (2006); Iacopini et al. (2007)) (Tikoff and Fossen, 1993). In such scenarios, one may find XZ-sections to be dominated by symmetric structures rarely denoting shear sense (Mukherjee, 2017 and references therein). Rocks may sometimes be devoid of stretching lineations, and Anisotropy Magnetic Susceptibility measurements of such samples can be utilized to identify the XZ-section (Goswami et al., 2018). Besides, sample preparation techniques can also render Riedel shear planes unrecognizable and thus greatly affect the understanding of micro-scale brittle shear kinematics (Aiyama et al., 2019).

Majority of the studies on shear fabrics and their geodynamic relevance focus on metamorphic low-grade rocks (LGR), possibly because of the features are better preserved. On the other hand, ductile flow partitioning for high-grade rocks (HGR) occurs on a much larger scale owing to dominant creep mechanisms and grain boundary migration. Moreover, unlike LGR, the deformation is pervasive, and hence overprinting is widespread (Trouw et al., 2010). Consequently, signatures of earlier deformation phases are largely lost. Besides, shear sense

Table 1
Summary of various shear sense indicators for both ductile and brittle deformation regimes (Figs. 1 and 2) (supplementary Fig. S1).

Deformation regime	Sl. no.	Author	Terrane/General concept (GC)	Shear sense indicators	Approach (**Ag**: Analog Model; **An**: Analytical Model; **F**: Field-based; **M**: Microscopic study; **N**: Numerical Model; **R**: Review; **S**: Satellite imagery)
DUCTILE (Fig. 1)	1	Etchecopar (1977)	GC	Asymmetric boudins	N
	2	Bouchez et al. (1983)	GC	Shape fabric asymmetry	R
	3	Lister and Snoke (1984)	GC	S–C fabrics, Mica Fish, and Quartz CPO	F, M
	4	Hanmer (1986)	Western Churchill and Grenville Provinces (Candian Shield)	Asymmetrical pull-apart (boudins, pinch & swell structures) and foliation fish	F, Ag
	5	Passchier and Simpson (1986)	French Pyrennees and Santa Rosa (California, USA)	σ- & δ-type porphyroclast systems	M, Ag
	6	White et al. (1986)	GC	Rotated foliation and markers, intrafolial folds, S–C farics, domino structure, mantled porphyroclasts, quartz SPO and CPO, mineral fish	R
	7	Hanmer and Passchier (1991)	GC	Sigmoid foliations, S–C fabric, winged inclusion, asymmetic boudins, mica fish, pressure shadows, quarter structures, deformed veins, tension gashes, asymmetric folds	R
	8	Simpson and De Paor (1993)	Pinaleno Mountains, Arizona (USA)	Mantled porphyroclasts (σ- & δ-type)	R, An
	9	Shelley (1995)	GC	Mineral SPO	M
	10	Koehn and Passchier (2000)	Orbic Alps (northern Italy)	Striped bedding-veins	F
	11	Grasemann and Stüwe (2001)	Schober (Austria), Naxos (Greece), Vintschgau (Italy), Sutlej Valley (India), and Kalak Nappe Complex (Norway)	Flanking folds	F, N
	12	Goscombe and Passchier (2003)	Kaoko Belt (Namibia), Arunta Block (Central Australia) and Adelaidean Fold Belt (South Australia)	Asymmetric boudins	F
	13	ten Grotenhuis et al. (2003)	GC	Mineral Fish	M
	17	Trouw et al. (2010)	GC	Mantled porphyroclasts, S–C fabrics, oblique foliations, mineral and foliation fish, asymmteric folds, quarter folds, and strain shadows	M, R
	14	Passchier and Trouw (2005)	GC	Quartz CPO, crenulation cleavages, asymmetric folds, quarter structures, mantled porphyroclasts, oblique foliations, deformed veins, pressure fringes, mineral fish, asymmetric boudins, flanking structures, porphyroblast inclusion trails	R
	15	Passchier and Coelho (2006)	Ticino (Switzerland), Cadaques (NE Spain), Pilbara (Australia), southern Minas Gerais (Brazil), and Rio (Brazil)	Shear bands, asymmetric boudins, mineral fish, mantled porphyroclasts, strain shadow, flanking structures, tension gashes, folded & boudinaged veins	F, M
	16	Cosgrove (2007)	GC	Asymmetric folds, pinch & swell structures, kink bands, tension gashes, en-echelon veins, and S–C fabrics	R
	17	Trouw et al. (2010)	GC	Mantled porphyroclasts, S–C fabrics, oblique foliations, mineral and foliation fish, asymmteric folds, quarter folds, and strain shadows	M, R
	18	Mukherjee (2011)	Karakoram Metamorphic Complex (NW Himalaya, India)	Mineral fish	M, R
	19	Mukherjee et al. (2015)	Higher Himlayan Shear Zone (NW India)	Intrafolial folds	R
	20	Grasemann et al. (2019)	GC	Flanking structures, domino & shear band boudins, winged inclusions	F, N, R
	21	Scharf et al. (2019)	Oman mountains	PDT (Pul-apart, Drag fold, thrust) and dragged intergrowth	F, M
	21	Tjia (1964)	Lokulo Area (Java, Indonesia)	Slickenlines, steps, grooves, ridges	F

(*continued on next page*)

Table 1 (*continued*)

22	Petit (1987)	GC	Secondary shear fractures (T, M, P, R, R′)	F	
23	Ramsay and Huber (1987)	Sierra Nevada (California, USA)	Curved slickenfibers	F	
24	Olson and Pollard (1991)	GC	En-echelon fractures	N	
25	Tanaka (1992)	Akaishi Tectonic Line (Japan)	Cataclastic lineations, slickenlines	F	
26	Hippertt (1993)	Moeda Bonfim Shear Zone (Brazil)	V-pull apart	M	
27	Rajlich (1993)	GC	Riedel Shear	R	
28	Doblas (1998)	GC	Slickenside features: Crescentic markings, steps, fractures, secondary shear fractures, trailed material, asymmetric elevations, deformed elements, asymmetric plan-view features	R	
29	Davis et al. (2000)	Cottonwood and Sheets Gulch Area (Utah, USA)	Riedel Shear	F	
30	Samanta et al. (2002)	GC	Pull-apart microstructures	Ag	
31	Katz et al. (2004)	Capitol Reef National Park (Utah, USA)	Riedel Shear	F, An	
32	Passchier and Trouw (2005)	GC	Shear fractures (Y, P, R, R′, T, M)	R	
33	Mukherjee (2012a)	Higher Himalayan Shear Zone (NW India)	Trapezoidal mica grains	M	
34	Misra et al. (2014)	Western Deccan Region (India)	Brittle shear fractures, slickenfibers, asymmetric elevations	F	
35	Fossen (2016)	GC	Shear fractures (Y, P, R, R′), domino structures	R	
36	Dasgupta and Mukherjee (2017)	Barmer Basin (W India)	Shear fractures (Y, P, R, R′, T, M), steps on slickensides	F	
37	Mattern and Scharf (2018)	Oman Mountains (Oman)	Riedel Shear, curved slickenlines	F	
38	Dasgupta and Mukherjee (2019)	Barmer & Kutch Basins (W India)	Displaced lineaments	S	

indicators for HGR are much more prominent than those in the LGR, and often the feature is only partly preserved. Identifying the VPP in the field also poses a challenge! Hence, whereas the low-grade terranes with isolated outcrops reveal enough tectonic information, their high-grade counterparts may not. To unveil the deformation history of high-grade terranes, the structural features from multiple outcrops should, therefore, be correlated (Passchier et al., 1990; Passchier and Coelho, 2006).

2. Research objectives and significance

Opposite shears can be deciphered from opposite slip sense displayed by the same or different kinematic indicators. Unlike superposed folding (also referred as “folding interference” and “refolding” in the literature), which has been classified and studied in great detail (e.g., Neves et al., 2018), a similar concise effort for superposed shear (or “reshear”) under a single platform remained due even though it has been reported from several terranes worldwide (Section 6). Surprisingly, this is despite the origin of contradictory slip senses has been debated for over three decades (e.g., Bell and Johnson, 1992; Passchier and Williams, 1996; Kilian et al., 2011).

The need for such a catalogue for OSS is two-fold:

(a) *Decoding geodynamic evolution*: Field geologists will be able to decipher plausible explanation(s) for the OSS that they might encounter at meso- and micro-scale, by comparing their findings with those reviewed in this article. Once the OSS are identified as single or multi-deformational (Section 4), further inferences viz., coaxiality of deformation, the role of isostasy or alteration of the stress regime can also be made. Such a piece of information can logically explain the otherwise puzzling deformation history.

(b) *Hydrocarbon appraisal*: Identification of OSS in sedimentary basins (using null points; Section 4.2.1) often indicate episode(s) of tectonic inversion, which, along with the arrangement of faults and fractures, play a pivotal role in the appraisal of hydrocarbon exploration (Section 8) e.g., re-distribution of hydrocarbon traps to shallower depths, increase in permeability of tight sandstones due to uplift-induced fracturing. (Corcoran and Doré, 2005; Henriksen et al., 2011). The offset of markers across faults coupled with apatite-fission track dating of the rocks can provide near-accurate estimates of the rate of uplift, which, if too rapid, can endanger hydrocarbon preservation (Henriksen et al., 2011).

In this study we aim to *(i)* list the mechanisms that produce OSS (Section 4), *(ii)* review globally reported ductile and brittle OSS in mega-, meso- and micro-scales (supplementary file S1), and *(iii)* comment on the common tectonic scenarios that result in OSS (Section 8). In a specific case, *(iv)* we report OSS from the schistose rocks of the Sutlej Valley (near Chaura, Himachal Pradesh, India) of western Lesser Himalaya (Section 7).

3. Opposite shear senses: definition and precautions

A body of rock is said to exhibit OSS when conflicting slip sense occurs at some portion of the rock (Hippertt and Tohver, 1999). Terms such as contradictory/conflicting shear senses, or reverse shear, kinematic reversal, can also be found in the literature (Passchier and Williams, 1996; Blenkinsop, 2002; Koyi et al., 2013). Besides, ‘shear sense reversal’, ‘slip reversal’, ‘shear sense inversion’ or ‘slip sense inversion’ also exist, e.g., Tavarnelli (1999), Michibayashi et al. (2000), Mattern (2001), Scisciani et al. (2002), Hsiao et al. (2004), Sawaguchi (2004), Mukherjee (2007), Kodaira et al. (2014), Javadi et al. (2015). At this point, the question remains: what percentage of OSS should be considered significant? The answer is subjective. However, we believe that the presence of even a single OSS indicator should be scrutinized from a geoscientific perspective rather than being treated as an

Table 2
Summary of models/processes that can produce OSS (Figs. 9–23).

Deformation stages	Process	Section no.	Fig(s). no.	Scale of observation	Key references
SINGLE (Figs. 9–15)	Fracturing of a layered body	4.1.1	9	This is a result of numerical modelling, hence scale of observation cannot be established unequivocally.	Cooke and Underwood (2001)
	Ductile deformation of a layered body with heterogeneous rheologies	4.1.2	10,11	This is a result of numerical modelling, hence scale of observation cannot be established unequivocally. However, Hippertt & Tohver (1999), and Langille et al. (2010) support the feasibility of the mechanism at micro- and orogen scale, respectively.	Lister and Williams (1983), Treagus (1983), Ishii (1992), Hippertt and Tohver (1999)
	Back-rotation under sub-simple shear regime	4.1.3	12	Meso- to mega-scale	Ghosh and Ramberg (1976), Passchier and Simpson (1986), Simpson and De Paor (1993), Marques et al. (2007), Fossen and Cavalcante (2017)
	Block rotation under simple shear	4.1.4	13	Meso- to mega-scale	MacLeod and Murton (1995),
	Folding	4.1.5	14	Micro- to meso-scale	Bell and Johnson (1992), Ghosh (1993), Goscombe and Trouw (1999), Twiss and Moores (2007), Bastida et al. (2014), Sengupta and Chatterjee (2015), Fossen (2016)
	Zipping of ductile shear zones	4.1.6	14	Mega- to meso scale	Platt and Passchier (2016), Passchier and Platt (2017)
	Differential stretching of faulted wall rocks	4.1.7	15	Meso- to mega-scale	Means (1989, 1990)
MULTIPLE (Figs. 16–23)	Fault reactivation/Inversion tectonics	4.2.1	16,17,18	Meso- to mega-scale	De Paor and Eisenstadt (1987), Cooper et al. (1989), Williams et al. (1989), Wennberg (1996), Holdsworth et al. (1997), Tavarnelli (1999), Turner and Williams (2004) and references therein, Bigi (2006), Cooper and Warren (2010)
	Subduction & Exhumation	4.2.2	19,20	Mega-scale	Brueckner and Cuthbert (2013) and references therein, Godin et al. (2006) and references therein
	Tilting & Overturning	4.2.3	21	Mega-scale	Lim and Cho (2012)
	Gravitational collapse	4.2.4	22	Mega-scale	Bell and Newman (2006), Bell and Sapkota (2012)
	Isostatic adjustments	4.2.5	23	Mega-scale	Wernicke and Axen (1988)

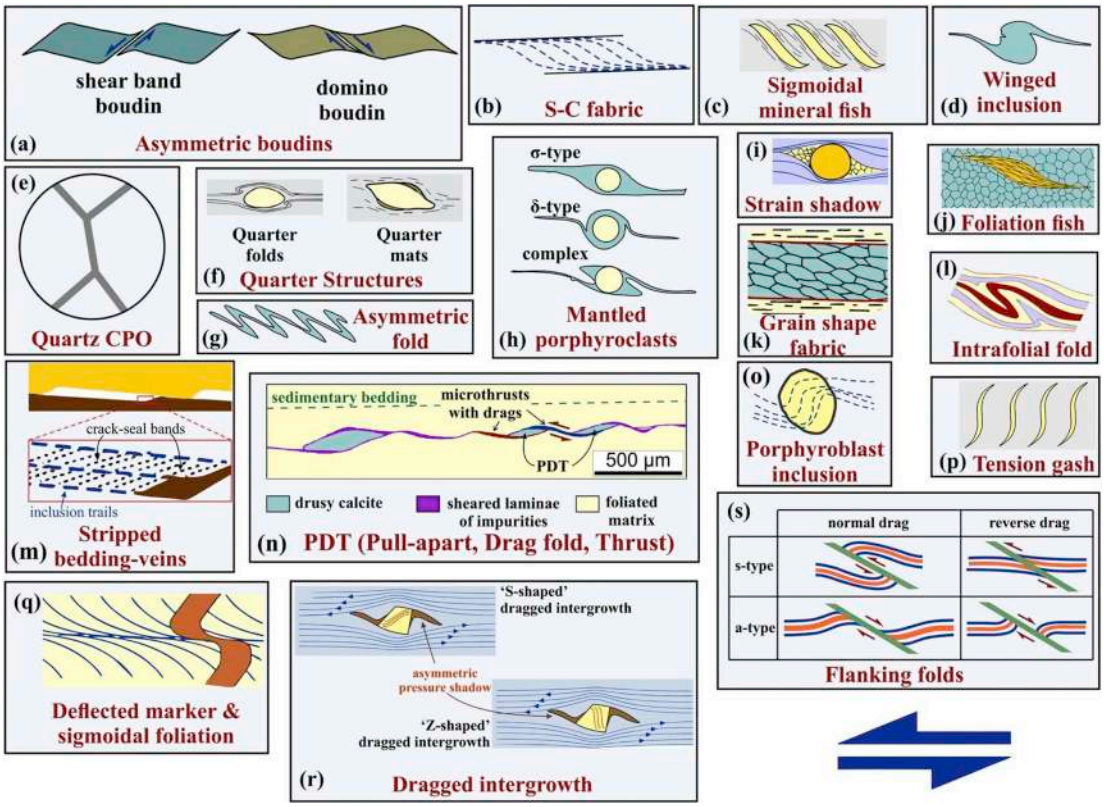

Fig. 1. Major ductile shear sense indicators observed at meso- and micro-scale (first referred at Section 1). Reproduced from (a) fig. 5c of Goscombe et al. (2004), fig. 4c of Grasemann et al. (2019), (d) fig. 2 of De Paor and Eisenstadt (1987), (f) fig. 5.38 of Passchier and Trouw (2005), (h) fig. 5.21 of Passchier and Trouw (2005), (i) fig. 9.7.13 of Trouw et al. (2010), (j) fig. 9.5.2 of Trouw et al. (2010), (k) fig. 10a of Xypolias (2010), (l) fig. 12.2c of Mukherjee et al. (2015) (m) fig. 10a of Koehn and Passchier (2000), (n,r) figs. 9 and 11d of Scharf et al. (2019), (o) fig. 5.80 of 2018, (p) fig. 8a of Fossen and Cavalcante (2017), (q) fig. 9.1 of Trouw et al. (2010), (s) fig. 1 of Grasemann et al. (2003). Shear sense: sinistral (blue half-arrows). Examples: (a) figs. 5 and 6 of Goscombe and Passchier (2003),(b) fig. 9.3.3 of Trouw et al. (2010), (c) fig. 9.5.3 of Trouw et al. (2010), (d) fig. 2 of Grasemann and Dabrowski (2015), (e) fig. 8 of Little et al. (2013), (f) fig. 9.7.11 of Trouw et al. (2010), fig. 3d of Larson (2018), (g) fig. 12.4 of Trouw et al. (2010), (h) fig. 9.1.5, 9.2.3 & 9.2.17 of Trouw et al. (2010), (i) fig. 6.12 of Trouw et al. (2010), (j) fig. 9.3.17 of Trouw et al. (2010), (k) fig. 9.5.11 of Trouw et al. (2010), (l) fig. 9.6.4 of Trouw et al. (2010), (m) fig. 4 of Koehn and Passchier (2000), (n) figs. 6 and 8 of Scharf et al. (2019), (o) fig. 5.89 of Vernon (2018), (n) fig. 1 of Lisle (2013), (q) fig. 4d of Mancktelow and Pennacchioni (2005), (r) fig. 11 of Scharf et al. (2019), (s) fig. 6 of Grasemann and Stüwe (2001), fig. 2 of Passchier (2001), figs. 8 and 9 of Grasemann et al. (2003), fig. 9 of Exner et al. (2004).

insignificant outlier. Shear sense indicators have been documented from a wide variety of scales (mega scale: Zhang and Cunningham (2012) (location no. 47 in Fig. 24, supplementary file S1), meso-scale: Fossen (2016), microscale: Passchier and Trouw (2005), and sub-microscopic scale: Back-scattered electron (BSE) image: fig. 6a in Rekha et al., 2014). Therefore, reverse shear can be expected at any of these scales. However, in the course of this review, we did not come across a case of OSS reported from BSE images.

Taking examples from Lewisian Gneiss Complex (Scotland), Wheeler (1987) emphasizes that the orientation of the pre-existing planar fabrics relative to that of the later shear direction is crucial (also see concept 5.1 A in Bose and Mukherjee, 2017). The resulting arrangement might indicate incorrect shear sense to a novice. Two more examples have been reported from Robbies Well Pluton and Mulgandinnah Shear Zone (Western Australia) by Passchier and Williams (1996). These authors further note that deflection of pre-existing planar fabrics by late-stage shear zones is not reliable as kinematic indicators (Fig. 4, Passchier and Coelho, 2006) unless the line of intersection of the planar feature and the shear zone are perpendicular to the stretching lineation. Structures produced in all other cases bear a triclinic or lower symmetry that may exhibit a shear sense opposite to that of the bulk shear.

The geometry of an 'a-type' flanking fold showing normal drag resembles that of a shear band (Figs. 1s and 5a, Grasemann et al., 2003; also see review in Mukherjee, 2014a), but the bulk shear that produces them are oppositely directed. Similar confusion may also arise while inferring shear senses from shear band and domino boudins (Fig. 1a). Moreover, asymmetric boudins at a high angle (>45°) to the shear plane are not reliable shear sense indicators (fig. 7 of Goscombe and Passchier, 2003; Dabrowski and Grasemann, 2019).

Tension gashes or extensional veins develop under a non-coaxial deformation regime. They tend to rotate after formation, and consequently, attain a sigmoidal geometry (Fossen, 2016), similar to that of a mineral fish. However, as indicated in Fig. 5e and f, they denote opposite shear senses. Such a similarity in geometries is also exhibited by an S–C fabric and the inclusion pattern inside a poprphyroblast such as garnet (Fig. 5g and h). But again, these two indicate opposite shear sense. However, the indicated shear sense for the garnet porphyroblast (Fig. 5h) holds true only if the garnet has rotated. Otherwise, both the S–C fabric and the inclusion trails within the porphyroblast exhibit identical shear senses (Passchier & Speck, 1994). Again, whether a porphyroblast has undergone rotation or not should be inferred keeping in mind the regional/dominant shear sense (see box 7.4 in Passchier and Trouw, 2005). Hence, if the shear sense indicated by the S–C fabric (Fig. 5g) is compatible to the regional one, and if any other shear sense indicator is absent, the porphyroblast must be considered as non-rotational, which in turn would imply absence of OSS.

It is also essential to correctly identify the marker bed before deciphering the sense of movement across a fault using the drag pattern (Fig. 5i,j1,j2; see review in Mukherjee, 2014a). Grasemann et al. (2003), based on analytical studies, propose that reverse drags develop when the acute angle between the fault and the undeformed marker

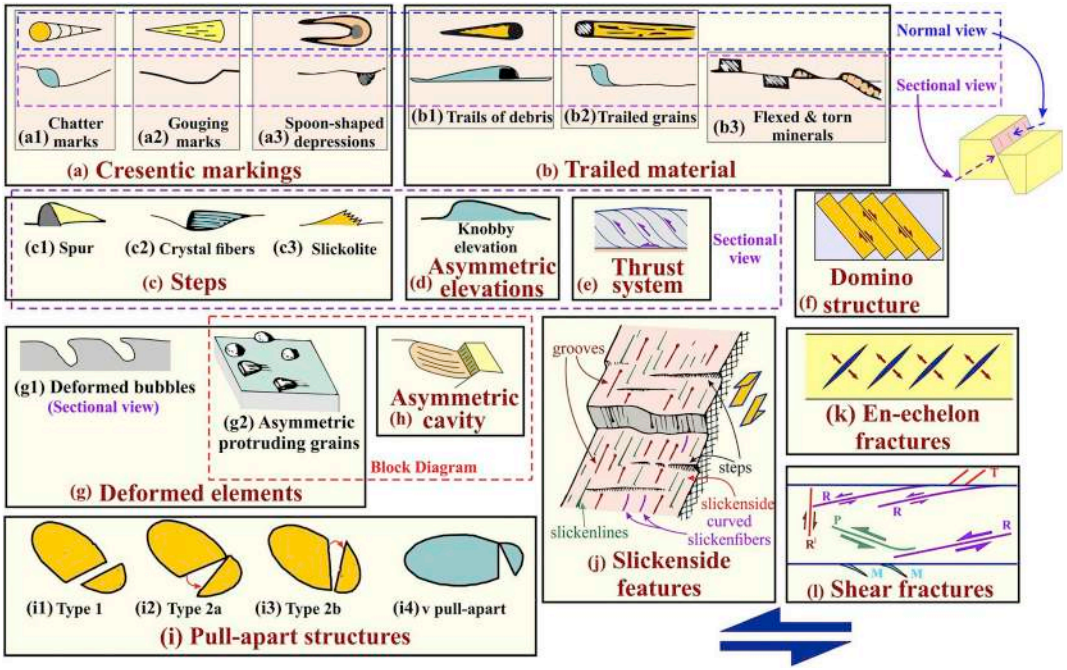

Fig. 2. Major brittle shear sense indicators observed at different scales (first referred at Section 1). Reproduced from (a,b,c,d,g,h) fig. 1 of Doblas (1998), (i1,i2,i3) fig. 4 of Samanta et al. (2002), (i4) fig. 1 Hippertt (1993), (j) fig. 3 of Tjia (1964), fig. 6 of Twiss and Gefell (1990), (l) fig. 1c of Petit (1987), Fig. 5.50 of Passchier and Trouw (2005). Shear sense: sinistral (blue half-arrows) except for (j) for which the relative sense of movement of the blocks have been denoted separately. Normal view: viewing direction perpendicular to the slickenside. Sectional view: viewing direction perpendicular to the plane normal to the slickenside but parallel to the slickenline. Also see the following figures by previous workers for the corresponding features: (a) fig. 2 of Phillipson (2003), figs. 6 and 7 of Engelder et al. (2004), fig. 4c of Wiatr et al. (2013), (b2) fig. 9d of Sümer (2015), (c) fig. 5a of Laurich et al. (2014), fig. 6e of Samant et al. (2017), (d) fig. 4f of Wiatr et al. (2013), fig. 8 of Misra et al. (2014), (e) fig. 4b of Doblas et al. (1997a), (f) fig. 5.43 of Passchier and Trouw (2005), (g2) fig. 4a of Doblas et al. (1997b), (h) fig. 4g of Wiatr et al. (2013) (i1) fig. 8c and d of Sarkarinejad and Azizi (2008), fig. 5d of Bose et al. (2018), (i2-i4) fig. 6e of Roy et al. (2010), fig. 5d of Joshi et al. (2017), (j) fig. 8 of Twiss and Gefell (1990), fig. 10c of Zhang et al. (2011), figs. 4b,c,d of Samant et al. (2017), (k) fig. 8.30 of Fossen (2016), (l) fig. 2 of Dresen (1991), fig. 8 of Katz et al. (2004).

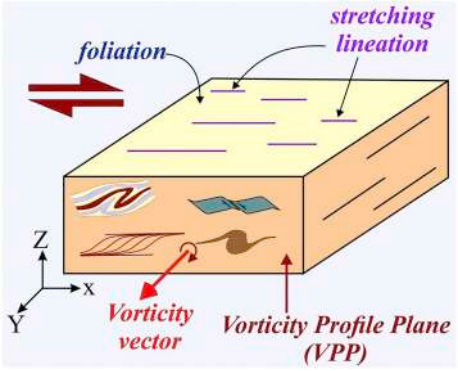

Fig. 3. Schematic diagram illustrating the vorticity profile plane (VPP) and the vorticity vector for a dextral shear sense (first referred at Section 1).

i.e., $\alpha > 30^{\circ}$. In the example of a flanking structure with reverse drag (also see figs. 18 and 19 of Mukherjee (2014a)) shown in Fig. 5k1, k2, $\alpha = 70^{\circ}$, thus substantiating the claims of Grasemann et al. (2003). Pre-existing foliations deflect by a late-stage deformation along a shear zone (Pennacchioni and Mancktelow, 2018), and develop a sigmoid-geometry. Such features also help to identify the shear sense (Fig. 5l1,l2). Such features should be carefully interpreted and must not be confused with drag patterns observed across faults as shown in Fig. 5j1,j2. On a mega-scale, a strike-slip asymmetric pull-apart basin also exhibits a sigmoidal shape. However, while deciphering the shear sense, it must not be confused with the geometry of a mineral fish (compare Fig. 5f,m1,m2). Scharf et al. (2019) report two new ductile shear sense indicators 'PDT' (pull-apart, drag fold, thrust) (Fig. 5n) and 'dragged intergrowths' (Fig. 5o1,o2). The geometry of the former is similar to that of the shear band boudin (Fig. 5c), but they are products of opposite shear senses (compare Fig. 5c,n). The authors further emphasize that: *(i)* individual boudins are made up of deformed rocks, whereas PDTs are usually filled with calcitic cement, and (ii) PDTs are separated by microthrusts (Fig. 5n), but shear band boudins are separated by extensional faults (Fig. 5c). Likewise, the asymmetric appearance of Z-shaped dragged intergrowths (Fig. 5o2) must not be confused with the inclusion trail patterns found in porphyroblasts (Fig. 5h). In the former case, the '*pre-existing*' or '*pre-kinematic*' intergrowths: *(i)* do not merge with mylonitic foliations outside, and *(ii)* attain the Z-shaped geometry during rotation of the porphyroclasts. However, the sigmoidal inclusion trails in the porphyroblasts continue into the matrix, and indicate a shear sense opposite to that of the dragged intergrowths (compare Fig. 5h,o2).

Highly strained winged inclusions (Grasemann et al., 2019), although, appear as σ_b-type porphyroclasts of Passchier and Simpson (1986), are produced by shearing opposite to that required for the latter (Fig. 5). Partial exposure of features (Fig. 7a,b,c) may result in incorrect identification of structures, and hence should be avoided. Parallelogram shaped mica grains should be carefully observed before deducing the shear sense. The parallelogram shape of any mica grain 'm' could also be a product of overlap by two other mica grains ('m1' and 'm2' in Fig. 7d1) and hence completely unrelated to shearing (Fig. 7d2). Such cases should be avoided in determining shear sense. Moreover, a parallelogram 'p' could develop by ductile shear of rectangular unstrained grain having two possible orientations (Fig. 7e1). In such a scenario, the orientation of the nearby foliations must be considered before deriving the shear sense (Fig. 7e2); otherwise one would incorrectly deduce the shear sense.

Inside a foliation fish (Fig. 1j), individual grain(s) can be oriented in the opposite sense. This must be avoided for shear sense determination. Only the overall geometry of the foliation fish should be picked up and not the asymmetry/orientation of its constituent mineral grains

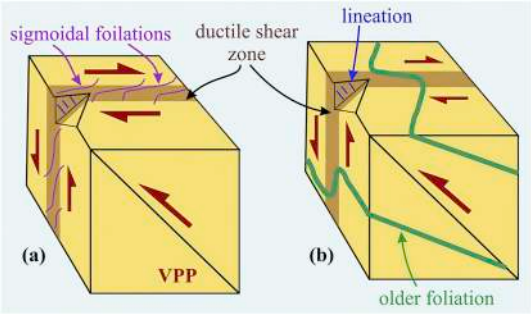

Fig. 4. Problematic shear sense indicator (first referred at Section 3). Sigmoidal foliations (a) in a ductile shear zone are reliable indicators of shear sense. However, deformation of a pre-existing foliation (green curve) (b) can be misleading and should be avoided in the interpretation of shear senses. Reproduced from fig.7 of Passchier and Coelho (2006).

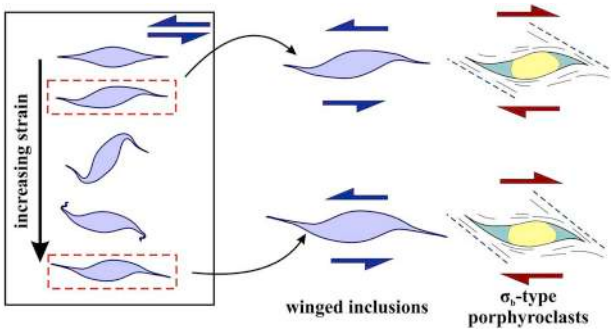

Fig. 6. Winged inclusions and σ_b-type porphyroclasts (first referred at Section 3). Products of opposite shears with near-identical geometries. Reproduced from fig. 5 of Grasemann et al. (2019) and fig. 2d of Passchier and Simpson (1986).

(Figs. 1j, 7f, Mukherjee, 2011, 2013b). The inclination of cleavage planes with respect to the C-plane should also be avoided as a sole criterion to deduce shear sense from mineral fish (Fig. 7g) (see also fig. 4 of ten Grotenhuis et al., 2003).

Crenulation cleavages, as Bell and Johnson (1992) claim, are more abundant than S–C fabrics (Fig. 1b) or any other kinematic indicators in multi-deformed terranes, and their asymmetry is a useful tool for deducing the shear sense. However, the authors also caution that

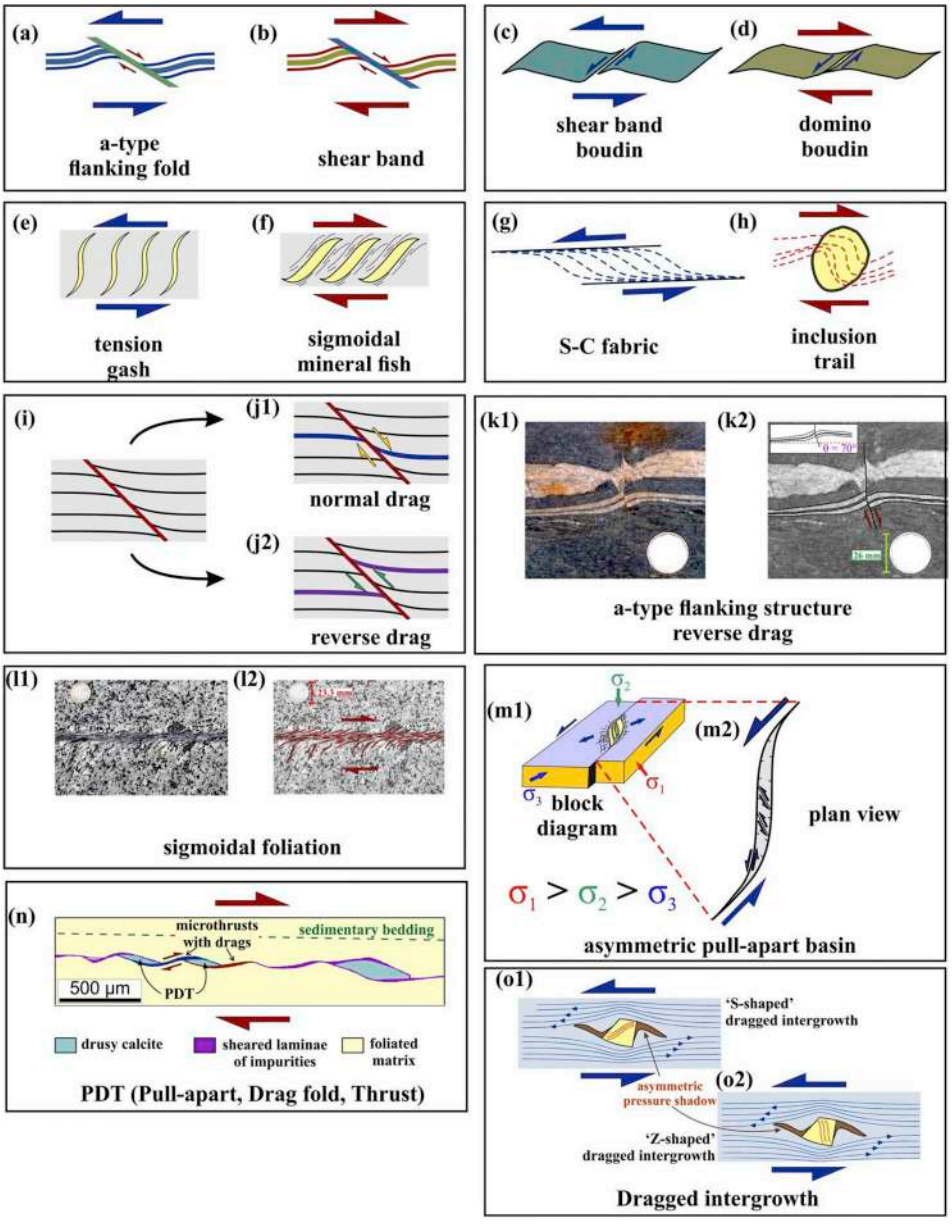

Fig. 5. Ductile shear sense indicators with similar geometries (first referred at Section 3). (a) a-type flanking fold, (b) shear band, (c) shear band boudin, (d) domino boudin, (e) tension gash, (f) sigmoid mineral fish, (g) S–C fabric, (h) inclusion trail inside a porphyroblast, (i,j1,j2) drag patterns, (k1,k2) a-type flanking structure with reverse drag (Goriganga section, Higher Himalaya Crystallines, India). Here, the marker (or the host fabric element) does not penetrate the fault (or the cross-cutting element) (see also fig. 18 of Mukherjee, 2014a). 'α' in the inset for (k2) is the acute angle between the fault and the undeformed marker. (l1,l2) Heterogeneous ductile shear zone with sigmoid foliation pattern (traced with red curves in l2) along pre-existing joints. Dextral shear sense evident. 3D block diagram (m1) and plan view (m2) of a sinistral strike-slip pull-apart basin. (n) PDT (pull-apart, drag fold, thrust), and (o1,o2) S- & Z-shaped dragged intergrowths (red curves) within δ-type mantled porphyroclasts. The blue curves (with arrow heads) show the flow directions in the matrix. (a) & (b) have identical shapes but the former is a result of sinistral shear whereas the latter is a product of dextral shear. Similarly, (c) & (d), though appear alike, are products of sinistral and dextral shears, respectively. Tension gash (e) and sigmoid mineral fish (f) look similar but indicate opposite shears. Reproduced from: (a,b) fig. 1 of Grasemann et al. (2003), (c) fig. 5c of Goscombe et al. (2004), (d) fig. 4c of Grasemann et al. (2019), (e) fig. 8a of Fossen and Cavalcante (2017), (h) fig. 5.80 of Vernon (2018), (i,j1,j2) fig. 0.7 of Mukherjee (2014a), (k1,k2) fig. 2.17 of Mukherjee (2015a), (l1,l2) fig. 4.1 of Mukherjee (2014b), (m2) fig. 19.13 of Fossen (2016), (m2) fig. 1.10 of Nemčok (2016), (n, o1,o2) figs. 9 and 11d of Scharf et al. (2019). See Fig. 1 captions for more references.

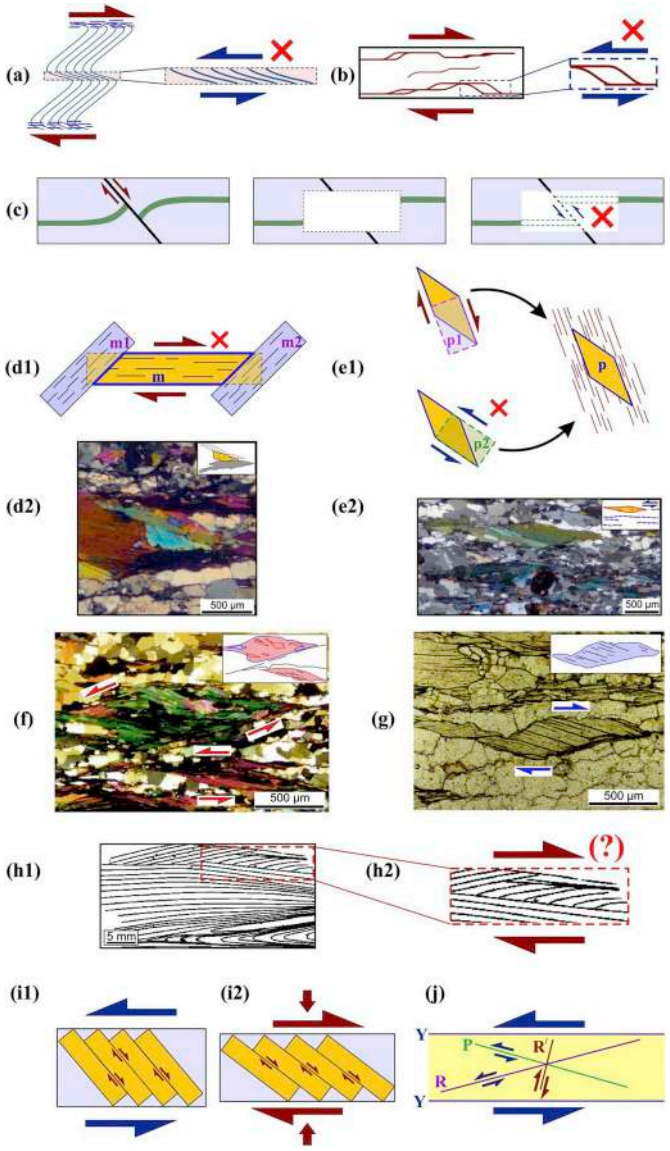

Fig. 7. Possible misinterpretations in identifying shear senses (first referred at Section 3). (a) Partial exposure (shaded region) of asymmetric crenulations. (b) Composite shear zones. Asymmetry of anastomosed domain (dashed rectangle) may give misleading shear sense (reproduced from fig. 16b of Fossen and Cavalcante, 2017). (c) Misinterpretation of a normal fault as a reverse fault. If only a part of the feature is exposed, extrapolation of marker beds (green) will give incorrect shear sense. (d1) Overlap of mica grain (m) with two other mica grains (m1 & m2) may give rise to an apparent parallelogram shape (reproduced from fig. 11 of Mukherjee, 2011). An example of the same is shown in (d2). (e1) Parallelogram 'p' could either be a product of dextral shearing of 'p1' or sinistral shearing of 'p2'. In such cases, orientation of the foliation (brown lines) should be considered. The shear plane must be parallel to the foliation (reproduced from fig. 9 of Mukherjee, 2011). (e2) Parallelogram muscovite fish exhibiting top-to-left shear. Note that the shear plane and the foliation (blue dashed lines) are parallel. (f) Composite lenticular mica fish at the centre and lower right corner showing top-to-left shear (red half arrows). Whereas, few mica inclusions inside the bigger mica fish do not show any shear sense (Karakoram Shear Zone, Jammu & Kashmir, India) (reproduced from fig. 1.72 of Mukherjee, 2013b). (g) Mica fish displaying top-to-right shear (blue half arrows) (reproduced from fig. 1.6 of Mukherjee, 2013b). (h1, h2) Partial exposure of an outcrop (red dashed rectangle) may provoke an observer to infer incorrect shear senses (reproduced from fig. 4b of Bell, 2010). Book-shelf glide/domino structure under (i1) simple shear and (i2) general shear regime. (j) Geometries of the brittle shear fractures under sinistral shear (reproduced from fig. 5.50 of Passchier and Trouw, 2005). Note the shear sense on R′ shear plane. Both (d2) (WGS 84 GPS coordinates: 33.24 N, 78.24 E) and (e2) (WGS 84 GPS coordinates: 33.27 N, 78.17 E) belong to the gneissic rocks of the Tso Morari Crystallines (Ladakh Himalaya, India).

overprinting of deformations may rotate the crenulation cleavages. In such a scenario, the final product, if considered alone, will denote a shear sense opposite to the latest one (Section 4.2.1). They further emphasize that interpretations should be based on the entire history of deformation rather than partial field exposures (Fig. 7h1,h2).

Caution should also be exercised while deciphering shear senses from the asymmetry of the Quartz CPO plots (Passchier, 1983). Studies such as Bell and Johnson (1992) and Kilian et al. (2011) show that the CPO plots from the same sample may indicate OSS. Larson and Cottle (2014) report that the asymmetry of the quartz c-axis plots derived from a sample of migmatitic paragneiss of the upper Tama Kosi region (Higher Himalayan Crystallines, Central Nepal) show OSS. The authors speculate that the two shears may reflect two separate deformations. The shear senses derived from S–C fabrics, asymmetric folds, and other such indicators may not always match with those indicated by the CPO plots (Krohe, 1990; Law et al., 1994; Xypolias and Koukouvelas, 2001; Barnhoorn et al., 2004). However, the c-axis plots obtained from the high-strain zones within a thin-section are reasonably consistent with the overall shear (Kilian et al., 2011). Summarily, shear senses are always to be cross-checked with the shear senses exhibited by other meso- or micro-scale kinematic indicators (Passchier and Trouw, 2005).

This work categorizes OSS based on *(a)* deformation regime and *(b)* whether the shear planes are parallel. The former can be subdivided into *(a1)* ductile, *(a2)* brittle, and *(a3)* ductile followed by brittle. For case-b, shear planes for the two OSS can either be *(b1)* parallel or *(b2)* non-parallel (range of the acute angle between the two: ~30–80°) (Fig. 8). However, one may confuse antithetic shears between the domino-style shear (Fig. 7i1,i2) and Riedel (R′) shear (Fig. 7j), which are present at angle of >80° and 25–60°, respectively, to the shear plane (Passchier and Trouw, 2005; Fossen, 2016; see also Fig. 16 of Pennacchioni and Zucchi, 2013), with those belonging to b2. Similarly, '*bi-sense*' zipper junctions described by Passchier and Platt (2017) also exhibit OSS along non-parallel shear planes. At this point we must make it clear that, although we discuss examples for both b1 (supplementary file S1) and b2 (5 examples, supplementary file S1), we have strictly restricted the majority of mechanisms described below (Section 4) to those which generate OSS with parallel shear planes (category b1). Moreover, in the case of b2, only those examples have been included (supplementary file S1) where the C-planes are non-parallel (Fig. 8). We do not consider the non-parallelism of C- and C′′-planes belonging to single or multi-stage deformation as examples of OSS, since it is often a tricky and difficult (yet crucial) task to differentiate the two in the field. The reason for introducing the category b2 is to make the reader aware that such features are neither uncommon in the field nor thin-sections. However, at the same time, only a few examples are included since our primary focus is category b1.

4. Genesis of OSS (Table 2)

The presence of OSS in mylonites/shear zones is common (Bell and Johnson, 1992; Blenkinsop, 2002). Their origin could be attributed to single or multiple deformations, e.g., De Paor and Eisenstadt (1987), Tourigny and Schwerdtner (1991), Little et al. (2013), etc.

We define '*single stage deformation*' as the one during which the bulk shear sense for the rock under consideration remains constant over time. Most of the shear sense-related studies commonly deal with narrow shear zones, wherein the sense is usually consistent and represents that of the latest deformation phase and the corresponding foliation.

'*Multi-stage deformation*', on the other hand, refers mainly to the temporal variation of the bulk-shear sense such that the new structural features overprint the earlier ones (e.g., Lenze and Stöckhert, 2007; Koyi et al., 2013; Czertowicz et al., 2016; Japas et al., 2016; Lopez-

Sanchez and Llana-Fúnez, 2018). Consequently, somewhat more complex history is preserved in broader/mega/plate-scale shear zones (especially at orogenic belts), with foliations from earlier deformation events either frozen inside porphyroblasts and/or at strain shadow zones or re-deformed during later tectonic events. These are the ones wherein chances of finding OSS, and/or misinterpreting kinematic indicators, is higher (Bell and Johnson, 1989, 1992; Bell and Hickey, 1999; Bell, 2010; Bell and Hobbs, 2010; Bell et al., 2013) (see A.3 in Appendix).

Moreover, we believe the most essential criterion in considering two deformation events as separate is the period of 'deformation inactivity/quiescence' that lies in between them. And hence, in our opinion, the transition from one phase of deformation to the next may or may not be accompanied by a change in the stress state/regime. We also emphasize that whether the origin is single or, multiple deformational could only be ascertained if the events are identified from various structural and/or petrological evidences. Hence, prior to arriving at a conclusion one must have clear idea of the tectono-thermal history of the region, determined from petrological or P-T studies, so that the observer does not end up using a shear sense criterion produced during an earlier event to infer the latest shear sense, and in the process, missing a deformation phase. Below, we briefly discuss the genesis of OSS.

4.1. Single stage deformation (Figs. 9–15)

OSS can coexist in a single outcrop either with sub-parallel (Little et al., 2013; Dutta, 2016) or non-parallel shear planes (~56–80° in Ruiz-Fuentes and Aerden, 2018). However, a cross-cut relation, similar to that found for fracture networks (Peacock and Sanderson, 2018 & references therein), between the two may not always be preserved/identified, rendering difficulty to constrain the relative temporal relation between the two shear events. Hence, unless established independently using alternative techniques viz., geochronology (Oriolo et al., 2018) or petrology, an absence of cross-cut relation is often assumed to indicate that the structures are coeval (Langille et al., 2010; Little et al., 2013) (see A.2, A.3 in Appendix). Below we explain the available models for OSS produced in a single deformation phase.

4.1.1. Fracturing of a layered body (Fig. 9)

Numerical models of Cooke and Underwood (2001) reveal that propagation of a mode-I fracture tip (within a dolomitic material) towards and across a bedding contact/interface (blue horizontal line in Fig. 9) can result in OSS on either side of the fracture. The authors show that in the model, wherein sliding as well as opening are permitted along the interface, a reversal in slip sense occurs as the fracture tip meets the contact (Fig. 9a and b). On the other hand, no such reversal occurs if opening along the interface is inhibited (Fig. 9c). Nevertheless, both models demonstrate that the sense of displacement along a plane may vary spatially, and sometimes also temporally.

4.1.2. Ductile deformation of a layered body with heterogeneous rheologies (Figs. 10 and 11)

Ishii (1992) performs 2D numerical experiments to demonstrate the effects of competency contrast, layering orientation, and thickness ratio on a deforming layered (one incompetent layer within two competent layers) rock mass (nearly incompressible and Newtonian rheology) under a general shear regime. The results show that the more viscous (competent) layers deform more coaxially than the less competent ones, as proposed by Lister and Williams (1983) and Treagus (1983). Such a '*partitioning of non-coaxiality*' can produce reverse shears within the more competent layers if they are oblique (45°) to the shear plane (Fig. 10) and if the rate of extension equals the rate of shear strain. Apart from that, similar but more detailed numerical experiments were conducted by Jiang (1994). The author demonstrated that over time, the sense of rotation within a single layer might reverse, even under a constant bulk flow. Stronger the coaxiality and lesser the competency of a layer, higher the are the chances of shear reversal for that layer. In support of this, Xypolias et al. (2010) report antithetic shearing to be particularly present within the weaker (less competent) mica-rich tectonites (interlayered with more competent quartz-rich tectonites) of the Evia thrust zone, Internal Hellenides, Greece.

Differences in the deformation mechanisms or strain rates (usually varies between 10^{-13} s^{-1} - 10^{-8} s^{-1} at micro-scale; Fagereng and Biggs, 2019) between adjacent domains of a rock mass is a direct consequence of the pre-existing (Pennacchioni and Mancktelow, 2018) or syn-kinematic variations in rheologic properties (Hippertt and Tohver, 1999). This can induce OSS at the domain boundaries, along which the shear strain is maximum due to localization during progressive deformation (Mancktelow and Pennacchioni, 2005) (Fig. 11) (Section 4.1.2). Hippertt and Tohver (1999) also report that such a deformation partitioning is more likely to occur for low-to medium-grade tectonites with prominent compositional layers. They further propose that if a multi-layered rock body, for example, banded mylonite, is subjected to 'simple' and 'general' shear, OSS possibly develops only in the latter scenario (Fig. 11).

4.1.3. Back-rotation under sub-simple shear regime (Fig. 12)

Back rotation (opposite to the bulk shear direction) of porphyroclasts is possible under sub-simple shear when the rotational component is less than that for simple shear (Fig. 12) (Simpson and De Paor, 1993; Fossen and Cavalcante, 2017). The authors point out that during such a deformation, a material line can pro- and retro-shear. However, back-rotated clasts often display forward sheared tails or shadow zones (Fig. 12c; also see fig. 8a of Xypolias, 2010). But the absence of such tails (Passchier, 1982; Schmid and Podladchikov, 2005) such as in Fig. 7i2 may give an impression of OSS. Passchier and Simpson (1986) suggest that whether back-rotation has occurred or not can be checked in shear zones only if the orientations of *(a)* the instantaneous stretching axis, and *(b)* the flow plane, before rotation of the porphyroclast, have been established confidently. Moreover, whether a porphyroclast will rotate backward or not depends on its axial ratio (R) as well. For

$$R > [(1 + (1 + 4S_r^2)^{1/2})(2S_r)^{-1}] \quad (1)$$

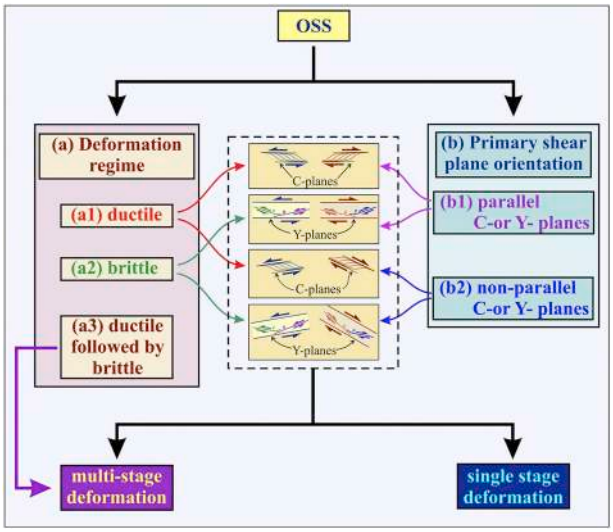

Fig. 8. Flowchart depicting the categorization of OSS based on the deformation regime and orientation of the primary shear planes (first referred at Section 3). Shear sense indicators with parallel (b1) or non-parallel (b2) primary shear planes in both ductile (a1) and brittle (a2) regime can develop due to both single (Figs. 9,11,13-15) or multiple (Figs. 16,19,21,22) phases of deformation. In contrast, category a3 will only be possible in a multi-stage deformation since it involves two different regimes.

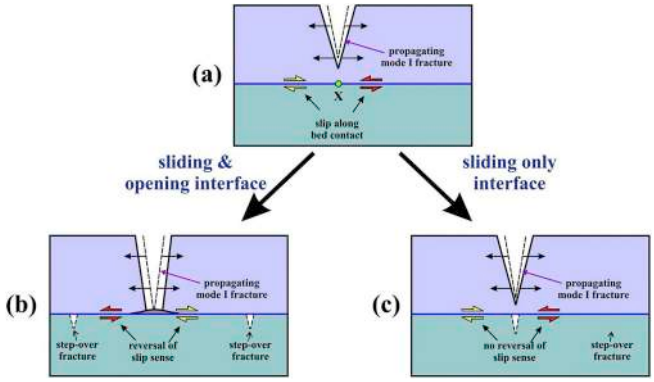

Fig. 9. Results of two numerical experiments (first referred at Section 4.1.1) showing the interaction between fracture propagation and the bedding interface of moderate strength with coefficient of friction = 0.65; cohesion (c) = 3.25 MPa. Material properties of the body resemble dolomite. (a) The fracture tip is ~3 cm away from the contact. The shear senses imposed at the bed contact are opposite on either sides of the propagating Mode-I fracture. Shear sense reversal at X (green circle) induced by the stress field near the fracture tip maximizes the magnitude of tensile stress there. (b) When both sliding and opening along the contact is allowed under a tensile stress (T) = 5 MPa, step-over fractures develop such that the shear sense reverses across the fracture (red and yellow half-arrows). (c) For an interface that allows only sliding at T = 0 MPa, fractures migrate across the contact. Unlike (b), no shear reversal occurs. Reproduced from figs. 9 and 11e of Cooke and Underwood (2001).

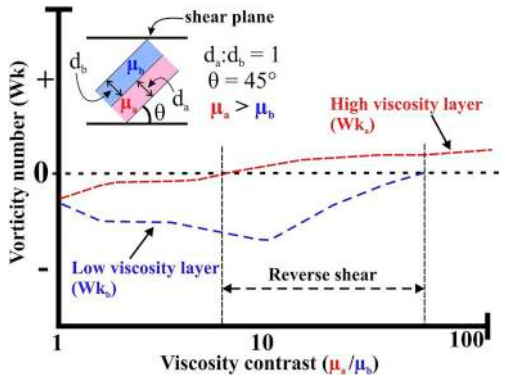

Fig. 10. Results of the 2D numerical experiments performed by Ishii (1992), and demonstrates the control of viscosity inhomogeneity on the origin of OSS (first referred at Section 4.1.2). Two layers of equal thickness ($d_a = d_b$) at angle of 45° to the shear plane promotes opposite flow vorticities, if the viscosity contrast (μa/μb) exceeds 2. Reproduced from fig. 5b of Hippertt and Tohver (1999). Also see Mulchrone and Mukherjee (2015).

where S_r is the ratio of the rate of pure shear to simple shear, the porphyroclast rotates opposite to that of the imposed simple shear (Ghosh and Ramberg, 1976). Back-rotation, however, is not limited to pophyroclasts, asymmetric boudins can also undergo the same process when the pure shear component either equals or exceeds that of the simple shear (Marques et al., 2007).

4.1.4. Block rotation under simple shear (Fig. 13)

MacLeod and Murton (1995), to explain both left- and right-lateral motion along the Southern Trodos transform fault zone (Cyprus), came up with a geometric model demonstrating simultaneous opposite shears. This model consists of several rectangular/square blocks with sizes much smaller than the shear zone width. Rotation of the blocks, synthetic to the imposed bulk shear sense, can flip slip senses at the contacts between the blocks (Fig. 13). The resulting slip planes, although oblique (~15°) to the shear zone boundary, are mutually parallel. This model, however, is somewhat similar to the bookshelf gliding/domino model that has so far been observed at *(i)* micro-scale within feldspar porphyroclasts (e.g. Vernon, 2018; Passchier and Trouw, 2005; Fossen, 2016), *(ii)* meso-scale (e.g. Branney and Kokelaar, 1994; Carmignani et al., 1994; Schulte et al., 2014; Zhao et al., 2017; Mukherjee and Khonsari, 2018) and, *(iii)* mega-scale (e.g., Freund, 1970; Cowan et al., 1986; Sigmundsson et al., 1995; Stewart and Argent, 2000; Szeliga, 2010; Zuza and Yin, 2016). Interestingly, using *'photo-geological mapping'*, Yin and Pappalardo (2015) speculate the presence of bookshelf faulting in the Enceladus, one of the moons of the planet Saturn!

4.1.5. Folding (Fig. 14)

The shear sense indicators, on the two limbs of a Class 1B buckle fold (Fig. 14a and b), exhibit OSS (Bell and Johnson, 1992; Ghosh, 1993; Twiss and Moores, 2007; Fossen, 2016). Similar reversals in shear senses, across the axial plane, are also exhibited by (active-) sheath folds (Alsop, 1994; Alsop and Carreras, 2007, Alsop and Holdsworth, 2004, 2006, 2007, 2012), which are ubiquitous across a variety of tectonic settings (Alsop et al., 2007; Searle and Alsop, 2007).

However, in almost all such scenarios, the corresponding shear planes are non-parallel except the isoclinals folds. Sengupta and Chatterjee (2015) report such an example from the quartzofeldspathic mylonites (amphibolite facies) of Phulad Shear Zone of the Delhi Fold belt (Rajasthan, western India). Several stages of deformation following the formation of a recumbent/isoclinal fold may obliterate the hinge zone, thereby rendering an explanation of OSS difficult (Fig. 14c1,c2). Re-folding of subhorizontal (Fig. 14d1,d2,d3) or sub-vertical (Fig. 14e1,e2,e3) shear zones also result in shear reversal (Goscombe and Trouw, 1999). Recumbent folds are prominent structures, especially in the orogenic belts that undergo multiple deformations (Bastida et al., 2014). Consequently, OSS in orogens should be carefully studied to avoid any misinterpretation regarding their genesis.

4.1.6. Zipping of ductile shear zones (Fig. 14)

Zipper junctions are defined as locations where two shear zones with opposite slip senses appear to diverge from the main branch, or merge (also see Koyi et al., 2013 where the authors have used the term 'wakes' for merged shear zones exhibiting OSS) to form a third branch (Passchier and Platt, 2017) called the branchline. The former is known as '*opening zipper junction*' (OZJ), whereas the term for the latter is '*closing zipper junction*' (CZJ) (Fig. 14f1-h2). Depending upon the amount and the slip sense along the branchline, these zipper junctions can be classified as *(i)* dextral (D)/sinistal (S) OZJ (Fig. 14f1,g1), *(ii)* dextral (D)/sinistral (S) CZJ (Fig. 14f2,g2), *(iii)* pure (P) OZJ/CZJ (Fig. 14h1,h2) (where the branchline eventually becomes inactive without any displacement). *(i)* and *(ii)* are also called the 'shear zipper junctions' (SZJ) (Fig. 14f1-g2). Froitzheim et al. (2006) use the term 'extraction faults' for the abandoned branch of *(iii)*. CZJ was also identified previously by Bell (1981) and Hudleston (1999). Moreover, Rosenberg & Kissling (2013) referred to OZJ with a horizontal branchline (in a compressional regime) as 'wedge'. It is crucial to note that the SZJs are expected to exhibit overprinting of shear senses close to the junction and beside any one of the flanks of the branchline (shown by blue colour zones in Fig. 14f1-g2). Besides, even more complex overprinting structures may develop if the junction moves laterally with respect to the branchline. However, such features are only predicted and have not been observed in the field so far. The following pair of mega-fault systems have so far been identified as zippers (Platt and Passchier, 2016): North- and East-Anatolian (Turkey) (see Section S.30 in the supplementary file S1) (CZJ), Altyn-Tagh and Karakoram (Tibet) (SCZJ), San Andreas-Garlock (USA) (DCZJ), and Periadriatic (Austria) (see Section S.24 in the supplementary file S1) (DCZJ).

4.1.7. Differential stretching of faulted wall rocks (Fig. 15)

These are active faults within a rock body that flows/deforms in

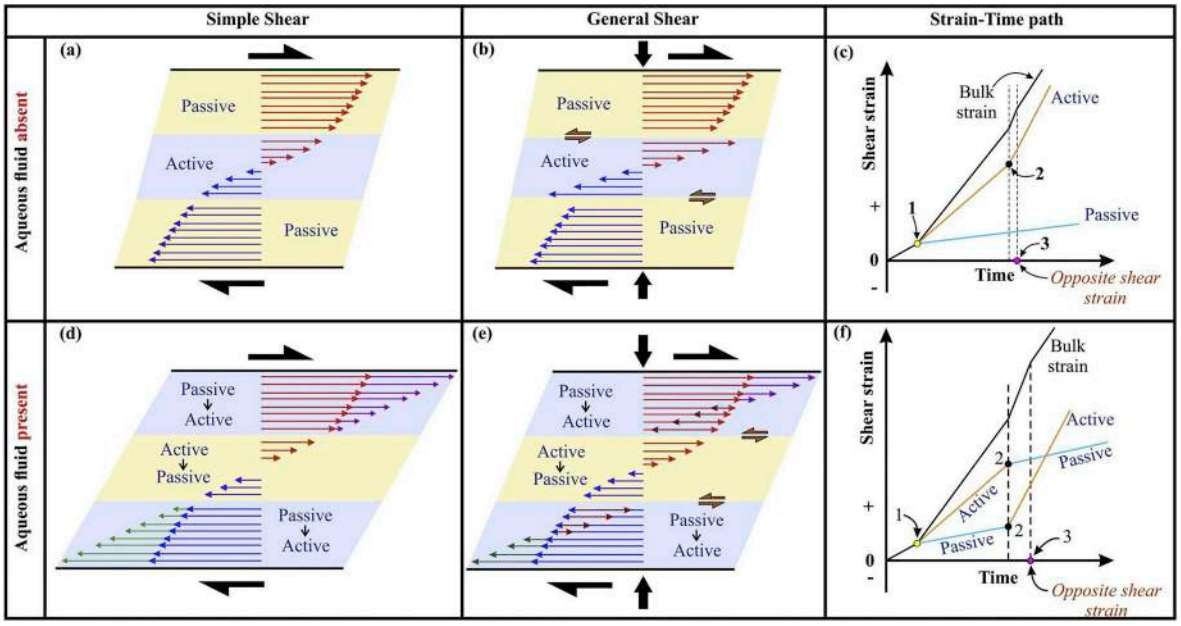

Fig. 11. Possibilities that may give rise to OSSs in a multi-layered rock (first referred at Section 4.1.2). Active layer represents the domain (e.g., quartz rich) that absorbs maximum shear strain, and hence deforms more than the passive domain (e.g., feldspar rich). Under anhydrous conditions (top row), unlike the simple shear scenario (a), shear senses at the domain boundaries are opposite (brown half arrows) to that of the overall shear (black colored half-arrows) in (b). The strain-time path for the same is shown in (c), where the individual domains start deforming differently from point 1 (yellow circle). At point 2, the strain rate for the active domain keeps increasing. Point 3 represents the situation where the strain-rate contrast between two domains is so high that opposite shears begin to develop at the domain boundaries. The scenario is quite different for water-rich conditions. Here, the initially passive domain becomes the active one (e.g., muscovitisation of feldspars, Wibberley & McCaig, 2000) and vice-versa (because quartz is stronger than muscovite) with progressive deformation. Consequently, opposite shears develop at the domain boundaries (arrows in (e)). However, unlike the previous case, OSS originates at a much lower strain-rate contrast. Redrawn after figs. 6-8 of Hippertt and Tohver (1999). Examples: figs. 1 and 4 of Hippertt and Tohver (1999).

response to far-field stress regime. It can be either a positive or a negative stretching fault depending on whether the rocks on either side lengthen or shorten, respectively (Means, 1989). Means (1990) further divide them into Type I (Fig. 15a,b,c) and Type II (Fig. 15d,e,f) categories. For the former, the stretching rate is identical on either side of the fault, whereas for the latter it differs. The author suggests that such variation or gradient in the stretching reverses shear senses along the fault. That is, slip reversal is only exhibited by the Type II stretching (Fig. 15d). The amount of offset may also vary between different marker sets (Fig. 15d). These commonly occur at deep crustal levels under ductile conditions. Pennacchioni (2005) too reported displacement gradients along ductile shear zones (S Alps, Italy), although without any prominent reversal in shear sense.

4.2. Multi-stage deformation (Figs. 16–23)

Overprinting of deformation events often results in cross-cut relation between two sets of shear fabrics (Passchier and Trouw, 2005; Fossen, 2016). Subsequent deformation events obliterate the older structures (see A.3 in Appendix), and hence evidences of younger deformation get preserved selectively (Lenze and Stöckhert, 2007). Our focus lies in shear indicators with (sub-) parallel shear planes. Here, we list various existing kinematic models that induce reverse shear sense, and hence, may give rise to OSS with/without prominent cross-cut. Although the underlying mechanism, for the different deformation/tectonic processes described under sec. 4.2.2–4.2.5, are the same as that of Sec. 4.2.1 i.e., reactivation of pre-existing fault(s) with an opposite sense, they have been presented as separate entities so that the reader can easily correlate them to the possible tectonic settings.

4.2.1. Fault reactivation/inversion tectonics (Figs. 16–18)

Reactivation of older faults/fault zones, with same (kinematic reactivation) or different (geometric reactivation) sense of displacement (Holdsworth et al., 1997) is a widespread tectonic phenomenon since faults mark low cohesion (Sibson, 1985 and references therein; White et al., 1986 and references therein; De Paor and Eisenstadt, 1987; Sibson, 2001). However, older faults may increase cohesion temporally and hence inhibit reactivation (Nortje et al., 2011). Holdsworth et al. (1997) propose two separate definitions of reactivation depending on its recent activity. For non-neotectonic reactivations, the authors suggest a temporal gap of >1 Ma between the two deformation phases (e.g., Lewisian Shear Zone (Scotland), Lei and Park, 1993; Malpica-Lamego Ductile Shear Zone (Spain), Lenze and Stöckhert, 2007; see Sections S.17 & S.19). On the other hand, neotectonic reactivations involve structures, which originate before the inception of the tectonic regime that induce reactivation (e.g., NE Brazil, Bezerra et al., 2014; Central Andes (Argentina), Sagripanti et al., 2015). The authors also categorize various criteria to identify reactivation viz., structural, geochronologic, stratigraphic, and neotectonic. The structural criterion, in particular, includes slip reversal along shear planes/zones. However, multiple (i.e., >2) slip directions do not reliably indicate reactivation (Holdsworth et al., 1997) because they may also arise due to *(i)* plate-scale partitioning of strain during oblique convergence (Tikoff and Teyssier, 1994), and *(ii)* localized variations in a regionally constant stress regime (Cashman and Ellis, 1994).

White et al. (1986) reviews that fault reactivation primarily depends on the two major factors: *(a)* orientation of the fault plane/zone with respect to the imposed stress vectors. Planes oriented favorably reactivate selectively. *(b)* Weakness of the mylonitic rocks within the fault

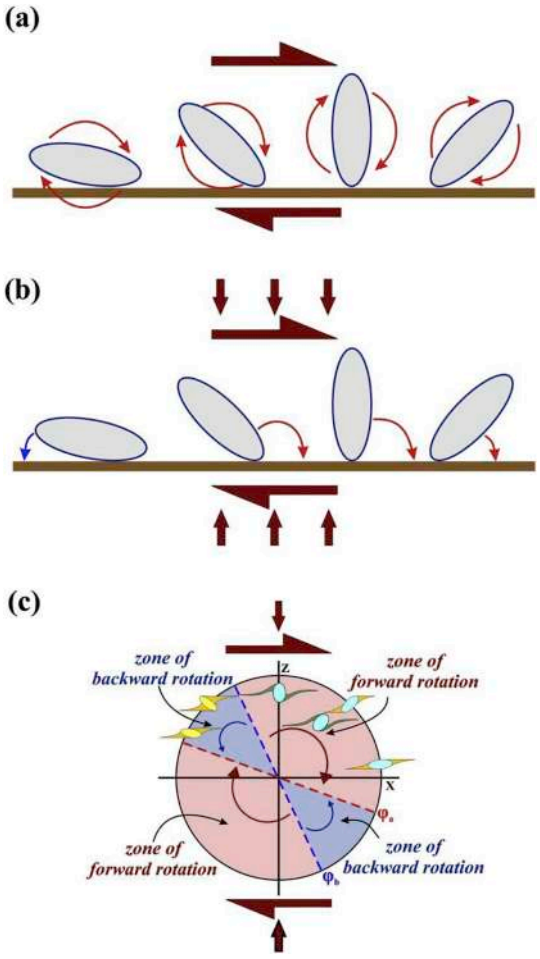

Fig. 12. Porphyroclasts rotate under (a) simple and (b) general shear. Back-rotation is possible in the second case (first referred at Section 4.1.3). Reproduced from fig. 26c and d of Fossen and Cavalcante (2017). (c) Ranges of positive (forward) and negative (backward) senses of rotation for a porphyroclast with aspect ratio (= long axis/short axis) > 1.62. The porphyroclast, with an initial orientation φ_0 (angle between the long-axis of the porphyroclast and the z-axis) lies in the red zone. It will rotate forward and assume a stable position for $\varphi_0 = \varphi_a$. Otherwise, if $\varphi_a < \varphi_0 < \varphi_b$ (i.e., in the blue zone), the porphyroclast rotates backward. The types of mantled porphyroclasts to be expected in each of the zones are also shown. Compiled and reproduced from fig. 17 of Ghosh and Ramberg (1976) and fig. 27 of Fossen and Cavalcante (2017).

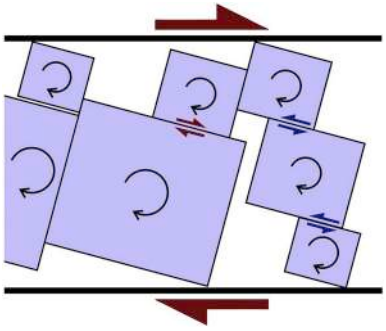

Fig. 13. Schematic model of fig. 4 of MacLeod and Murton (1995) to explain OSS in the Southern Troodos transform fault zone (Cyprus) (first referred at Section 4.1.4). Block rotations within a dextral shear zone can result in both dextral (brown half-arrows) and sinistral (blue half-arrows) shear at the contacts between the different blocks.

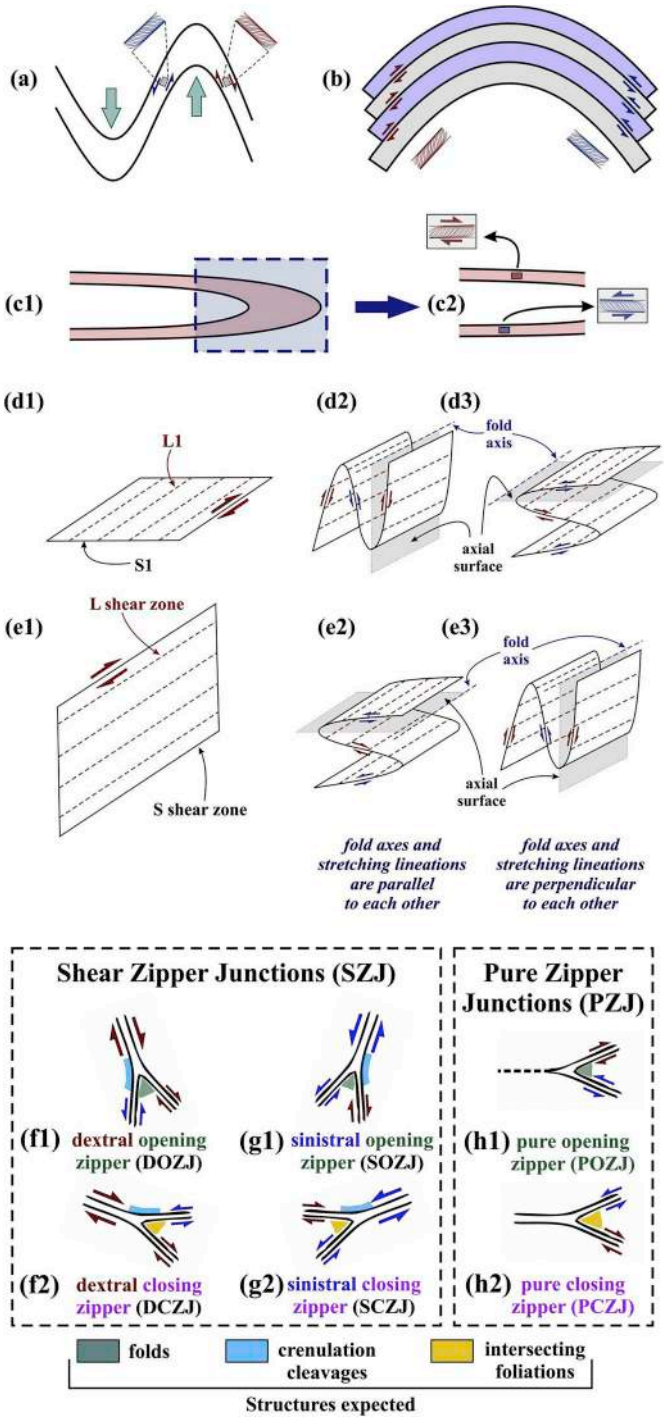

Fig. 14. Folds and zipper junctions (first referred at Sections 4.1.5 and 4.1.6). Conflicting shear senses on the limbs of (a) buckle fold, and (b) flexure-slip fold (first referred at Section 4.1.5). (c1,c2) When the hinge zone of an isoclinal recumbent fold obliterates by intense deformation, OSSs appears one above the other. This can confuse if the earlier generation fold cannot be ascertained from other field evidences (Sengupta and Chatterjee, 2015). Refolding of shear zones (d1-d3) sub-horizontal, (e1-e3) sub-vertical. Shear (f1-g2) and Pure (h1-h2) zipper junctions (Platt and Passchier, 2016; Passchier and Platt, 2017). The blue colored zones are the ones where overlap/overprinting between the two opposite shear senses (shown by the half-arrows) occur. The possible structures that one may expect at or near the zipper junctions are also mentioned. Reproduced from (a) fig. 13 of Bell and Johnson (1992); (d1-e3) figs. 2 and 3 of Goscombe and Trouw (1999). (f1-h2) figs. 4 and 7 of Passchier and Platt (2017). Examples: (a) fig. 12.22 of Fossen (2016), (f1-g2) fig. 8 of Passchier and Platt (2017).

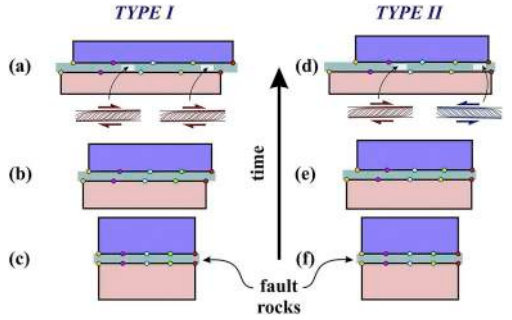

Fig. 15. Stretching faults (first referred at Section 4.1.7). (a,b,c) *Type I*. Stretching rates of both the upper and the lower blocks are similar. Offset (distance) between pink and green circles in the upper block is equal to that in the lower block. No shear reversal along the fault/shear zone (green zone). (d,e,f) *Type II*. Stretching rate of lower block greater than that of the upper block. Variation in the offset between circles is discernible. Distance between pink and green circles in the upper block is less than that in the lower block. Shear reversal (dextral between pink and blue circles, and sinistral between green and red circles) along the fault/shear zone. Redrawn from figs. 4 and 5 of Means (1990).

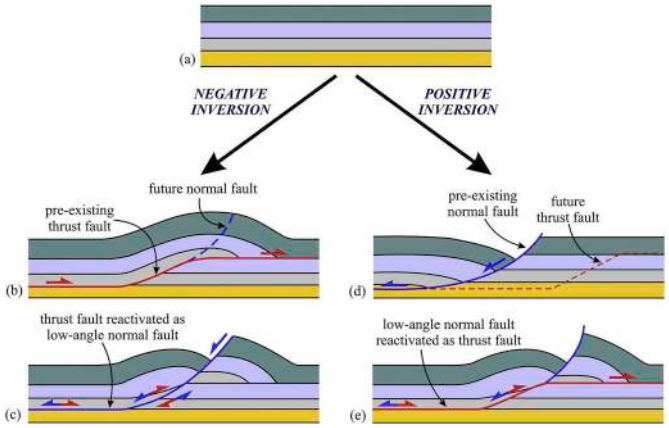

Fig. 16. Inversion tectonics in a sedimentary basin (first referred at Section 4.2.1). (a) Sequence of beds after deposition. (b) Folding of the beds over the ramp. (c) Normal faulting under extension. (d, e) Positive Inversion, where extension precedes compression. Two headed half-arrows indicate zones where evidences of both contraction and extension can be found. Reproduced from fig. 1 of Tavarnelli (1999).

zone. The weakest planes reactivate preferably. Analog and 2D numerical models of Marques and Nogueira (2008) and Ruh and Vergés (2018), respectively, show that frictional weakening (the former introduced lubricant along the fault, whereas the latter reduced the value of internal friction angle) of faults can ultimately reactivate them. Faults, not favorably oriented with respect to the stress axes, may also reactivate due to fluid-induced low cohesion of the fault zone rocks (Nortje et al., 2011 and references therein; Misra and Mukherjee, 2015).

Sedimentary basin inversion is one of the most common manifestations of fault reactivation due to orthogonal switch in the regional stress field (Turner and Williams, 2004 and references therein). Both pre- and post-orogenic extensions, termed as positive and negative inversions (Figs. 17 and 18), respectively, are possible (Bond and McClay, 1995; Constenius, 1996; Butler et al., 2006 and references therein). Tectonic inversion results in obliteration/alteration of some previous structures (Hayward and Graham, 1989). Consequently, deciphering the sequence of events becomes difficult (Cooper et al., 1989). However, Cooper et al. (2010) point out a few key features to identify tectonic inversion viz., *(i)* presence of a syn-rift sedimentary sequence, *(ii)* an asymmetric monocline facing the footwall rocks, and *(iii)* varied elevations of the marker bed in the hanging wall with respect to their regional elevation.

Besides, Redmond (1972) introduces the concept of 'null-point'. It is the point of no apparent movement along the fault, post-inversion, irrespective of the net-slip. The null point appears to drift down-section along the fault trace due to inversion (Fig. 17) (De Paor and Eisenstadt, 1987; Williams et al., 1989; Cooper and Warren, 2010).

Tavarnelli (1999) utilize overprinting of kinematic indicators to establish repeated inversions in the Umbria-Marche Range, Italy. The author further discusses that the two processes: shear sense reversal along a fault plane and collision followed by extension, can fold older shear bands and weaken shear zones. Increasing intensity of the later deformation may unfold shear bands - as they eventually enter the extensional field of the instantaneous strain ellipse (fig. 3c of Lloyd, 2018)- thereby destroying early deformation fabrics (Fig. 9 of Wennberg, 1996). '*Shear box experiment*' of Wennberg (1996) show that the angle between the S- and the C- planes (β) as well as the perpendicular distance between the two adjacent S-planes (d), both produced from the earlier deformation, decrease as shear strain elevates after reversal of shear sense (Fig. 18). A simple analysis using 2D drawing program by Bigi (2006) reveal that whether an earlier fabric will rotate or not depends upon the angle between the S- and the C-planes (SΛC) produced during the first deformation phase. The author shows that for SΛC ~30°, opposite shear may impart an extension perpendicular to the S-planes along with rotation. But, for an initial SΛC ~10°, the S-plane shortens, i.e., it behaves like an active marker, without any rotation.

4.2.2. *Subduction and exhumation (Figs. 19 and 20)*

Exhumation of the subducted lithosphere due to extension and/or buoyancy can switch shear sense at the upper boundary of the channel through which extrusion happens (Fig. 19). During subduction, the rocks at the upper margin of the lithosphere shears in a top-to-foreland (up) thrust sense. Exhumation, on the other hand, causes hinterland-directed normal motion. Similar OSS have been reported from the UHP terrane of the Norwegian Caledonides (Brueckner and Cuthbert, 2013 and references therein).

The channel flow model (Godin et al., 2006 and references therein), proposed for exhumation of *(a)* HP mid-crustal rocks of the Higher Himalayan Crystallines (e.g. Beaumont et al., 2001, 2004, 2006; Grujic et al., 2002; Jessup et al., 2006; Searle et al., 2010; Langille et al., 2010 and references therein; Mukherjee and Koyi, 2010a,b), and *(b)* UHP rocks of the Tso Morari Crystallines (Beaumont et al., 2009; Mukherjee and Mulchrone, 2012), also explain shear reversal along the upper

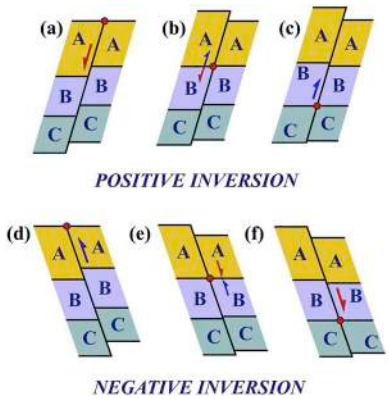

Fig. 17. Migration of the null point (red circle) along the fault trace during both (a,b,c) positive (normal movement → reverse movement) and (d,e,f) negative (reverse movement → normal movement) inversion (first referred at Section 4.2.1). Half-arrows indicate the sense of movement. Presence of two oppositely directed half-arrows (b,e) indicate shear reversal. Reproduced from fig. 1 of De Paor and Eisenstadt (1987).

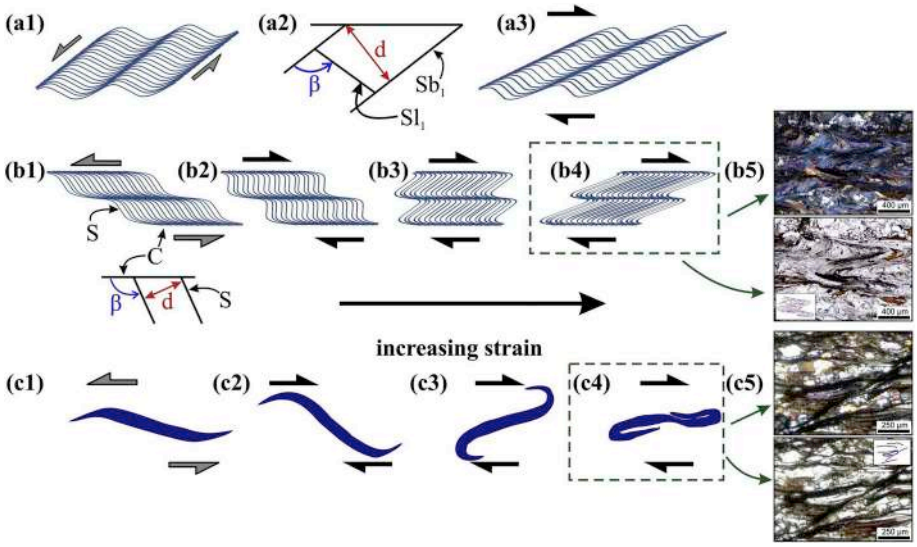

Fig. 18. Overprinting of deformations and variations in the morphologies (first referred at Section 4.2.1). (a1-a3, b1-b4) shear bands, (b5) Thin-section images (both plane- and cross-polarized) of a schistose sample (amphibolite facies, Early Cambrian in age; Epard & Steck, 2008 & references therein) from the Zildat Shear Zone (WGS 84 GPS coordinates: 33.24 N, 78.36 E; northern margin of the Tso Morari Crystallines, Ladakh Himalaya, India) showing crenulations. The photomicrographs in plane polars also contain sketches as inset, and (c1-c4) isolated sigmoid quartz vein. (c5) Thin-section photographs (both plane- and cross-polarized) of hook-shaped aggregate of quartz grains. Initial sinistral shearing was followed by dextral shear produced the hook shape (Location: Zanskar Shear Zone). The parameters "β" (angle between the C- and S-planes, measured counter-clockwise from the C-plane) and "d" (perpendicular distance between adjacent S-planes) tend to decrease as strain elevates when an initial S–C fabric (produced from sinistral shear) is overprinted by dextral shear. Redrawn after figs. 8a and b of Wennberg (1996).

portion of the exhuming viscous channel (Fig. 20). Slab rollback is another mechanism that accommodates ductile extrusion of the subducted rocks (Tapponier et al., 1982; Armijo et al., 1999; Brun and Faccenna, 2008; Hacker and Gerya, 2013; Sternai et al., 2014) by inducing extension on the over-riding plate (Sternai et al., 2014; Schlunegger and Kissling, 2015; Chen et al., 2016; Cassel et al., 2018), which can also trigger gravitational collapse (Section 4.2.4) (Rey and Müller, 2010). Hence, OSS should also be expected from terranes extruded as a result of slab rollback.

4.2.3. Tilting & overturning (Fig. 21)

This model explains the coexistence of OSS without any change in regional stress regime. As per this model (Fig. 21), tilting of rocks or fault planes in a sedimentary basin *(i)* against or *(ii)* towards the transport direction, followed by overturning can reverse shear sense. Interestingly, case *(i)* (Fig. 21b and c) would result in a single deformation event leading to OSS. Case *(ii)* would produce two deformation events leading to OSS (Fig. 21d and e). Lim and Cho (2012) propose a model, both cases *(i)* and *(ii)*, to explain the OSS in the Ocheon area, Chungam Basin, South Korea (Detail in Section 4).

4.2.4. Gravitational collapse (Fig. 22)

Bell and Newman (2006) explain how episodic gravitational collapse, horizontal spreading and vertical shortening during convergence

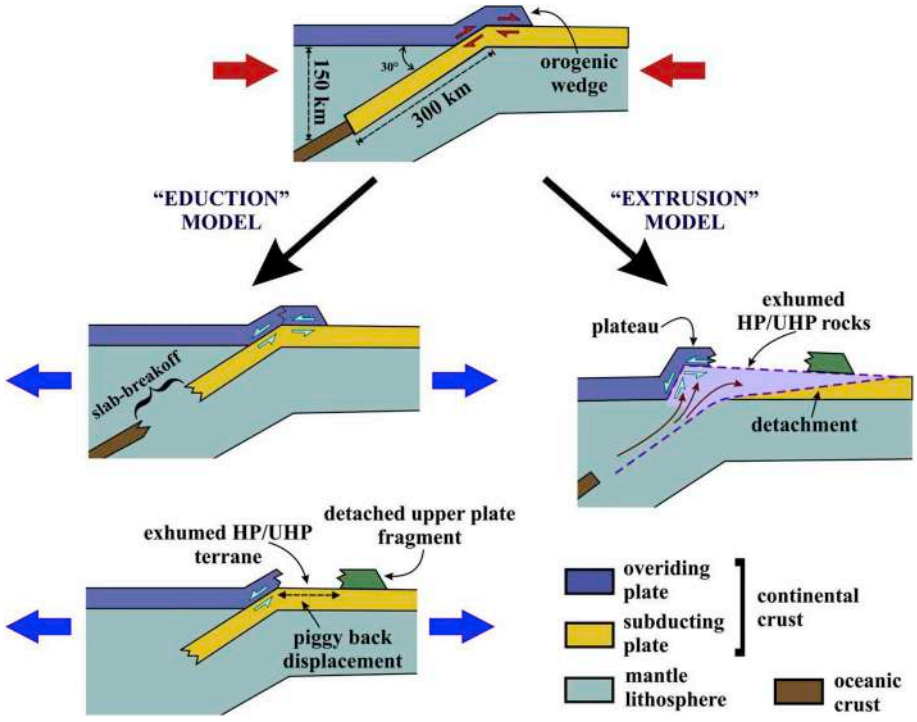

Fig. 19. OSS in an exhumed terrane (first referred at Section 4.2.2). Top-to-foreland shear (red half arrows) on the upper part of the subducting continental crust is replaced by a top-to-hinterland shear during extension (*eduction model*) or buoyancy (*extrusion model*) driven exhumation. Redrawn after fig. 1 of Brueckner & Cuthbert (2013).

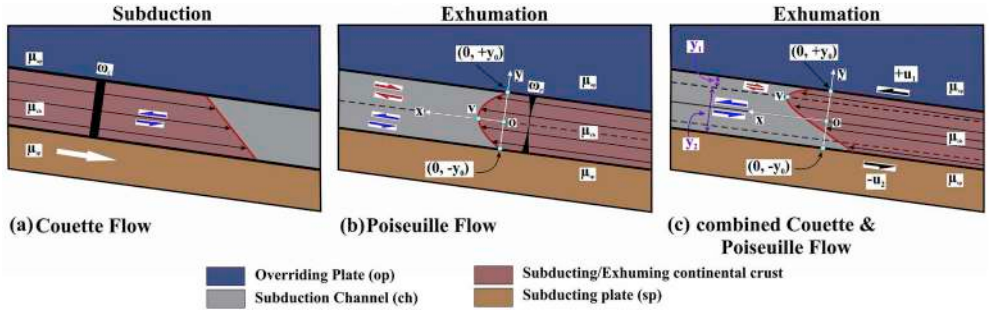

Fig. 20. Channel flow model (redrawn after fig. 2 of Godin et al., 2006) (first referred at Section 4.2.2). (a) Couette Flow during burial, (b) Poiseuille flow for exhumation, and (c) combined Couette & Poiseuille flow (redrawn after fig.1e of Mukherjee, 2012b). ω_c, ω_p:vorticity for ideal Couette & Poiseuille flows, respectively. Thickness of zones: $y_1 = y_0 - 0.5\ y_0^{-1}\ \mu(U_1+U_2)\ (\partial P/\partial x\text{-}dgSin\theta)^{-1}$, $y_2 = y_0 + 0.5\ y_0^{-1}\ \mu(U_1+U_2)\ (\partial P/\partial x\text{-}dgSin\theta)^{-1}$ (Schlichting and Gersten, 2017). Thickness 'y_2' is more than 'y_1' in (c), whereas the two zones of opposite shear have equal thickness i.e. y_0 unit (half the width of the channel). The width of the black bars denotes the variation of vorticity values across the subduction channel. μ_{op}, μ_{ch} and μ_{sp}: viscosities of the overriding plate, subduction channel and the subducting plate, respectively ($\mu_{op} > \mu_{ch} < \mu_{sp}$). Velocity profiles: (b) $U_x = 0.5\ \mu^{-1}\ [\partial P/\partial x\text{-}dgSin\theta]\ (y^2\text{-}y_o^2)$, (c) $U_x = 0.5\ \mu^{-1}\ [\partial P/\partial x\text{-}dgSin\theta]\ (y^2\text{-}y_o^2) + 0.5\{y\ y_0^{-1}(U_1+U_2) + (U_1\text{–}U_2)\}$ (Schlichting and Gersten, 2017). Thin arrows: velocity vectors, red line and curve: velocity profile; half-arrows: shear sense. Vide Mulchrone and Mukherjee (2015, 2016, 2019) for more detailed discussions.

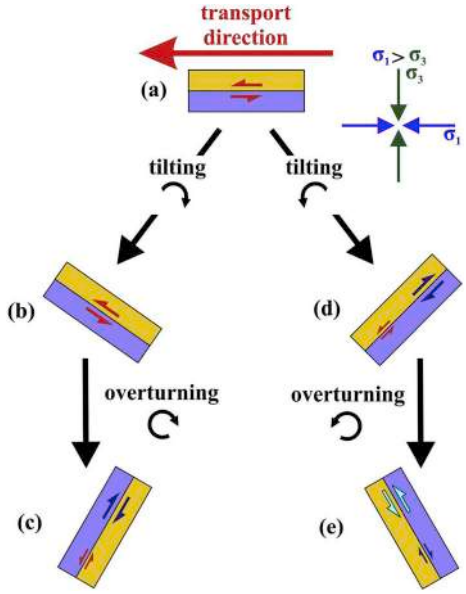

Fig. 21. Development of OSS during tilting and overturning of lithounits (first referred at Section 4.2.3). Under a constant state of stress (denoted at top right corner), and transport direction (towards left), shear senses can get overprinted during tilting and turning of the rock units. Redrawn after fig. 11 of Lim and Cho (2012).

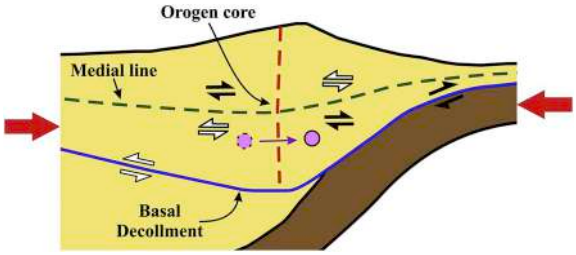

Fig. 22. Crustal thickening and gravitational collapse in an orogen (first referred at Section 4.2.4). Continued thickening of the continental crust followed by an episodic collapse due to sub-horizontal extension during an ongoing compression can flip shear senses at different parts of an orogen. The sample (pink circles, dashed boundary denotes the starting position) initially present to the left of the orogen core (red dashed line) may migrate towards foreland due to continued convergence, and hence will record different shear senses (white and black half-arrows). Horizontal stretching is highest along the medial line (green dashed line) during gravitational collapse. Compiled from fig. 18b of Bell &Newman (2006) and figs. 8c and d of Bell and Sapkota (2012).

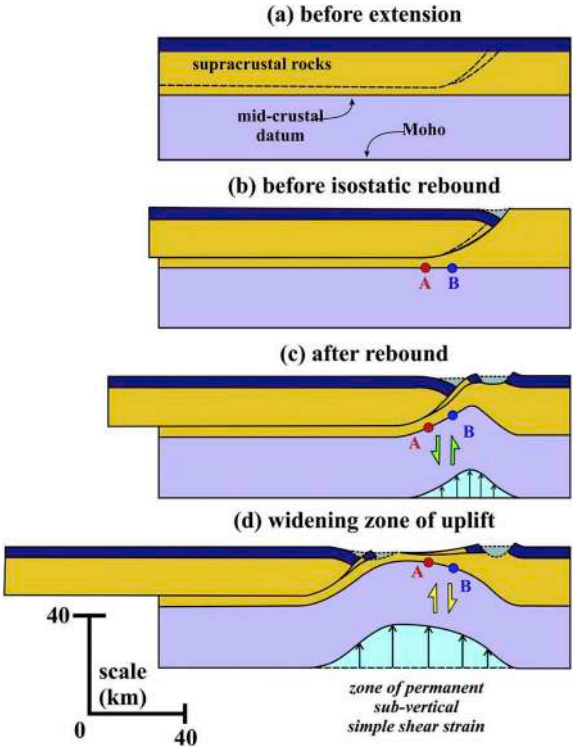

Fig. 23. Shear sense reversal along a vertical plane due to isostatic rebound (first referred at Section 4.2.5). Continued extension and widening of basin (a,b) creates negative load, which compensates by the topographic uplift of the footwall rocks. Migration of the uplifted zone in the direction of extension reverses the shear sense (c,d). Reproduced from fig. 4 of Wernicke and Axen (1988).

in orogens cause OSS across the orogen core and the medial line – the horizontal line perpendicular to orogenic trend along which lateral spreading is maximum during a gravitational collapse - of the orogen (Fig. 22). A marker initially in the hinterland of the core, will undergo OSS once it moves beyond the core and towards the foreland. Horizontal shortening-induced crustal thickening may gravitationally collapse the over-thickened crust (Liu et al., 2000; Rey et al., 2001 and references therein). Bell and Newman (2006) and Bell and Sapkota (2012) suggest such a model to justify the complexity of the inclusion trail geometry within the porphyroblasts from multiply deformed rocks of the New England Appalachians (eastern USA) and the Kathmandu Nappe (central Nepal), respectively. Whether the Kathmandu Nappe rocks belong to the Lesser Himalayan Sequence (LHS) (e.g. Upreti and Le Fort, 1999; Hodges, 2000; Yin, 2006) or the Higher Himalayan

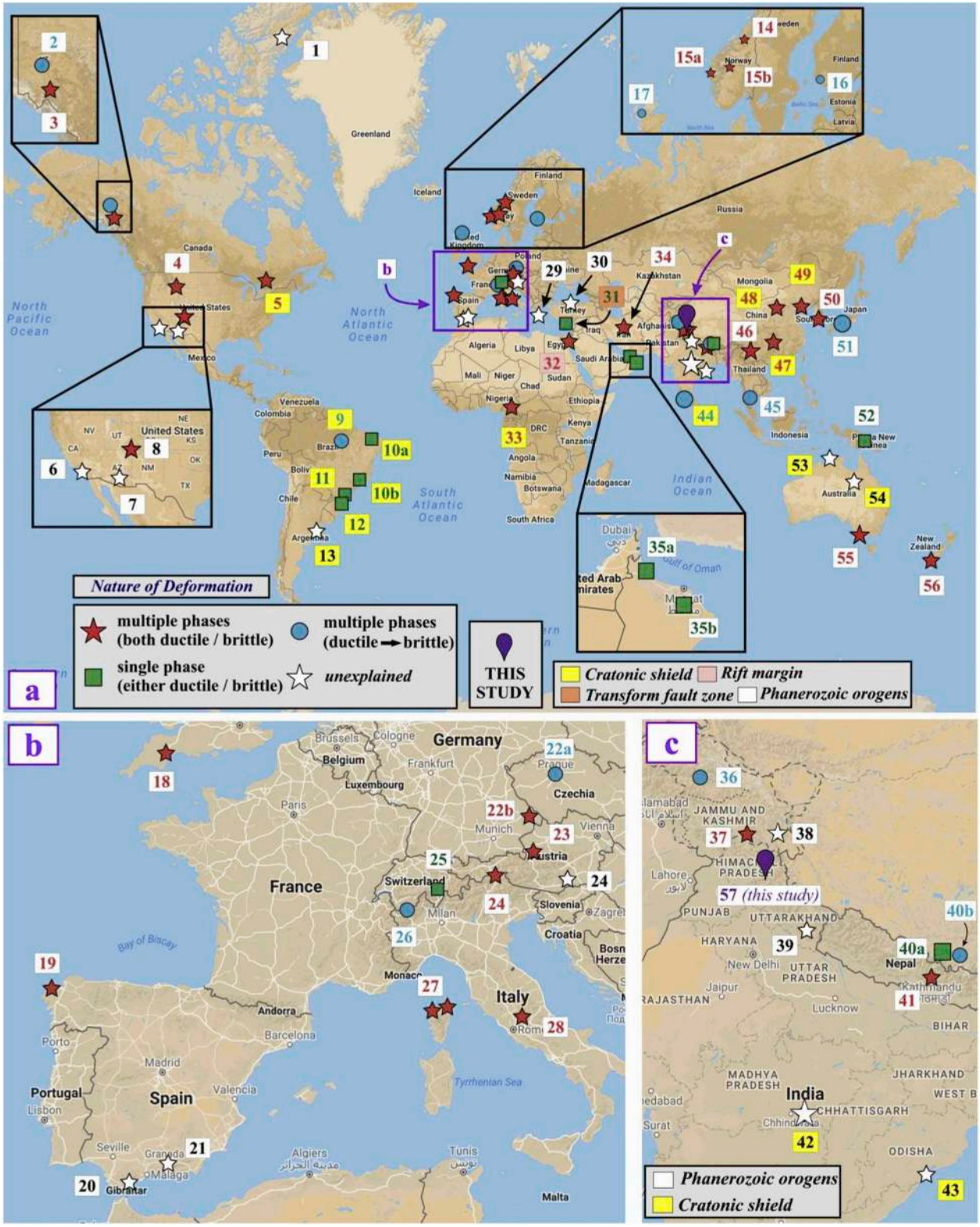

Fig. 24. Global distribution of OSS reported in the literature, and compiled in this study (first referred at Section 6). The numbers corresponding to each location denote the "Sl no." in Table 3. Yellow, pink, orange, and white colored boxes indicate that the locations belong to Precambrian shields, rift margin, transform fault zone and Phanerozoic orogens, respectively. The map is taken from Google My Maps (*www.google.com/mymaps*; accessed on December 2018).

Crystallines (HHC) (e.g. Grasemann et al., 2003; Robinson et al., 2003) or the Tethyan Himalayan Sequence (THS) (e.g. Webb et al., 2011; Khanal et al., 2015; Rapa et al., 2016) is still debated.

4.2.5. Isostatic adjustments (Fig. 23)

Shear sense reversal can also occur during isostatic rebound (Kearey et al., 2009) of the footwall and lateral migration of the uplifted portion (Fig. 23). The negative load of the depression/basin created by the extension of the lithosphere uplifts the footwall rocks isostatically.

Table 3
List of locations where OSS have been reported along with the references (Fig. 24). Note: a. Two locations from same terrane have been clubbed under one serial number. The numbers in the map correspond to the '*Sl no.*' b. *Green fonts*: OSS due to reorientation of principal stress axes. c. The list has been arranged continent-wise. For the detailed descriptions, refer to "Section S.x" in the supplementary file S1where 'x' denotes the corresponding '*Sl no.*' in this table.

Sl. no	Location	Shear Sense	Nature of kinematic indicators	References	Plausible origin of OSS proposed by corresponding workers
1	Franklinian Basin, Ellesmere Island, Canada	Near-vertical fault	Brittle	De Paor and Eisenstadt (1987)	–
2	Yukon River Shear Zone, Canada	Top-to-ESE (down) → Top-to-WNW (up)	Ductile → Brittle	Parsons et al. (2018) & references therein	reactivation of ductile normal fault (~259 - 176 Ma) to reverse fault (<176 Ma)
3	Teslin Suture Zone, Canada	Top-to-E (up) → Right lateral translation → Top-to-W (down)	Ductile	Hansen (1992)	subduction related reverse movement followed by normal slip during exhumation
4	Ruby Mountains, USA	Top-to-south (up) → Top-to-north (down)	Ductile	Sousa (2008)	topographic collapse of the thickened orogenic crust
5	Belleterre Greenstone Belt, Canada	Dextral → Sinistral	Ductile	Tourigny and Schwerdtner (1991)	orthogonal switching of the principal compressive stress axes from NW-SE → NE-SW
6	Portuguese bend landslide complex, California, USA	Sinistral → Dextral	Brittle	Larue and Hudleston (1987)	–
7	Pinal Peak, USA	Top-to-S (up) & Top-to-N (down)	Ductile	Keep and Hansen (1994)	–
8	Northern Snake Range Mylonite Zone, USA	Top-to-E → Top-to-W	Ductile	Cooper et al. (2010)	shear reversal due to roll over of the mylonites over the hinge as in '*rolling hinge system*' of Axen et al. (1995)
9	Itacaiúnas Belt, Brazil	Sinistral (Ductile) → Dextral (Brittle) → Sinistral (Brittle) → Dextral (Brittle)	Ductile → Brittle	Pinheiro and Holdsworth (1997)	oscillation of the principal compressive stress axes between NE-SW and NW-SE
10a,b	Senador Pompeu shear zone and Bação complex, Brazil	Dextral & Sinistral	Ductile	Hippert and Tohver (1999)	deformation induced rheological changes within different domains led to OSS at domain boundaries
11	Quadrilátero Ferrífero, SE Brazil	Top-to-N & Top-to-S; Top-to-E & Top-to-W	Ductile	Hippertt and Davis (2000)	folding (flexure-slip) resulted in bedding parallel shear zones with slip sense opposite to that of at the margins due to exhumation of gneissic dome
12	Major Gercino Shear Zone, Brazil	Dextral & Sinistral	Ductile	Hueck et al. (2018) & references therein	pure shear dominated deformation resulted in bidirectional shear
13	Azul megashear zone, Argentina	Dextral & Sinistral	Ductile	Frisicale et al. (2005) & references therein	–
14	Møre-Trøndelag Fault Zone, Central Norway	Top-to-NE → Top-to-SW	Ductile	Seranne (1992)	post-orogenic extension collapse during Mid-Devonian
15a,b	Bergen Arc Shear Zone, Norway	Top-to-SE → Top-to-NW	Ductile	15a: Wennberg (1996); 15b: Harris et al. (2002)	extensional deformation at late stages of orogeny or post-orogeny
16	Svecofennian shear zones, Finland	Top-to-W up → Top-to-E down	Ductile → Brittle	Väisänen and Skyttä (2007) & Torvela et al. (2008)	reorientation of extensional direction from ~ NE-SW → ~ E-W
17	Lewisian Shear Zone, Scotland	Sinistral → Dextral → Sinistral	Ductile → Brittle → Brittle	Lei and Park (1993)	*first reversal*: change in principal compression direction from ~ NW-SE → ~ N–S; *second reversal*: clockwise rotation of the region with respect to a dextral strike-slip fault system in the vicinity
18	Greenclife-Sticklepath-Lustleigh fault zone, UK	Dextral → Sinistral → Dextral (locally)	Brittle	Holloway and Chadwick (1986)	*first reversal*: change in the tectonic regime from compressive to extensional; *second reversal*: localized occurrences hence unexplained
19	Malpica-Lamego Ductile Shear Zone (Northern Segment), Spain	Dextral → Sinistral	Ductile	Pamplona et al. (2015) & references therein	reactivation of faults due to intracontinental tectonics
20	Ronda Peridotite, SW Spain	Top-to-N → Top-to-S	Ductile	Van der Wal et al. (1992), Van der Wal and Vissers (1996)	–
21	Nevado-Filabride complex, Spain	Top-to-W & Top-to-E	Ductile	Ruiz-Fuentes and Aerden (2018)	–
22a,b	Bohemian Massif, Czech Republic	Dextral (Ductile) → Sinistral (Ductile) → Dextral (Brittle)	Ductile and Brittle	22a: Mattern (2001); 22b: Galadí-Enríquez et al. (2006) (22b)	*first reversal*: orthogonal switch of principal compressive stress axes from ~ N–S → ~ E-W; *second reversal*: restoration of ~ N–S compression (?)
23	Alpine-Carpathian-Pannonian region (Eastern Alps)	Dextral → Sinistral (NW-SE trending faults) & Sinsitral → Dextral (NE-SW trending faults)	Brittle	Peresson and Decker (1997)	switching of principal compressive stress direction from ~ N–S → ~ E-W

(*continued on next page*)

Table 3 (*continued*)

Sl. no	Location	Shear Sense	Nature of kinematic indicators	References	Plausible origin of OSS proposed by corresponding workers
24	Greiner shear zone, Eastern Alps, Austria	Sinistral → Dextral	Ductile	Barnes et al. (2004)	switch to dextral shear occurred in response to the ~ N–S compresssion due to continued convergence between the Eurasian & Adriatic blocks
	Koralpe range, Eastern Alps, Austria	Top-to-S & Top-to-N	Ductile	Hatley et al. (2009)	–
25	Vals-Scaradra Shear Zone, Switzerland	Top-to-SW & Top-to-NE	Ductile	Kossak-Glowczewski et al. (2017)	lateral spreading of the northward propagating Adula Nappe along the ~ WSW-ENE striking Vals-Scaradra Shear Zone
26	Combin & Zermatt-Saas zones, Italy	Top-to-SE → Top-to-NW	Ductile → semi-Ductile and Brittle	Kirst and Leiss (2017) & references therein	post-exhumational coaxial deformation
27	Alpine Corsica, Corsica Islands, France	Top-to-W (up) → Top-to-E (down)	Ductile	Jolivet et al. (1990,1991), Beaudoin et al. (2017)	post-orogenic collapse of thickened crust
28	The Apennines, Italy	top-to-W(SW) (down) (pre-orogenic) → top-to-E (NE) (up) (syn-orogenic) → top-to-W(SW) (down) (post-orogenic)	Overall Brittle deformation but the kinematic indicators are Ductile in nature	Tavarnelli (1999), Scisciani et al. (2002) & Bigi (2006)	first reversal: ~ NE-SW orogenic compression; second reversal: post-orogenic reactivation of thrust faults due to ~ E-W extension
29	Chelmos Shear Zone, Greece	Top-to-W/SW & Top-to-E/NE	Ductile	Xypolias and Koukouvelas (2001)	–
30	North Anatolian fault zone, Turkey	Sinistral → Dextral	Brittle	Hancock and Barka (1981)	–
31	Southern Troodos transform fault zone, Cyprus	Dextral & Sinistral	Brittle	MacLeod and Murton (1995)	rigid block rotation within a shear zone resulted in OSS along block margins
32	Wadi Kid, Egypt	Top-to-NW → Top-to-SE	Ductile	Blasband et al. (1997)	upwarping of the region due to intrusion
33	Central Cameroon Shear Zone	Sinistral → Dextral	Ductile	Ngako et al. (2003)	reorientation of compressive stress from ~ NE-SW → ~ NW-SE during the Pan-African orogeny
34	Doruneh Fault System, Iran	Dextral → Sinistral	Ductile & Brittle	Javadi et al. (2015)	change in compression from ~ NW-SE → ~ N–S due to Arabia-Eurasia convergence
35a	Hilti massif, Oman	Top-to-W & Top-to-E	Ductile	Ceuleneer et al. (1988); Michibayashi et al. (2000); Dijkstra et al. (2002)	variation in the relative velocity of the lithosphere and the underlying mantle flow (asthenosphere) to the spreading rate ofthe ridge
35b	Wadi Tayin massif, Oman	Top-to-NW & Top-to-SE	Ductile	Nicolas and Boudier (2008)	divergence of the asthenospheric mantle flow
36	Nanga Parbat massif, Pakistan	Top-to-S up → Top-to-N down	Ductile → Brittle-Ductile	Argles and Edwards (2002)	syn-convergent extension
37	Zanskar Shear Zone, India	Top-to-SW up → Top-to-NE down	Ductile	Kellett et al. (2019) & references therein	normal slip induced by exhumation of the HHC towards foreland
38	Tso Morari Crystallines, Ladakh Himalaya, India	Top-to-N & Top-to-S	Ductile	Dutta (2016)	–
	Tso Morari Crystallines, Ladakh Himalaya, India	Top-to-NE (down) → Top-to-SW (up)	Brittle	Sen et al. (2013)	–
39	North Almora Thrust Zone, India	Top-to-S down → Top-to-N up	Ductile-Brittle	Agarwal et al. (2016)	–
40a	Tethys Himlaya, Tibet	Top-to-N & Top-to-S	Ductile	Langille et al. (2010)	coaxial deformation or viscosity heterogeneity
40b	Tethys Himlaya, Tibet	Top-to-S → Top-to-N	Ductile → Ductile-Brittle	King et al. (2011)	extrusion of low-viscosity channel towards south
41	Kathmandu nappe, Nepal	Top-to-N → Top-to-S	Ductile	Bell and Sapkota (2012)	gravitational collapse of over-thickened orogenic crust
42	Gavilgarh–Tan shear zone, India	Sinistral (Ductile) → Dextral (semi-Brittle) → Sinistral (Brittle)	Ductile → Brittle	Chattopadhyay et al. (2008)	–
43	Eastern Ghat Belts, India	Dextral & Sinistral	Ductile-Brittle	Dobmeier and Simmat (2002)	–
44	Achankovil Shear Zone, Southern India	Dextral → Sinistral	Ductile → Brittle	Rajesh and Chetty (2006)	1. Dextral: East African Orogeny, 2. Sinistral: Kuunga Orogeny
45	Thai Peninsula, Thailand	1. Sinitral → Dextral (TPF & MPF); 2. Dextral → Sinistral (KMF & RF)	Ductile → Brittle	Watkinson et al. (2008) & references therein	1. Indo-Eurasia collision; 2. subduction along southern Sundaland or Indo-Eurasia convergence or both
46	Red River Fault Zone, SE China	Sinistral → Dextral	Brittle	Leloup et al. (2001), Zhu et al. (2009)	eastward extrusion of the South China block realtive to the Indochina block
47	Beishan Terrane, China	Sinistral → Dextral	Ductile and Brittle	Zhang and Cunningham (2012) & references therein	switching of principal compressive stress direction from ~ NE-SW → ~ NW-SE due to westward subduction of Pacific plate beneath the Eurasian plate along eastern China
48	Ertix Fault, Central Asian Orogenic System, NW China	Dextral → Sinistral	Brittle	Allen et al. (1995)	intra-continental deformation

(*continued on next page*)

Table 3 (*continued*)

Sl. no	Location	Shear Sense	Nature of kinematic indicators	References	Plausible origin of OSS proposed by corresponding workers
49	Tan-Lu fault, SE China	Sinistral → Dextral	Brittle	Hsiao et al. (2004) & references therein	change in subduction direction of the Pacific plate beneath Eurasia or Indo-Eurasia collsion or both
50	Chungnam Basin, S Korea	Top-to-E → Top-to-W and vice versa	Ductile	Lim and Cho (2012)	tiltling and overturning of the rocks in the basin under constant ~ WNW-ESE compressive stress field
51	Yamasaki, Mitoke fault zones and Median Tectonic Line, Japan	1. Dextral → Sinistral (YFZ, MFZ); 2. Sinistral → Dextral (MTL)	Ductile & Brittle	Maruyama and Lin (2004)	opening of the Japan Sea resulted in the reorientation of the maximum horizontal stress direction from ~ N–S/NE-SW → ~ NW-SE/WNW-ESE
52	D'Entrecasteaux Islands, Papua New Guinea	Top-to-E & Top-to-W	Ductile	Little et al. (2013)	syn-exhumational pure shear dominated deformation
53	Woodroffe Thrust, Australia	Top-to-N & Top-to-S	Ductile	Bell and Johnson (1992)	–
54	Mary Kathleen fold belt, Australia	Top-to-N & Top-to-S	Ductile	Holcombe et al. (1991)	–
55	Castle Cove Fault, Australia	Top-to-NW (down) → Top-to-SE (up)	Brittle	Holford et al. (2014)	Late Miocene switching of principal compressive direction from ~ NE-SW → ~ NW-SE
56	Moonlight Fault Zone, New Zealand	Top-to-W (down) → Top-to-E (up)	Brittle	Smith et al. (2017) & references therein	orthogonal switching of the prinicpal compressive stress axes from NE-SW → NW-SE

Continued displacement of the hanging wall rocks due to extension widens the basin and consequently the uplifted portion of the footwall, in the same direction, would compensate the void created above the décollement (Wernicke and Axen, 1988). Consequently, the footwall rocks reverse shear along several (sub-) vertical planes (Fig. 23c and d).

It must be noted, that the classification suggested in Fig. 8 is applicable for both single and multi-stage deformations, except for the category a3 (ductile followed by brittle deformation) that falls under the later. As far as orientations of the primary shear planes are concerned, most of the mechanisms discussed so far will produce OSS with parallel primary shear planes (category b1 in Fig. 8) except for class 1B buckle folding (Fig. 14a and b). Besides, multi-stage deformation can certainly result in OSS with non-parallel shear senses, and a few examples have also been discussed below, e.g., location no. 8, 9, 17, 21, 40b, and 42 (Fig. 24, Table 3, supplementary file S1).

5. Numerical simulations

5.1. Introduction

We study the effects of two-stages of deformation viz., pure shear, and dextral simple shear on a rectangular domain with rheological properties of a (non-schistose) sandstone (Table A1 in the Appendix). We use simple 2D-finite element modelling (FEM) of an elasto-plastic material. Two modelling experiments (Fig. A1 in the Appendix) are performed: (i) *Model I*: pure shear followed by dextral simple shear, (ii) *Model II*: dextral simple shear followed by pure shear. Both are time-dependent models wherein the stresses on the upper boundary of the domain increase non-linearly with time (Fig. A2 in the Appendix). The simulations are carried out in the software COMSOL Multiphysics v5.4. We aim to investigate how these two-stage deformations produces OSS.

Ductile deformation of rocks can be reasonably approximated by an elasto-plastic rheology (Vermeer and De Borst, 1984; Ord, 1991; Poliakov and Herrmann, 1994; Zhang et al., 1996; Burg, 1999; Currenti et al., 2010; Turcotte and Schubert, 2014) with linear isotropic hardening (Paterson and Wong, 2005; Anandarajah, 2011; Hobbs and Ord, 2015). Herein the material undergoes permanent/irreversible (non-newtonian) deformation (hardening) once the applied stress crosses its elastic limit or the plastic yield point (σ_{ys}). (Jaeger et al., 2009; see Fig. 7.27 of Turcotte and Schubert, 2014). In natural cases, the stress-strain curve beyond σ_{ys} follows a non-linear path, which varies for one rock type to another, as well as between similar rock types (e.g., sandstones, see Bernabe and Brace, 1990; Ord et al., 1991; Bésuelle, 2001; Baud et al., 2006; Gautam et al., 2016, etc.). Hence, a linear hardening model is considered for the sake of simplicity. Several workers viz. Gerya and Yuen (2007), Popov and Sobolev (2008), Crameri and Kaus (2010), Tian and Buck (2019), have also assumed an elasto-visco-plastic rheology (also see review in Piazolo et al., 2019) to study ductile deformation in lithosphere-scale models.

5.2. Model setup

The 2D model is performed on a 1 by 0.5 μm^2 rectangular domain (Fig. A1a in the Appendix). Four ellipses viz. e1, e2, e3, e4, each with an aspect ratio of 4 (long axis: 0.04 μm, short axis: 0.01 μm), with the long axes perpendicular to the x-axis and rheological properties same as that of the matrix (*another two models viz. Model III, IV, wherein the Young's Moduli of the ellipses are twice as high as that of the matrix are also run, see* Fig. S9 *in the supplementary file S2 for the results*), are also included inside the rectangular matrix (Fig. A1a in the Appendix). These ellipses are included to examine the sense and magnitude of rotation of their long axes with deformation. We chose ellipses instead of circles because the long axes and their rotations are much more prominent for the former than the latter. Triangular meshing with an advancing front tessellation (Johnson et al., 2009; Ismail-Zadeh and Tackley, 2010; Tadmor et al., 2012; Fenner, 2013; Bose et al., 2018) is applied with the

help of the mesh generation module in COMSOL Multiphysics v5.4. Table A2 (in the Appendix) presents the detailed mesh statistics. Both the models are subjected to pure and simple shears assuming plane strain deformation. In Model I, the domain is subjected to pure shear followed by dextral simple shear. In Model II, the sequence of shearing is opposite. (Figs. A1, A2 in the Appendix).

Three different '*no velocity*' boundary conditions are introduced viz. (a) $U_X = 0$, (b) $U_Y = 0$, (c) $U_X = U_Y = 0$. Conditions (a) and (b) are employed on the upper boundary only during pure and simple shear deformation (as in Mukherjee, 2019), respectively. Whereas (c) acts only on the lower boundary throughout the entire run time for all the models. These conditions are necessary to inhibit deformation induced translation and rotation of the entire model/domain as a whole.

The stresses $|\sigma_X|$and$|\sigma_Y|$ act only on the upper boundary of the

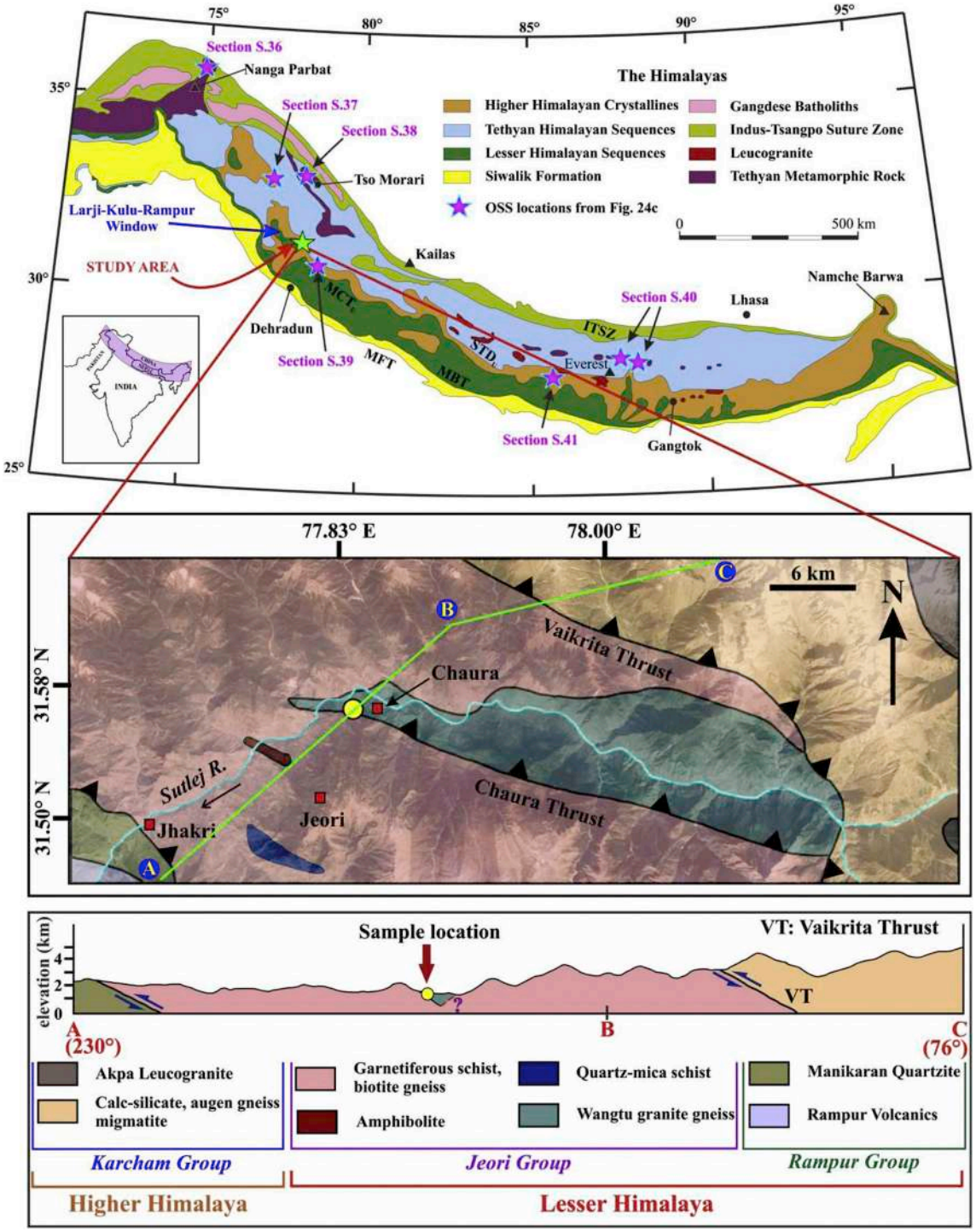

Fig. 25. Geological map of the Himalaya (reproduced from fig. 1 of Mukherjee, 2015b) and the study area (redrawn after fig. 2 of Jain et al., 2000) with the sample (S-16) location (yellow circle) (first referred at Section 7.1). Topographic image on the background was taken from Google Earth on 12-Nov-2018. ITSZ: Indus-Tsangpo Suture Zone, MBT: Main Boundary Thrust, MCT_U: Main Central Thrust upper; MFT: Main Frontal Thrust, STD_U: South Tibetan Detachment upper. The locations of OSS from other part of Himalaya (Fig. 24c) are also shown with pink stars. Also see Fig. S6 in the supplementary file S2.

domain and parallel to the x- and y-axes, respectively. Moreover, for both the models I and II $|\sigma_X|$and$|\sigma_Y|$ increase non-linearly from 0 to 400 and 800 MPa (Fig. A2 in the Appendix), respectively. Experimental studies conducted on sandstones (Ord et al., 1991; Sulem et al., 1999; Shipton and Cowie, 2003; Baud et al., 2006; Schultz et al., 2010; Soliva et al., 2013; Gautam et al., 2016) reveal that they usually undergo strain hardening/softening beyond the elastic limit, and hence deformation for a constant stress is avoided in this study. But, in opposite sequences i.e. for Model I: $|\sigma_Y|$ acts from t = 0–1 s, and $|\sigma_X|$ from t = 1–2 s (Figs. A2a,b in the Appendix), and for Model II: $|\sigma_X|$ acts from t = 0–1 s, and $|\sigma_Y|$ from t = 1–2 s (Figs. A2c,d in the Appendix). (Boundary conditions for the Models III and IV in supplementary file S2 are the same as in Models I and II).

5.3. Results & interpretations

The sense of rotation of the long axes of the ellipses during pure shear does vary across the domain as expected i.e., e1and e4 rotate in a clockwise sense, whereas it is counter-clockwise for e2 and e3 (Fig. A3, A4 in the Appendix). Although the rotation sense may differ, the amount is almost the same ~3° and ~6–7° for each of the ellipses at the end of pure and dextral simple shear deformation, respectively. Note that the final products of both the models do not show OSS i.e., the long axis of all the ellipses in Fig. A3c,g (in the Appendix) are tilted towards the right (+X-direction). Moreover, the angle of tilt (φ) also does not vary much i.e., ~ 80–81° for e1 and e4, and ~86° for e2 and e3 (The results for the Models III and IV are identical except that of the effective plastic strain, see supplementary file S2). Hence, it would be really difficult for any observer to decipher presence of OSS only by looking at the final product. The observer may well end up assigning only one set of deformation (general shear with a high dextral component as in Fig. S10).

6. Reports of OSS from across the globe (Fig. 24)

OSS has been identified from different terranes worldwide (Table 3; Fig. 24; supplementary file S1). We compile as many examples as we could; however, the list may not contain all the examples. A few examples of conflicting shear senses with non-parallel shear planes have been included. Brief descriptions for each of the terranes have been provided in the Supplementary file S1. The locations are arranged continent-wise i.e., N. America (1–8) → S. America (9–13) → Europe (14–31) → Africa (32 and 33) → Asia (34–51) → Australia (52–55) → Zealandia (Mortimer et al., 2017, 2018) (56) (Fig. 24).

7. OSS from NW Himalaya (Chaura village, Sutlej river section, Himachal Pradesh state, India) - this study

7.1. Geology

The study area lies in the vicinity of the Chaura Thrust. The lithotectonic identity of the group of rocks (categorized under the Jeori Group in Fig. 25) that lie between the Karcham Group (considered as a part of the Higher Himalayan Crystallines (HHC), Law et al. (2013)) to the north, and the sediments of the Larlji-Kulu-Rampur Window (LRKW) of the Lesser Himalayan Sequence (LHS) (Richards et al., 2005) is still debated. A sample from the region yields a *'hairpin'* P-T path, typically reported from the LHS rocks (Kohn, 2008, 2014) and a relatively young Early to Mid-Miocene prograde deformation deduced using *in-situ* monazite dating (Caddick et al., 2007). Moreover, Richards (2004) obtain an εNd (500) value of −17.7, consistent with those reported from the LHS rocks (Caddick, 2004), from the same sample. Law et al. (2013) include them within the LKRW, but both Chambers et al. (2008) and Richards et al. (2005) view it as a separate entity: The Jutogh Group (also called the Jeori Group, Fig. 25). On the other hand, Singh and Jain (1993) categorized them much earlier as the HHC rocks. In this paper, following the findings of Caddick (2004), Richards (2004), and Chambers et al. (2008), we have considered the rocks to be a part of LHS (Fig. 25).

The 9 km thick sequence (Miller et al., 2000) of Jeori metasediments (Manickavasagam et al., 1999) comprise of mylonites, mica schist, quartzites with intercalations of calc-silicates and marble (Vannay et al., 1999), and is overlain by the ~1.87 Ga Wangtu Gneissic Complex (WGC). The later consists of granitoids, granite gneiss with intercalations of mica schists (Jain et al., 2000). Towards SW, along the Sutlej valley, the pelitic to psammitic migmatite content in the 6–7 km thick WGC rises gradually (Richards et al., 2005). Jeori metasediments overlie the Proterozoic (~1.95–1.87 Ga) (Richards et al., 2005) sedimentary succession of Rampur Group (Caddick et al., 2007; Law et al., 2013) that also is recognized as an OOST (Mukherjee, 2015b), which comprises of greenschist facies metamorphosed-sediments only (Vannay et al., 1999). Interestingly, the Jeori Group exhibits inverted metamorphic sequence i.e., the grade increases from garnet to staurolite in Jeori metasediments (within ~10 km towards NE) and then goes up to sillimanite grade near the top of the WGC (Chambers et al., 2008). Vannay et al. (2004) suggest that the Lesser Himalayan Sequence (LHS), comprising of the Jeori metasediments and the WGC, reached their peak metamorphic conditions (~700 °C) during Late Miocene. Moreover, they also claim that U–Th–Pb dating of monazites from the Karcham Group (HHC) indicate peak conditions at ~ 40-22 Ma.

The WGC contains asymmetric feldspar porphyroclasts exhibiting top-to-SW shear (Grasemann et al., 1999). Moreover, evidence of top-to-SW up sense of shear is also shown by the NE dipping thrust plane viz., Vaikrita Thrust (known as MCT-II or MCT upper (MCT_U), see Godin et al., 2006; Martin, 2017) (Fig. 25).

7.2. Microstructural observations

Thin-sections of mylonitic and schistose rocks from the Sutlej River section (Fig. 25) have been studied for the presence of opposite shear senses. Major shear sense indicators viz., mineral fish of lenticle (Fig. 26) and parallelogram shapes (Fig. 27) are present. Most of them are preserved elegantly (e.g., Fig. 26k,m,n & 27) and denote the shear senses. Moreover, examples of OSS bounded by the same as well as different (but parallel) sets of C-planes, are most prominent within the samples from the location S-16 in Fig. 25. Few more evidences of ductile shearing are shown by sigmoidal quartz fish (Fig. 28, also see Fig. S7 in the supplementary file S2). 7 of them exhibit top-to-N shear sense (Fig. 28a,c,e,g,i,k & S7a,e), whereas 2 show top-to-S shear sense. Quartz grains with irregular margins (Fig. S8a in the supplementary file S2) and symmetric geometry (Fig. S8b in the supplementary file S2) are avoided in deciphering the shear sense. It should be noted that the quartz fish in Fig. 28f is present adjacent to the mica fish, and both of them exhibit similar sigmoidal shapes. This is, however, not always the case as shown in Fig. S8c (supplementary file S2). Unlike the mica fish of Figs. 26–27, the quartz fish are widely separated in the thin-sections, and hence could not be encapsulated into a single image. However, the mica fish from Fig. 26m (top-to-S shear) is present at the bottom of Fig. 28f in which the quartz fish shows top-to-N shear. The rest of the samples up to Jhakri, which is ~12 km SW from S-16, show little or no evidence of OSS.

In all these samples, the recrystallized muscovite and biotite grains define the foliation/shear planes. Sometimes, the recrystallized

muscovite grains occur along the boundaries of coarser muscovite grains as well as around quartz grains. For close-spaced cleavage domains (CD), quartz and feldspar grains are finer, whereas coarser grains are found where CDs are more widely separated. C-planes are rarely curved, but the angle between S- and the C-planes for top-to-south shear vary over a wider range (10–35°) than that for top-to-north shear (30–40°).

Apart from these, other quartz recrystallization features viz. bulging (BLG; Stipp et al., 2002a,b) (Fig. 29a and b) and grain boundary migration (GBM; Stipp et al., 2002a,b) (Fig. 29a,c) recrystallization are observed as well, along with chessboard extinction in quartz (Fig. 29d), which indicates high deformation temperature (>700 °C; Wallis et al., 2019). The samples also consist of intensely kinked muscovite (Fig. 29e) and thin interconnected micro-shear zones, which are characterized by grain-size reduction (Fig. 29f). Such a texture may have arisen due to deformation/strain partitioning (Larson et al., 2014) or exhumation/decompression induced retrogression (Cao et al., 2017). The exact cause, however, is unclear at present and needs to be looked into in detail.

8. Discussions

8.1. General comments

Shear sense indicators and their applications have so far been the focus of the research works of structural geologists while dealing with ductile and brittle shear zones. These hold crucial kinematic information based on which stress regime and tectonic models are established (Fossen and Cavalcante, 2017). The origin of individual shear sense indicators has already been studied in detail (e.g., Hanmer and Passchier, 1991; ten Grotenhuis et al., 2003; Passchier and Trouw, 2005; Mukherjee, 2011 etc.), along with the necessary precautions to be taken care of while interpreting them (e.g., Bell and Johnson, 1992). But in this article, we have noticed that opposite shear senses from a single terrane or even from the same outcrop have been reported. Consequently, the onus lies upon the observer to construe the cause of its presence/origin, and thus correlate it with the deformation phases deciphered from other structural features or petrological studies (preferably both).

8.2. Mechanisms and plausible tectonic scenario(s)

OSS can either arise out of single or multiple deformation phase(s) (global examples in Table 3). This review, although not claimed to be exhaustive, lists most of the reports of OSS from all over the globe. OSS due to a single deformation phase have been reported from 10 out of the total of 56 cases we present. As explained in Section 4.1, seven major mechanisms have been put forward by previous workers to such OSS viz. *(i)* interaction between fracture and bedding interface (Cooke and Underwood, 2001); *(ii)* viscosity heterogeneity (Ishii, 1992), *(iii)* strain rate contrast (Hippertt and Tohver, 1999), *(iv)* back rotation (Ghosh and Ramberg, 1976; Fossen, 2016), *(v)* rigid block rotation and mutual interaction (MacLeod and Murton, 1995), *(vi)* folding (Twiss and Moores, 2007; Sengupta and Chatterjee, 2015), and *(vii)* stretching faults (Means, 1989, 1990). Of these, cases *(i)* and *(iv)* are purely based on experimental results/theoretical concepts and are yet to be substantiated with natural examples. However, cases *(ii)*, *(iii)* and *(vii)* although proposed based on numerical/analog experiments, were later validated from microstructural (*(ii)* and *(iii)*: Hippertt and Tohver, 1999) as well as from field (*(vii)*: Kossak-Glowczewski et al., 2017) observations by as well. The rest, on the other hand, i.e., cases *(v)* and *(vi)* were proposed based on field findings, on which experimental validation is required. Apart from these, pure shear-dominated deformation can also result in OSS (Bell and Johnson, 1992; also see the Appendix for our analyses). Furthermore, observations at outcrop- and micro-scale from a few terranes viz. Mabja Dome, Tibet (Langille et al., 2010), D'Entrecasteaux Islands, Papua New Guinea (Little et al., 2013), and Major Gercino Shear Zone, Brazil (Hueck et al., 2018a,b), have corroborated the pure shear theory.

Majority of the OSS owe their origin to multiple deformation phases: *(i)* inversion tectonics/fault reactivation (Turner and Williams, 2004; Javadi et al., 2015 & references therein), *(ii)* exhumation of subducted crustal slices (Brueckner and Cuthbert, 2013), *(iii)*

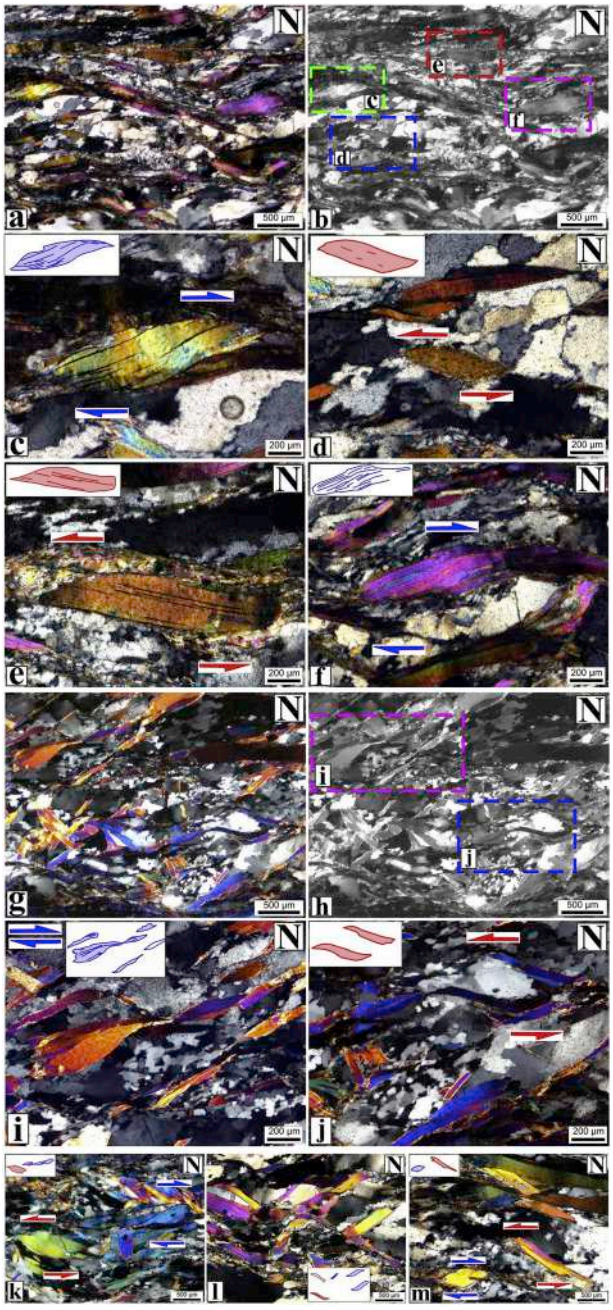

Fig. 26. OSS observed under an optical microscope from the schistose rock near Chaura village (Fig. 25) (NW Himalaya, Uttarakhand state, India) (first referred at Section 7.2). Sigmoid mica fish with bent cleavages and undulose extinction. Gray-scale version of (a) and (g) shown in (b) and (h), respectively, to demarcate the positions of (c,d,e,f,i,j). (c,f,i) Top-to-N shear (blue half-arrows). (d,e,j) Top-to-S shear (red half-arrows). The C-shear plane in all the images is horizontal. Few images (k,l,m) show both the shear senses (see Figs. 24 and 25 for the location of the sample). The insets show line sketches of the mica fish. Blue and red colored boundaries indicate shear senses corresponding to the same half-arrows with the same colors. The dotted rectangles in gray-scale images indicate the locations of the images given by the letters inside them.

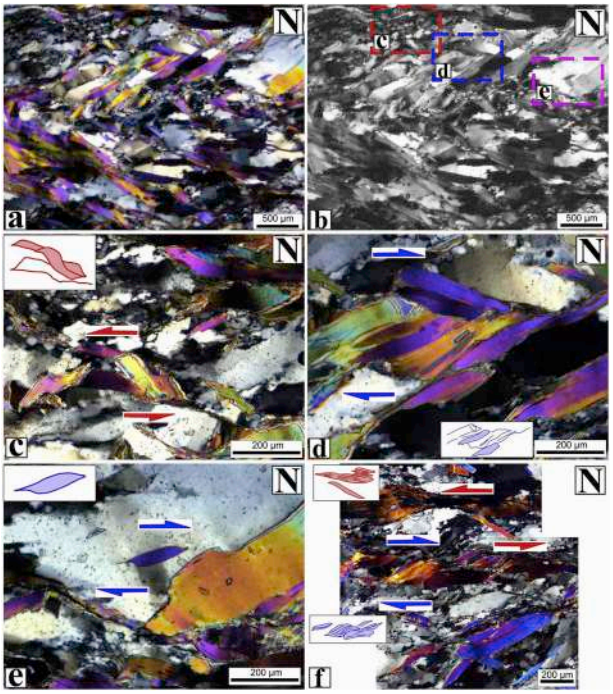

Fig. 27. OSS from thin-sections of the schistose rock near Chaura village (Fig. 25) (NW Himalaya, Uttarakhand state, India) (first referred at Section 7.2). (a) A fold with the axial trace nearly parallel to the foliation of the rock. Gray-scale version of (a) shown in (b), to demarcate the positions of (c,d,e). Sigmoid (c,d,f) and parallelogram (e) mica fish with bent cleavages displaying undulose extinction. The boundaries are partly destroyed by recrystallization. (c) Top-to-S shear (red half-arrows). (d,e) Top-to-N shear (blue half-arrows). (f) Both top-to-N and top-to-S shears are present. The dotted rectangles in gray-scale images indicate the locations of the images given by the letters inside them.

overturning or tilting of faults or litho-sequences (Lim and Cho, 2012), *(iv)* orogenic collapse (Bell and Newman, 2006), and *(v)* isostatic adjustment (Wernicke and Axen, 1988) etc. Of these, cases *(i)* and *(iii)* usually associate with sedimentary basins, e.g., the Franklinian Basin (Canada) (Table 3; De Paor and Eisenstadt, 1987), the Otway Basin (Australia) (Table 3; Holford et al., 2014), and the Chungnam Basin (S. Korea) (Table 3; Lim and Cho, 2012). However, fault reactivation, which is also considered under case *(i)*, does not necessarily restrict to basin deposits e.g., Beishan Terrane (China) (Table 3; Zhang and Cunningham, 2012), Donureh Fault System (Iran) (Table 3; Javadi et al., 2015), Yukon River Shear Zone (Canada) (Table 3; Parsons et al., 2018) etc. Further, reorientation of the principal stress axes is a necessity only for case *(i)*. Interestingly, of all the examples of OSS discussed here that originated due to multiple deformation events, change in regional stress distribution (Fig. 30) is required for half of the cases (blue colored locations in Table 3). Also, we note that the locations are mostly concentrated along Phanerozoic orogens/fold-thrust belts i.e., the Himalaya, Alps, Variscan, Caledonides, North American Cordillera, etc. The reason could either possibly be the severe complexity of the deformational history (Bell and Johnson, 1992; Jamieson and Beaumont, 2013), or the fact that these regions have gained more attention and hence were studied more intensely, or both. Several of the examples (locations 5, 9–13, 33, 35, 42–44, 47–49, 53, and 54 in Fig. 24 and Table 3) lie within Precambrian cratonic shield at present. Apart

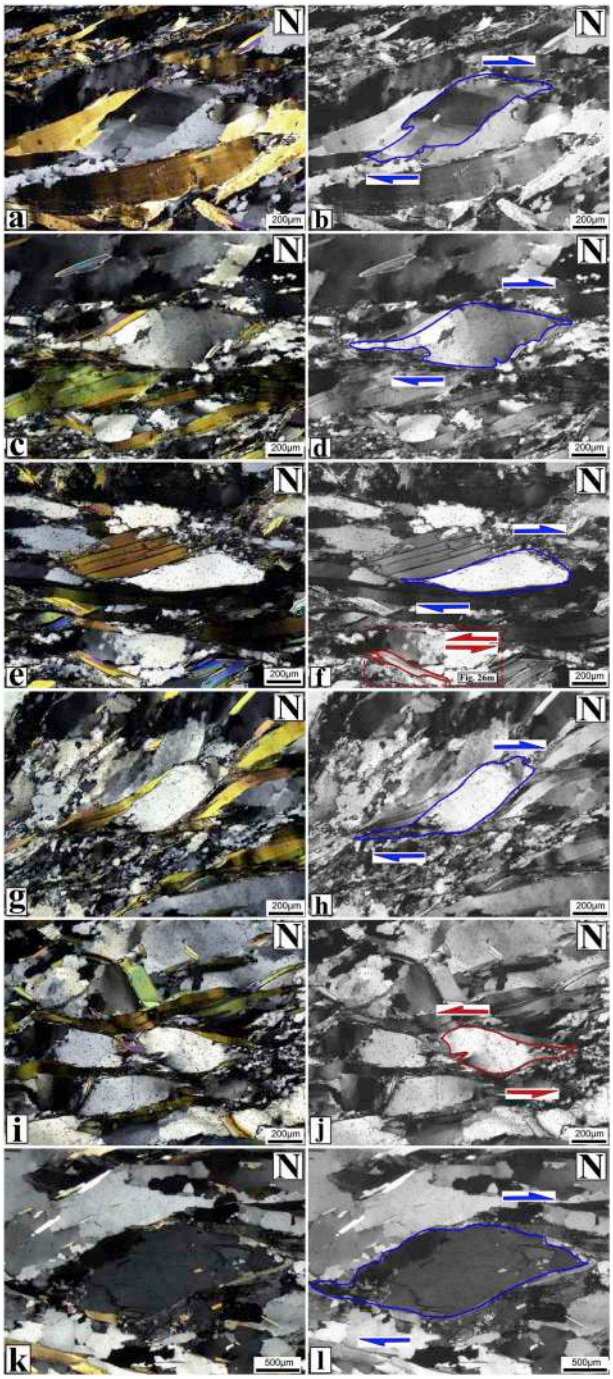

Fig. 28. Ductile OSS indicators from the schistose rock near Chaura village (Fig. 25) (NW Himalaya, Uttarakhand state, India) (first referred at Section 7.2). Sigmoidal quartz fish show (a-h,k,l) top-to-right (N) and (i,j) top-to-left (S) shear senses. Undulose extinction, typical of deformed quartz, is clearly visible in (a). Muscovite fish, below the quartz fish in (f) show a top-to-left (S) shear. This is also the same muscovite fish from Fig. 26m as marked inside the red rectangle. The mica and quartz fish in (e,f) both indicate the same shear sense. (b), (d), (f), (h), (j), and (l) are gray-scale versions of (a), (c), (e), (g), (i), and (k).

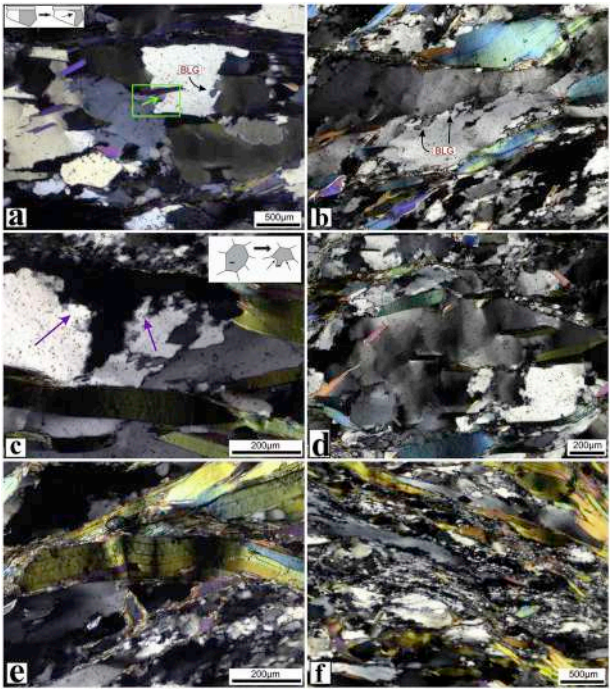

Fig. 29. Quartz and muscovite deformation microstructures from the schistose rock near Chaura village (Fig. 25) (NW Himalaya, Uttarakhand state, India) (first referred at Section 7.2). (a) Dragging microstructure in quartz. The green arrow shows the direction of grain boundary migration (GBM). It indicates of deformation at 550–700 °C (Stipp et al., 2002a,b). Evidence of bulging (BLG) recrystallization (270–390 °C; Stipp et al., 2002a,b) are also shown in (a) and (b). (c) Pinning microstructure in quartz suggestive of GBM recrystallization (550–700 °C; Stipp et al., 2002a,b). Purple arrows denote migration direction. (d) Chessboard extinction (> 700 °C; Kruhl, 1996; Chakraborty and Mukul, 2019; Wallis et al., 2019) in a quartz grain. (e) Intensely kinked muscovite grain exhibiting deformation-induced undulose extinction. Kink axes are formed near-perpendicular to the cleavages. (f) Grain-size reduction in the quartzo-feldspathic matrix. Thin zones of interconnected fine-grained quartz and feldspar between elongated medium-sized quartz ribbon. The microscopic stage was rotated to avoid extinction of the muscovite grains, and thus clearer visualization of the foliation plane. Cartoons in (a) and (c) have been redrawn from Fig. 3.34 of Passchier and Trouw (2005).

from these, STTFZ (Cyprus) (Table 3, see supplementary file S1) and Wadi kid (Egypt) (Table 3, see supplementary file S1) belong to transform and extensional settings, respectively.

8.3. Zagros and Andes: special cases?

We observe no reports of OSS so far from the Andes and the Zagros fold-and-thrust belt (ZFTB). As we have noticed so far, OSS in fold-thrust belts are mostly results of either gravitational collapse (e.g., Nepal Himalaya, North American Cordillera; Table 3, Fig. 24) or reorientation of principal stress axes (Fig. 29) (e.g., Apennines, Eastern Alps; Table 3, Fig. 24, see supplementary file S1). Unlike the Himalaya, gravitational collapse has not yet been reported from the ZFTB except for in the synorogenic siliciclastic deposits (Pirouz et al., 2011) of the Agha Jari Formation (Middle Miocene-Pliocene), where Sarkarinejad et al. (2018) identify a normal fault. Also, as far as stress reorientation is concerned, paleostress reconstructions using fault-slip data (Mesozoic normal faults, and Late Cenozoic strike-slip as well as reverse faults) and fractures present within the ~10 km thick sedimentary cover (Paleozoic-Cenozoic) of the ZFTB reveal that the stress state has changed from extensional (~N–S to ~ NE-SW oriented σ_3 axis in Triassic – Jurassic, and Jurassic – Cretaceous, respectively) to compressional (σ_1: ~ NE-SW, σ_3: vertical, Oligocene – Early Miocene). This was followed by strike-slip tectonics (σ_1 axis: ~ NE-SW, and σ_2: vertical, Early Miocene – Post Pliocene). The orientation of σ_1 in itself has varied from N058° to N002°during the strike-slip regime (Navabpour et al., 2007, 2008; 2014; Navabpour and Barrier, 2012; Tavani et al., 2018). The present-day shortening direction in the region, as estimated from GPS studies, ranges N025°to N068° (Lacombe et al., 2007; Rajabi et al., 2010; Heidbach et al., 2018). Given the reorientation of stress axes in the ZFTB, detailed structural studies need to be carried out to extract evidences of OSS.

On the other hand, gravitational collapse has been widely documented from the Andes (Dalmayrac and Molnar, 1981; Sébrier et al., 1985, 1988; Wörner et al., 2002). Giambiagi et al. (2016) derive paleostress tensors using over 650 fault-slip data from Central Andes (22–26° S). The authors identify two distinct phases of geodynamic evolution for the region: *(i)* compressional (~20–13 Ma), followed by *(ii)* gravitational collapse (<13 Ma). Furthermore, they suggest that the stress states varied from case *(i)* to case *(ii)* and within case *(ii)* as well. The stress regime changed as follows: σ_1: ~ E-W, σ_2: ~ N–S, σ_3: vertical (*case i*) → σ_1: ~ E-W, σ_2: vertical, σ_3: ~ N–S → σ_1: ~ N–S, σ_2: vertical, σ_3: ~ E-W → σ_1: ~ N–S, σ_2: ~ E-W, σ_3: vertical (*case ii*). 2D numerical models of Liu et al. (2000) and Husson and Ricard (2004) also predict a N–S extension in the Central Andes due to crustal collapse. However, Flesch & Kreemer (2010) propose that the extension direction varies from ~ NE-SW at northern Chile to ~ E-W further south along the Central Andes. In support of these findings, Tibaldi and Bonali (2018) report Plio-Quaternary normal faults whose trends change from ~ N–S in the south of central Andes to ~ NW-SE to the north. ~ N–S striking Quaternary normal faults were also identified within 30° S to 31° S latitudes by Heinze (2003). GPS studies, too, reveal an ~ E-W neotectonic extension (Khazaradze and Klotz, 2003; Klotz et al., 2006). Mercier et al. (1992), study the faults in the region and proposed a switch in the extensional direction from E-W (Miocene - Pliocene) to N–S (Pleistocene) in the High Andes. Early Cretaceous extensional basins were aplenty along the margin of the Central Andes that developed in response to the E-W extension (Late Jurassic – Early Cretaceous) but got obliterated by the Cenozoic Andean shortening (Mpodozis and Allmendinger, 1993; Ramos, 2010; Armijo et al., 2015; Horton, 2018). Although there are reports of reactivation of a few favorably oriented pre-Andean extensional faults as (oblique-) thrusts (positive inversion, Section 4.2.1), the workers do not present evidences of OSS from the same region (Schmidt et al., 1995; Kley and Monaldi, 2002; Webster et al., 2004; Iaffa et al., 2011; Winocur et al., 2015; Perez et al., 2016).

8.4. OSS and hydrocarbon prospect

Cooper and Warren (2010) brilliantly review how positive tectonic inversion i.e., thrusting along a pre-existing extensional fault (Section 4.2.1) can affect a petroleum system. Positive inversions can either create new traps or modify pre-existing traps and trigger migration of the hydrocarbons from pre-to post-inversion traps. The degree of inversion plays a crucial role since too much upliftment can expose the overburden rocks resulting in erosion and hence, leakage of hydrocarbon reserves (Doré et al., 2000, 2002). Similar damage may arise from faulting of the reservoir rocks (Pei et al., 2015). Mechanically dead faults are hydraulically dead and act as barriers to hydrocarbon migration. On the other hand, reactivated faults act as excellent pathways for the same and result in leakage (Barton et al., 1995; Zoback, 2007). Moreover, both upliftment prior to maturation of the source rock (also called maturation 'switch-off') and rapid uplift post-maturation, are detrimental to hydrocarbon prospectivity. Sudden pressure release due to rapid uplift can trigger: (a) failure of the top seals, (b) gas expansion, which in turn may cause oil spillage. However, upliftment has positive effects on the petroleum systems as well viz. increased permeability due to fracturing of reservoir rocks (e.g. tight sandstones), reduction in drilling costs due to remigration of hydrocarbon to reservoirs present at shallower depths, methane exsolved from the formation waters (Cramer et al., 2002) due to pressure reduction can

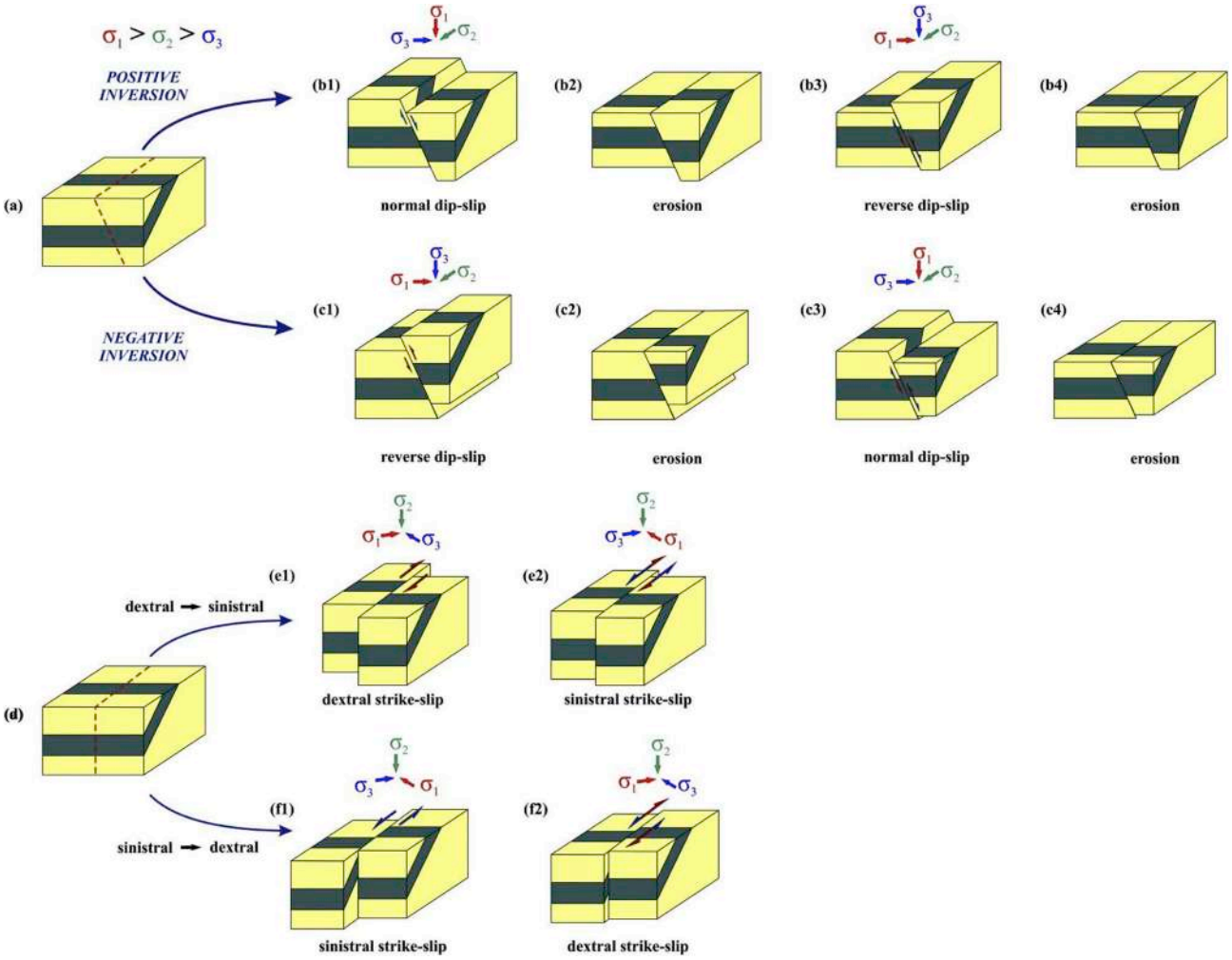

Fig. 30. Block diagrams showing reactivation of pre-existing fault planes with opposite movement sense due to reorientation of the principal stress axes (first referred at Section 8.2). (a) Pre-faulting condition. Red-dashed line shows the future fault plane. Both the scenarios of normal movement followed by reverse movement (b1-b4) and vice versa (c1-c4) have been shown. The orientations of the principal stress axes for each of the tectonic event is given above the corresponding blocks.

charge natural gas pools. The distribution of the seal, reservoir and the source rock depend upon the pre-inversion extensional phase as well (Gawthorpe and Leeder, 2000). However, inversion structures can often be confused with flower structures or overlooked in a fold-thrust belt dominated by thin-skinned tectonics (Cooper and Warren, 2010). Consequently, one must be careful, since the identification of tectonic inversion in sedimentary basins can provide insight into the geodynamic evolution of the region. It can then be correlated with the timing of the processes viz. hydrocarbon generation, migration and trapping, to decipher (with reasonable confidence) whether the components of the petroleum system survived inversion or not (e.g. Bristol Channel basin: UK, Nemčok et al., 1995; San Jorge Basin: Argentina, Uliana et al., 1995; Danish Central Graben: Denmark, Vejbaek & Andersen, 2002). If yes, then what could be the distribution of the source rocks/hydrocarbon traps over the region (Hardman et al., 1993; Grogan et al., 1999; Holmes et al., 1999)? A detailed field-based study including identification of inversion structures thus constitutes a crucial part of the reconnaissance survey and contributes significantly towards the evaluation of the hydrocarbon prospects of an area.

8.5. OSS from Chaura

Our thin-section studies conducted on the oriented samples from the vicinity of the Chaura village (Himachal Pradesh Himalaya, India) show the presence of mica fish exhibiting OSS (top-to-N and top-to-S). Temporal relationship between the shear senses could not be derived due to the absence of cross-cut relations between the C-planes that bound those asymmetric shear sense indicators. Detailed thermo-barometric studies of the samples from the area along with in-situ Ar–Ar dating (Mulch and Cosca, 2004) of the sheared muscovites could shed some light on the same. But, such a near-equal abundance of top-to-N and top-to-S possibly appears to be a product of single deformational event and may have developed under dominantly coaxial shear (Little et al., 2013). We cannot, however, completely discard possibilities such as viscosity heterogeneity (Section 4.1.2) or strain-rate contrast (Section 4.1.3). In both cases, kinematic indicators exhibiting OSS should lie within two different layers, which has been seen (Fig. 26a–j,27), but not always (Fig. 26k–m). Back rotation (Section 4.1.4), on the other hand, have so far been described only for porphyroclasts (Ghosh and Ramberg, 1976; Fossen, 2016), whereas we have identified OSS from naked clasts such as mica fish. Furthermore, OSS is dominant mostly in the samples close to the Chaura Thrust (Fig. 25), which is an OOST (Mukherjee, 2015b). Reverse shear from an OOST in a collisional orogen, to our knowledge, is the first ever report.

9. Conclusions

(i) OSS is present in many shear zones across the globe, especially at orogenic belts. 16 locations belong to Precambrian cratonic shields. However, proper cautions must be exercised in their

identification to avoid misinterpretations.

(ii) It appears that multiply deformed terranes, which have undergone orthogonal switching of the principal stress axes (both local and/or regional), are more likely to exhibit OSS.

(iii) Tectonic inversion, a major cause of producing OSS, of sedimentary basins play a crucial part in hydrocarbon prospectivity. Hence, the structural evolution of basins should be vigorously studied with special emphasis on the identification of OSS.

(iv) The equal abundance of OSS in the mylonitic sample from the HHC reveals dominance of coaxial deformation at some stage of its tectonic evolution. Pure shear flattening has been previously reported from different portions of the HHC.

(v) Numerical simulations conducted using COMSOL Multiphysics v5.4 (Section 5) show that the sense of rotation of elliptical inclusions does change across the matrix due to pure shear. So does the amount of rotation. Competency contrast between the elliptical inclusions and the matrix affects the magnitude of the effective plastic strain but neither the magnitude nor the sense of rotation.

Acknowledgements

This is a part of DD's Ph.D. work funded by the University Grants Commission (New Delhi, India) Junior Research Fellowship grant number: F. 2-2/1998 (SA-1). SM was supported by a research sabbatical for the year 2017 granted by IIT Bombay. Discussions with Narayan Bose (Post-Doctoral Fellow, Department of Geology & Geophysics, IIT Kharagpur) has been beneficial. Rocks sample from Chaura came from the fieldwork conducted by Rajkumar Ghosh and SM in 2014. Suggestions received from the Research Progress Committee members, George Mathew and Prabhakara Naraga (IIT Bombay), in several rounds have been beneficial. The authors thank Dr. Paris Xypolias and an anonymous reviewer for their comments, which significantly improved the manuscript. The editorial handling of Dr. Ian Alsop is greatly appreciated. We apologize in case we missed any references: this has been unintentional. SM's first study on reverse shear was submitted as a report: Mukherjee and Pal (2000).

Appendix A. Supplementary data

Supplementary data to this article can be found online at https://doi.org/10.1016/j.jsg.2019.05.008.

APPENDIX

A.1 Governing Equations

The total elastic strain tensor for an elastic-plastic material is (Mao-Hong et al., 2006; Hashiguchi, 2014; Hobbs and Ord, 2015):

$$\varepsilon = \varepsilon_{el} + \varepsilon_0 + \varepsilon_{th} + \varepsilon_p + \varepsilon_c \quad \text{(i)}$$

Here, ε, ε_{el}, ε_0, ε_{th}, ε_p, ε_c are the total, elastic, initial, thermal, plastic, and creep strain tensors.
However, in our case $\varepsilon_0 = \varepsilon_{th} = \varepsilon_c = 0$ and therefore

$$\varepsilon = \varepsilon_{el} + \varepsilon_p \quad \text{(ii)}$$

Material with an elasto-plastic rheology also follow the plastic flow rule:

$$\dot{\varepsilon}_p = \lambda \frac{\partial Q}{\partial \sigma} \text{ (for } \lambda \geq 0) \quad \text{(iii)}$$

where, $\dot{\varepsilon}_p$= incremental plastic strain, λ = plastic multiplier, σ: second Piola-Kirchhoff stress, Q: plastic potential and $\frac{\partial Q}{\partial \sigma}$= potential gradient.

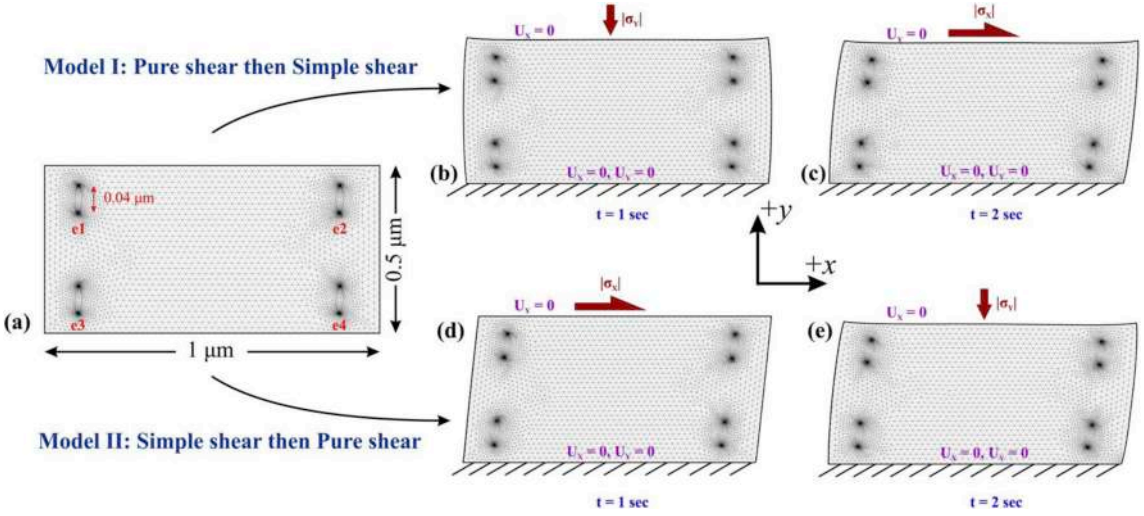

Fig. A1. Nomenclature, boundary conditions, and meshing of the models (first referred at Section 5.1). (a) Model setup before deformation. Triangular meshing adopted for both the models, (b,c) Model I: Pure shear followed by dextral simple shear, and (d,e) Model II: Dextral simple shear followed by pure shear. The ellipses are e1, e2, e3, and e4. In both the cases, the lower boundary of the domain was kept stationary ($U_X = U_Y = 0$). Similarly, during pure shear for both the models I and II, the movement of the upper boundary of the domain along the X-axis is inhibited ($U_X = 0$). However, during simple shear, the upper boundary is free to move along the X-axis but not along the Y-axis ($U_Y = 0$). The final products at the end of t = 1 s (b,d) and t = 2 s (c,e) are only shown.

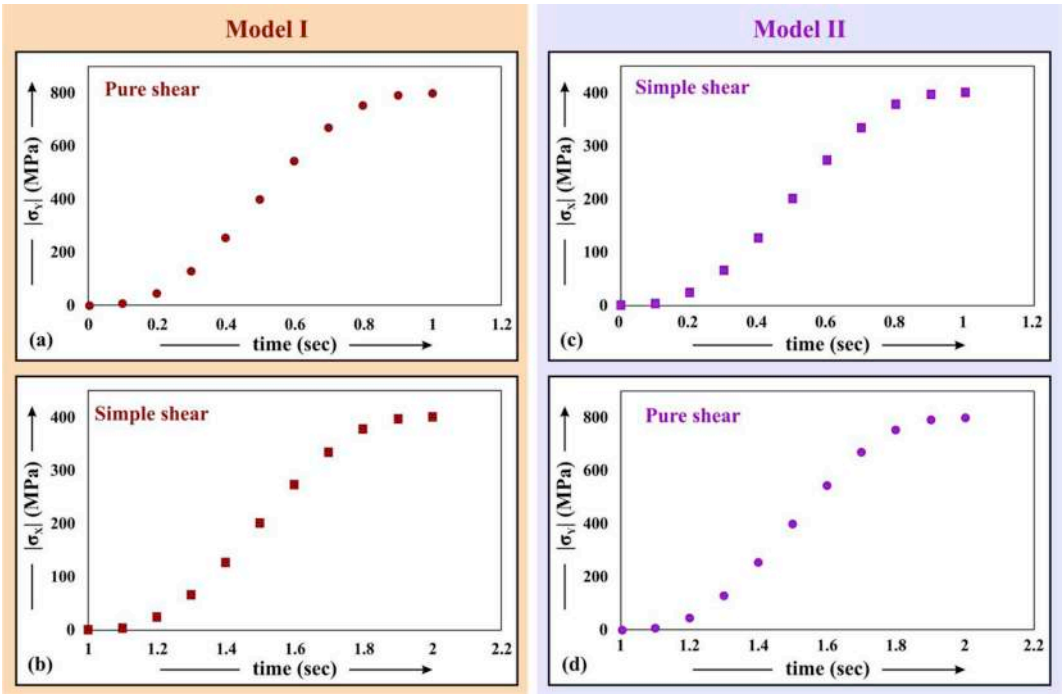

Fig. A2. Temporal variation of the stress magnitudes for (a,b) Model I and (c,d) Model II (first referred at Section 5.1). Time stepping for each of the deformation is 0.1 s such that stress magnitudes within the intervals ≤0.1 s, e.g. t = 0.2–0.3 s or t = 1.4–1.5 s, are unknown. Hence, the data points have not been connected with a curve.

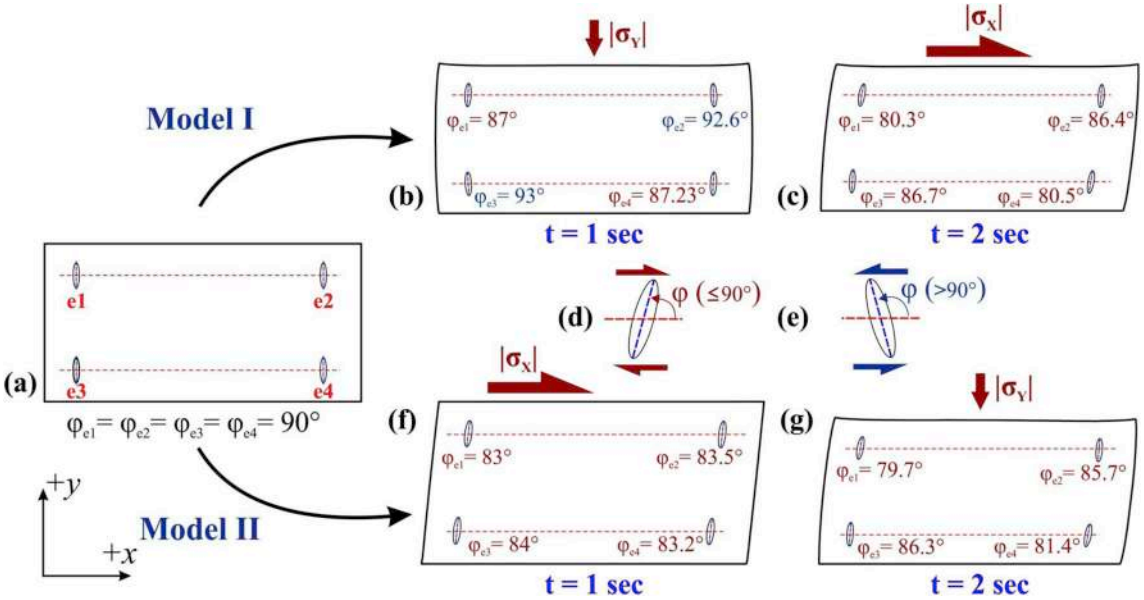

Fig. A3. Deformation induced rotation of the ellipses (first referred at Section 5.3). (a) Pre-deformational setup. All the angles are measured with reference to the red dotted lines, whereas the blue dotted lines indicate the long axes of the ellipses. The angle (φ) between the ellipses and the +X-axis, at the end of each deformation stages, are stated for both the Models I (b,c) and II (f,g). Angles were measured in a counter-clockwise sense for both (d) dextral and (e) sinistral rotations. Red- and blue colored texts present the acute and obtuse angles.

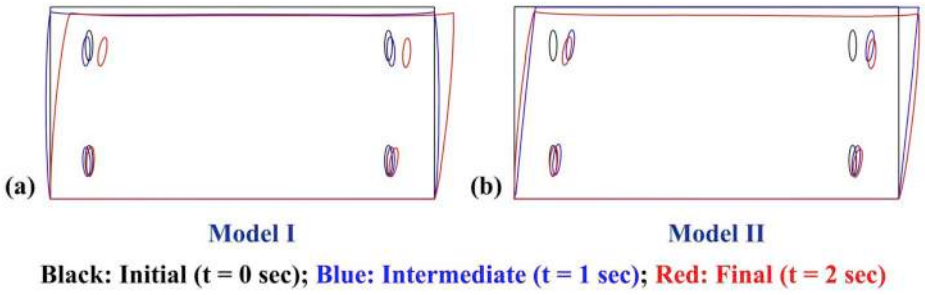

Fig. A4. Initial model setup, intermediate and final stages of deformation for both (a) Model I and (b) Model II (first referred at Section 5.3).

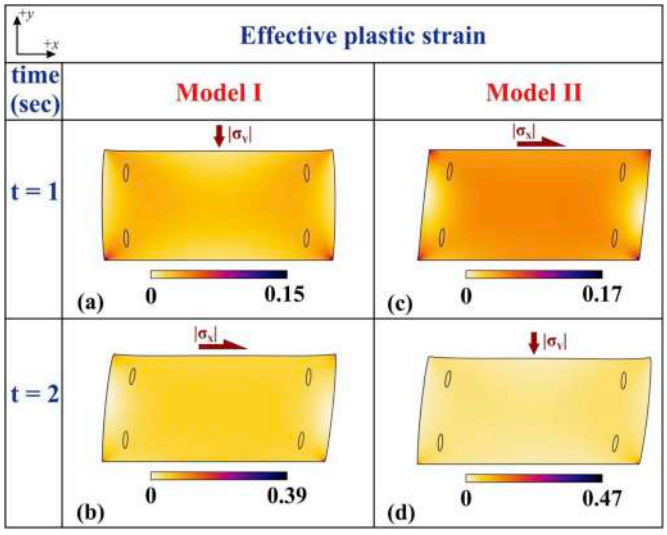

Fig. A5. Effective plastic strain at the end of each deformation (at t = 1 and 2 s) for (a,b) Model I and (c,d) Model II (first referred at Section 5.3).

Table A1
Physical parameters of the material used.

Material	Density[1,2] (kg m $^{-3}$) §	Young's Modulus[1,2,3] (GPa) §	Poisson's Ratio[1,2, §]	Initial Yield Stress[4,5,6,7,8] (MPa) §§	Isotropic Tangent/Hardening Modulus[9,10,11] (GPa)
Sandstone	2000-2800[1, 2]	10–60	0.1–0.3	54–420[5,6]	0.4–35

Data references: 1. Gudmundsson (2011), 2. Henderson and Henderson (2009), 3. Małkowski et al. (2018), 4. Bernabe and Brace (1990), 5. Wong et al. (1997), 6. Baud et al. (2006), 7. Louis et al. (2006), 8. Wang et al. (2018), 9. Ord et al. (1991), 10. Herrin (2008), 11. Duda and Renner (2013) #
Note:§ Mean values of the parameters are used in the model i.e. Density = 2400 kg m^{-3}, Young's Modulus = 35 GPa, Poisson's ratio = 0.2.
§§ Majority of the values lie within the range 150–200 MPa, hence the mean of this range i.e. 175 MPa has been used.
# The values of experimentally determined hardening modulus show an increase with decreasing strain rates, and the highest value was experimentally determined for a strain rate of 10^{-7} s^{-1} (geological strain rates at micro-scale vary from 10^{-13} – 10^{-8} s^{-1}; Fagereng and Biggs, 2019).

Table A2
Pre- and post-deformational statistics of the mesh configurations for both the models at the end of each deformation stage.

	Study step	Mesh Area (μm^2)	No. of Mesh Vertices	No. of Triangular elements	No. of Edge elements	No. of Vertex elements	Element Size (minimum, maximum) (μm)	Maximum element growth rate*	Curvature factor*	Minimum element quality*	Average element quality*
Pre-deformation set up	nil	0.5000	5563	10959	389	20	0.000075, 0.02	1.2	0.25	0.4925	0.8476
Model 1	*Step 1*: Pure shear	0.4880	5312	10451	379	20	0.0003, 0.0686	1.3	0.3	0.4876	0.8485
	Step 2: Dextral Simple shear	0.4893	5356	10516	403	20	0.0003, 0.0706			0.4943	0.8484
Model 2	*Step 1*: Dextral Simple shear	0.5014	5573	10974	394	20	0.0003, 0.0707			0.4847	0.8513
	Step 2: Pure shear	0.4893	5282	10390	382	20	0.0003, 0.0708			0.4839	0.8439

*: Unitless quanitites.

References

Agarwal, A., Agarwal, K.K., Bali, R., Prakash, C., Joshi, G., 2016. Back-thrusting in lesser Himalaya: evidences from magnetic fabric studies in parts of almora crystalline zone, kumaun lesser Himalaya. J. Earth Sys. Sci. 125, 873–884.

Aiyama, K., Mizoguchi, K., Hirano, K., Takizawa, S., 2019. Effects of sample preparation on the microstructural signatures of faulting in clay-bearing fault gouge. J. Struct. Geol. 126, 100–108.

Allen, M.B., Şengör, A.M.C., Natal'in, B.A., 1995. Junggar, turfan and alakol basins as late permian to? Early triassic extensional structures in a sinistral shear zone in the altaid orogenic collage, central Asia. J. Geol. Soc. 152, 327–338.

Alsop, G.I., 1994. Relationships between distributed and localized shear in the tectonic evolution of a Caledonian fold and thrust zone, northwest Ireland. Geol. Mag. 131, 123–136.

Alsop, G.I., Carreras, J., 2007. The structural evolution of sheath folds: a case study from Cap de Creus. J. Struct. Geol. 29, 1915–1930.

Alsop, G.I., Holdsworth, R.E., 2004. The geometry and topology of natural sheath folds: a new tool for structural analysis. J. Struct. Geol. 26, 1561–1589.

Alsop, G.I., Holdsworth, R.E., 2006. Sheath folds as discriminators of bulk strain type. J. Struct. Geol. 28, 1588–1606.

Alsop, G.I., Holdsworth, R.E., 2012. The three dimensional shape and localisation of deformation within multilayer sheath folds. J. Struct. Geol. 44, 110–128.

Alsop, G.I., Holdsworth, R.E., McCaffrey, K.J.W., 2007. Scale invariant sheath folds in salt, sediments and shear zones. J. Struct. Geol. 29, 1585–1604.

Anandarajah, A., 2011. Computational Methods in Elasticity and Plasticity: Solids and Porous Media. Springer, Berlin, 978-1-4419-6379-6pp. 328–332.

Argles, T.W., Edwards, M.A., 2002. First evidence for high-grade, Himalayan-age syn-convergent extension recognised within the western syntaxis—nanga Parbat, Pakistan. J. Struct. Geol. 24, 1327–1344.

Armijo, R., Meyer, B., Hubert, A., Barka, A., 1999. Westward propagation of the north anatolian fault into the northern aegean: timing and kinematics. Geology 27, 267–270.

Armijo, R., Lacassin, R., Coudurier-Curveur, A., Carrizo, D., 2015. Coupled tectonic evolution of Andean orogeny and global climate. Earth Sci. Rev. 143, 1–35.

Axen, G.J., Bartley, J.M., Selverstone, J., 1995. Structural expression of a rolling hinge in the footwall of the Brenner Line normal fault, eastern Alps. Tectonics 14, 1380–1392.

Barnes, J.D., Selverstone, J., Sharp, Z.D., 2004. Interactions between serpentinite devolatilization, metasomatism and strike-slip strain localization during deep-crustal shearing in the Eastern Alps. J. Metamorph. Geol. 22, 283–300.

Barnhoorn, A., Bystricky, M., Burlini, L., Kunze, K., 2004. The role of recrystallisation on the deformation behaviour of calcite rocks: large strain torsion experiments on Carrara marble. J. Struct. Geol. 26, 885–903.

Barton, C.A., Zoback, M.D., Moos, D., 1995. Fluid flow along potentially active faults in crystalline rock. Geology 23, 683–686.

Bastida, F., Aller, J., Fernandez, F.J., Lisle, R.J., Bobillo-Ares, N.C., Menendez, O., 2014. Recumbent folds: key structural elements in orogenic belts. Earth Sci. Rev. 135, 162–183.

Baud, P., Vajdova, V., Wong, T.F., 2006. Shear-enhanced compaction and strain localization: inelastic deformation and constitutive modeling of four porous sandstones. J. Geophys. Res. Solid Earth 111. https://doi.org/10.1029/2005JB004101.

Beaudoin, A., Augier, R., Jolivet, L., Jourdon, A., Raimbourg, H., Scaillet, S., Cardello, G.L., 2017. Deformation behavior of continental crust during subduction and exhumation: strain distribution over the Tenda massif (Alpine Corsica, France). Tectonophysics 705, 12–32.

Beaumont, C., Jamieson, R.A., Nguyen, M.H., Lee, B., 2001. Himalayan tectonics explained by extrusion of a low-viscosity crustal channel coupled to focused surface denudation. Nature 414, 738–742.

Beaumont, C., Jamieson, R.A., Nguyen, M.H., Medvedev, S., 2004. Crustal channel flows: 1. Numerical models with applications to the tectonics of the Himalayan–Tibetan orogen. J. Geophys. Res. 109. https://doi.org/10.1029/2003JB002809.

Beaumont, C., Nguyen, M., Jamieson, R., Ellis, S., 2006. Crustal flow models in large hot orogens. In: In: Law, R.D., Searle, M.P., Godin, L. (Eds.), Channel Flow, Ductile Extrusion and Exhumation in Continental Collision Zone, vol 268. Geological Society of London Special Publications, pp. 91–146.

Beaumont, C., Jamieson, R.A., Butler, J.P., Warren, C.J., 2009. Crustal structure: a key constraint on the mechanism of ultra-high-pressure rock exhumation. Earth Planet. Sci. Lett. 287, 116–129.

Bell, T.H., 1981. Foliation development: the contribution, geometry and significance of progressive, bulk, inhomogeneous shortening. Tectonophysics 75, 273–296.

Bell, T.H., 2010. Deformation partitioning, foliation successions and their significance for orogenesis: hiding lengthy deformation histories in mylonites. In: In: Law, R.D., Butler, R.W.H., Holdsworth, R.E., Krabbendam, M., Strachan, R.A. (Eds.), Continental Tectonics and Mountain Building: the Legacy of Peach and Horne, vol 335. Geological Societyof London Special Publications, pp. 275–292.

Bell, T.H., Hickey, K.A., 1999. Complex microstructures preserved in rocks with a simple matrix: significance for deformation and metamorphic processes. J. Metamorph. Geol. 17, 521–536.

Bell, T.H., Hobbs, B.E., 2010. Foliations and shear sense: a modern approach to an old problem. J. Geol. Soc. India 75, 137–151.

Bell, T.H., Johnson, S.E., 1989. Porphyroblast inclusion trails: the key to orogenesis. J. Metamorph. Geol. 7, 279–310.

Bell, T.H., Johnson, S.E., 1992. Shear sense: a new approach that resolves conflicts between criteria in metamorphic rocks. J. Metamorph. Geol. 10, 99–124.

Bell, T.H., Newman, R., 2006. Appalachian orogenesis: the role of repeated gravitational collapse. Geol. Soc. Am. Spec. Pap. 414, 95–118.

Bell, T.H., Sapkota, J., 2012. Episodic gravitational collapse and migration of the mountain chain during orogenic roll-on in the Himalayas. J. Metamorph. Geol. 30, 651–666.

Bell, T.H., Rieuwers, M.T., Cihan, M., Evans, T.P., Ham, A.P., Welch, P.W., 2013. Inter-relationships between deformation partitioning, metamorphism and tectonism. Tectonophysics 587, 119–132.

Bernabe, Y., Brace, W.F., 1990. Deformation and fracture of Berea sandstone. In: In: Duba, A.G., Durham, W.B., Handin, J.W., Wang, H.F. (Eds.), The Brittle-Ductile Transition in Rocks, Geophys. Monogr, vol 56. Am. Geophys. Union, pp. 91–101.

Bésuelle, P., 2001. Evolution of strain localisation with stress in a sandstone: brittle and semi-brittle regimes. Phys. Chem. Earth Solid Earth Geodes. 26, 101–106.

Bezerra, F.H.R., Rossetti, D.F., Oliveira, R.G., Medeiros, W.E., Neves, B.B., Balsamo, F., Noguiera, F.C.C., Dantas, E.L., Andrades Filho, C., Góes, A.M., 2014. Neotectonic reactivation of shear zones and implications for faulting style and geometry in the continental margin of NE Brazil. Tectonophysics 614, 78–90.

Bigi, S., 2006. An example of inversion in a brittle shear zone. J. Struct. Geol. 28, 431–443.

Blasband, B., Brooijmans, P., Dirks, P., Visser, W., White, S., 1997. A Pan-African core complex in the Sinai, Egypt. Geol. Mijnb. 76, 247–266.

Blenkinsop, T.G., 2002. Deformation Microstructures and Mechanisms in Minerals and Rocks. Kluwer Academic Publishers, New York, 978-0-306-47543-6pp. 150.

Bond, R.M.G., McClay, K.R., 1995. Inversion of a Lower Cretaceous extensional basin, south central Pyrenees, Spain. In: In: Buchanan, J.G., Buchanan, P.G. (Eds.), Basin Inversion, vol 88. Geological Societyof London Special Publications, pp. 415–431.

Bose, N., Mukherjee, S., 2017. Map Interpretation for Structural Geologists. Elsevier, Amsterdam, 978-0-12-809681-9pp. 49.

Bose, N., Dutta, D., Mukherjee, S., 2018. Role of grain-size in phyllonitisation: insights from mineralogy, microstructures, strain analyses and numerical modeling. J. Struct. Geol. 112, 39–52.

Bouchez, J.-L., Lister, G., Nicolas, A., 1983. Fabric asymmetry and shear sense in movement zones. Geol. Rundsch. 72, 401–419.

Branney, M.J., Kokelaar, P., 1994. Volcanotectonic faulting, soft-state deformation, and rheomorphism of tuffs during development of a piecemeal caldera, English Lake District. Geol. Soc. Am. Bull. 106, 507–530.

Brueckner, H.K., Cuthbert, S.J., 2013. Extension, disruption, and translation of an orogenic wedge by exhumation of large ultrahigh-pressure terranes: examples from the Norwegian Caledonides. Lithosphere 5, 277–289.

Brun, J.P., Faccenna, C., 2008. Exhumation of high-pressure rocks driven by slab rollback. Earth Planet. Sci. Lett. 272, 1–7.

Burg, J.P., 1999. Ductile structures and instabilities: their implication for Variscan tectonics in the Ardennes. Tectonophysics 309, 1–25.

Butler, R.W., Tavarnelli, E., Grasso, M., 2006. Structural inheritance in mountain belts: an Alpine–Apennine perspective. J. Struct. Geol. 28, 1893–1908.

Caddick, M.J., 2004. Tectono-metamorphic Evolution of the Central and Western Himalaya. PhD. University of Cambridge.

Caddick, M.J., Bickle, M.J., Harris, N.B.W., Holland, T.J.B., Horstwood, M.S.A., Parrish, R.R., Ahmad, T., 2007. Burial and exhumation history of a Lesser Himalayan schist: recording the formation of an inverted metamorphic sequence in NW India. Earth Planet. Sci. Lett. 264, 375–390.

Cao, S., Neubauer, F., Bernroider, M., Genser, J., Liu, J., Friedl, G., 2017. Low-grade retrogression of a high-temperature metamorphic core complex: naxos, Cyclades, Greece. Geol. Soc. Am. Bull. 129, 93–117.

Carmignani, L., Decandia, F.A., Fantozzi, P.L., Lazzarotto, A., Liotta, D., Meccheri, M., 1994. Tertiary extensional tectonics in Tuscany (northern Apennines, Italy). Tectonophysics 238, 295–315.

Cashman, P.H., Ellis, M.A., 1994. Fault interaction may generate multiple slip vectors on a single fault surface. Geology 22, 1123–1126.

Cassel, E.J., Smith, M.E., Jicha, B.R., 2018. The impact of slab rollback on earth's surface: uplift and extension in the hinterland of the north American Cordillera. Geophys. Res. Lett. 45, 10–996.

Ceuleneer, G., Nicolas, A., Boudier, F., 1988. Mantle flow patterns at an oceanic spreading centre: the Oman peridotites record. Tectonophysics 151, 1–26.

Chakraborty, S., Mukul, M., 2019. New insights into the position and geometry of the Main Central Thrust from Sikkim, eastern Himalaya. J. Geol. 127, 289–322.

Chambers, J.A., Argles, T.W., Horstwood, M.S.A., Harris, N.B.W., Parrish, R.R., Ahmad, T., 2008. Tectonic implications of palaeoproterozoic anatexis and late Miocene metamorphism in the Lesser Himalayan Sequence, Sutlej valley, NW India. J. Geol. Soc. 165, 725–737.

Chattopadhyay, A., Khasdeo, L., Holdsworth, R.E., Smith, S.A.F., 2008. Fault reactivation and pseudotachylite generation in the semi-brittle and brittle regimes: examples from the Gavilgarh–Tan Shear Zone, central India. Geol. Mag. 145, 766–777.

Chen, Z., Schellart, W.P., Strak, V., Duarte, J.C., 2016. Does subduction-induced mantle flow drive backarc extension? Earth Planet. Sci. Lett. 441, 200–210.

Cladouhos, T.T., 1999. A kinematic model for deformation within brittle shear zones. J. Struct. Geol. 21, 437–448.

Constenius, K.N., 1996. Late Paleogene extensional collapse of the Cordilleran foreland fold and thrust belt. Geol. Soc. Am. Bull. 108, 20–39.

Cooke, M.L., Underwood, C.A., 2001. Fracture termination and step-over at bedding interfaces due to frictional slip and interface opening. J. Struct. Geol. 23, 223–238.

Cooper, M., Warren, M.J., 2010. The geometric characteristics, genesis and petroleum significance of inversion structures. In: In: Law, R.D., Butler, R.W.H., Holdsworth, R.E., Krabbendam, M., Strachan, R.A. (Eds.), Continental Tectonics and Mountain Building: the Legacy of Peach and Horne, vol 335. Geological Societyof London Special Publications, pp. 827–846.

Cooper, M.A., Williams, G.D., De Graciansky, P.C., Murphy, R.W., Needham, T., De Paor, D., Stoneley, R., Todd, S.P., Turner, J.P., Ziegler, P.A., 1989. Inversion tectonics - a

discussion. In: In: Cooper, M.A., Williams, G.D. (Eds.), Inversion Tectonics, vol 44. Geological Societyof London Special Publications, pp. 335–347.
Cooper, F.J., Platt, J.P., Platzman, E.S., Grove, M.J., Seward, G., 2010. Opposing shear senses in a subdetachment mylonite zone: implications for core complex mechanics. Tectonics 29. https://doi.org/10.1029/2009TC002632.
Corcoran, D.V., Doré, A.G., 2005. A review of techniques for the estimation of magnitude and timing of exhumation in offshore basins. Earth Sci. Rev. 72, 129–168.
Cosgrove, J.W., 2007. The use of shear zones and related structures as kinematic indicators: a review. In: In: Ries, A.C., Butler, R.W.H., Graham, R.H. (Eds.), Deformation of the Continental Crust: the Legacy of Mike Coward, vol 272. Geological Societyof London Special Publications, pp. 59–74.
Cowan, D.S., Botros, M., Johnson, H.P., 1986. Bookshelf tectonics: rotated crustal blocks within the sovanco fracture zone. Geophys. Res. Lett. 13, 995–998.
Cramer, B., Schlömer, S., Poelchau, H.S., 2002. Uplift-related hydrocarbon accumulations: the release of natural gas from groundwater. In: In: Dore, A.G., Cartwright, J.A., Stoker, M.S., Turner, J.P., White, N.J. (Eds.), Exhumation of the North Atlantic Margin: Timing, Mechanisms and Implications for Petroleum Exploration, vol 196. Geological Society of London Special Publications, pp. 447–457.
Crameri, F., Kaus, B.J., 2010. Parameters that control lithospheric-scale thermal localization on terrestrial planets. Geophys. Res. Lett. 37. https://doi.org/10.1029/2010GL042921.
Currenti, G., Bonaccorso, A., Del Negro, C., Scandura, D., Boschi, E., 2010. Elasto-plastic modeling of volcano ground deformation. Earth Planet. Sci. Lett. 296, 311–318.
Czertowicz, T.A., Toy, V.G., Scott, J.M., 2016. Recrystallisation, phase mixing and strain localisation in peridotite during rapid extrusion of sub-arc mantle lithosphere. J. Struct. Geol. 88, 1–19.
Dabrowski, M., Grasemann, B., 2019. Numerical modelling of boudinage under pure shear: implications for estimating viscosity ratios and finite strain from natural examples. J. Struct. Geol. 126, 109–128.
Dalmayrac, B., Molnar, P., 1981. Parallel thrust and normal faulting in Peru and constraints on the state of stress. Earth Planet. Sci. Lett. 55, 473–481.
Dasgupta, S., Mukherjee, S., 2017. Brittle shear tectonics in a narrow continental rift: asymmetric nonvolcanic barmer basin (Rajasthan, India). J. Geol. 125, 561–591.
Dasgupta, S., Mukherjee, S., 2019. Remote sensing in lineament identification: examples from western India. In: Billi, A., Fagereng, A. (Eds.), Problems and Solutions in Structural Geology and Tectonics. Developments in Structural Geology and Tectonics Book Series. 9780128140482, Series Editor: Mukherjee S.
Davis, G.H., Bump, A.P., García, P.E., Ahlgren, S.G., 2000. Conjugate Riedel deformation band shear zones. J. Struct. Geol. 22, 169–190.
De Paor, D.G., Eisenstadt, G., 1987. Stratigraphic and structural consequences of fault reversal: an example from the Franklinian Basin. Ellesmere Island. Geol. 15, 948–949.
Dijkstra, A.H., Drury, M.R., Frijhoff, R.M., 2002. Microstructures and lattice fabrics in the Hilti mantle section (Oman Ophiolite): evidence for shear localization and melt weakening in the crust–mantle transition zone? J. Geophys. Res. Solid Earth 107. https://doi.org/10.1029/2001JB000458.
Doblas, M., 1998. Slickenside kinematic indicators. Tectonophysics 295, 187–197.
Doblas, M., Faulkner, D., Mahecha, V., Aparicio, A., Hoyos, M., 1997a. Morphologically ductile criteria for the sense of movement on slickensides from an extensional detachment fault in southern Spain. J. Struct. Geol. 19, 1045–1054.
Doblas, M., Mahecha, V., Hoyos, M., 1997b. Slickenside and fault surface kinematic indicators on active normal faults of the Alpine Betic cordilleras, Granada, southern Spain. J. Struct. Geol. 19, 159–170.
Dobmeier, C., Simmat, R., 2002. Post-Grenvillean transpression in the Chilka Lake area, Eastern Ghats Belt—implications for the geological evolution of peninsular India. Precambrian Res. 113, 243–268.
Doré, A.G., Corcoran, D.V., Scotchman, I., 2002. Exhumation of North Atlantic Margins: timing, mechanisms and implications for hydrocarbon exploration. In: In: Doré, A.G., Cartwright, J.A., Stoker, M.S., Turner, J.P., White, N.J. (Eds.), Exhumation of the North Atlantic Margin: Timing, Mechanisms and Implications for Hydrocarbon Exploration, vol 196. Geological Society of London Special Publications, pp. 401–429.
Doré, A.G., Scotchman, I.C., Corcoran, D., 2000. Cenozoic exhumation and prediction of the hydrocarbon system on the NW European margin. J. Geochem. Explor. 69, 615–618.
Dresen, G., 1991. Stress distribution and the orientation of Riedel shears. Tectonophysics 188, 239–247.
Duda, M., Renner, J., 2013. The weakening effect of water on the brittle failure strength of sandstone. Geophys. J. Int. 192, 1091–1108.
Dutta, D., 2016. Opposite ductile shear senses (Tso Morari dome, Ladakh Himalaya, India). Int. J. Earth Sci. 106, 237.
Engelder, T., Schulmann, K., Lexa, O., 2004. Indentation pits: a product of incipient slip on joints with a mesotopography. In: In: Cosgrove, J.W., Engelder, T. (Eds.), The Initiation, Propagation and Arrest of Joints and Other Fractures, vol 231. Geological Society of London Special Publications, pp. 315–324.
Epard, J.L., Steck, A., 2008. Structural development of the Tso Morari ultra-high pressure nappe of the Ladakh Himalaya. Tectonophysics 451, 242–264.
Etchecopar, A., 1977. A plane kinematic model of progressive deformation in a polycrystalline aggregate. Tectonophysics 39, 121–139.
Exner, U., Mancktelow, N.S., Grasemann, B., 2004. Progressive development of s-type flanking folds in simple shear. J. Struct. Geol. 26, 2191–2201.
Fagereng, Å., Biggs, J., 2019. New perspectives on 'geological strain rates' calculated from both naturally deformed and actively deforming rocks. J. Struct. Geol. 125, 100–110.
Fenner, R.T., 2013. Finite Element Methods for Engineers, second ed. World Scientific Publishing, London, 978-1-84816-886-2pp. 245.
Flesch, L.M., Kreemer, C., 2010. Gravitational potential energy and regional stress and strain rate fields for continental plateaus: examples from the central Andes and Colorado Plateau. Tectonophysics 482, 182–192.
Fossen, H., 2016. Structural Geology, second ed. Cambridge University Press, Cambridge, 978-1107057647pp. 510.
Fossen, H., Cavalcante, G.C.G., 2017. Shear zones–A review. Earth Sci. Rev. 171, 434–455.
Freund, R., 1970. Rotation of strike slip faults in Sistan, southeast Iran. J. Geol. 78, 188–200.
Frisicale, M.C., Martinez, F.J., Dimieri, L.V., Dristas, J.A., 2005. Microstructural analysis and P–T conditions of the Azul megashear zone, Tandilia, Buenos Aires province, Argentina. J. South Am. Earth Sci. 19, 433–444.
Froitzheim, N., Conti, P.T., Van Daalen, M., 1997. Late Cretaceous, synorogenic, low-angle normal faulting along the Schlinig fault (Switzerland, Italy, Austria) and its significance for the tectonics of the Eastern Alps. Tectonophysics 280, 267–293.
Froitzheim, N., Pleuger, J., Nagel, T.J., 2006. Extraction faults. J. Struct. Geol. 28, 1388–1395.
Galadí-Enríquez, E., Zulauf, G., Heidelbach, F., Rohrmüller, J., 2006. Insights into the post-emplacement history of the Saunstein granitic dyke showing heterogeneous deformation and inconsistent shear-sense indicators (Bavarian Forest, Germany). J. Struct. Geol. 28, 1536–1552.
Gautam, P.K., Verma, A.K., Jha, M.K., Sarkar, K., Singh, T.N., Bajpai, R.K., 2016. Study of strain rate and thermal damage of Dholpur sandstone at elevated temperature. Rock Mech. Rock Eng. 49, 3805–3815.
Gawthorpe, R.L., Leeder, M.R., 2000. Tectono-sedimentary evolution of active extensional basins. Basin Res. 12, 195–218.
Gerya, T.V., Yuen, D.A., 2007. Robust characteristics method for modelling multiphase visco-elasto-plastic thermo-mechanical problems. Phys. Earth Planet. In. 163, 83–105.
Ghosh, S.K., 1993. Structural Geology: Fundamentals and Modern Developments. Pergamon Press, Oxford, 978-0080418780pp. 596.
Ghosh, S.K., Ramberg, H., 1976. Reorientation of inclusions by combination of pure shear and simple shear. Tectonophysics 34, 1–70.
Giambiagi, L., Alvarez, P., Spagnotto, S., 2016. Temporal variation of the stress field during the construction of the central Andes: constrains from the volcanic arc region (22–26° S), Western Cordillera, Chile, during the last 20 Ma. Tectonics 35, 2014–2033.
Giorgis, S., Tikoff, B., 2004. Constraints on kinematics and strain from feldspar porphyroclast populations. In: In: Alsop, G.I., Holdsworth, R.E., McCaffrey, K.J.W., Hand, M. (Eds.), Flow Processes in Faults and Shear Zones, vol 224. Geological Society of London Special Publications, pp. 265–285.
Godin, L., Grujic, D., Law, R.D., Searle, M.P., 2006. Channel flow, ductile extrusion and exhumation in continental collision zones: an introduction. In: In: Law, R.D., Searle, M.P., Godin, L. (Eds.), Channel Flow, Ductile Extrusion and Exhumation in Continental Collision Zone, vol 268. Geological Society of London Special Publications, pp. 1–23.
Goscombe, B.D., Passchier, C.W., 2003. Asymmetric boudins as shear sense indicators—an assessment from field data. J. Struct. Geol. 25, 575–589.
Goscombe, B., Trouw, R., 1999. The geometry of folded tectonic shear sense indicators. J. Struct. Geol. 21, 123–127.
Goscombe, B.D., Passchier, C.W., Hand, M., 2004. Boudinage classification: end-member boudin types and modified boudin structures. J. Struct. Geol. 26, 739–763.
Goswami, S., Mamtani, M.A., Rana, V., 2018. Quartz CPO and kinematic analysis in deformed rocks devoid of visible stretching lineations: an integrated AMS and EBSD investigation. J. Struct. Geol. 115, 270–283.
Grasemann, B., Dabrowski, M., 2015. Winged inclusions: pinch-and-swell objects during high-strain simple shear. J. Struct. Geol. 70, 78–94.
Grasemann, B., Stüwe, K., 2001. The development of flanking folds during simple shear and their use as kinematic indicators. J. Struct. Geol. 23, 715–724.
Grasemann, B., Fritz, H., Vannay, J.C., 1999. Quantitative kinematic flow analysis from the Main Central Thrust Zone (NW-Himalaya, India): implications for a decelerating strain path and the extrusion of orogenic wedges. J. Struct. Geol. 21, 837–853.
Grasemann, B., Stüwe, K., Vannay, J.C., 2003. Sense and non-sense of shear in flanking structures. J. Struct. Geol. 25, 19–34.
Grasemann, B., Schneider, D.A., Stöckli, D.F., Iglseder, C., 2012. Miocene bivergent crustal extension in the Aegean: evidence from the western Cyclades (Greece). Lithosphere 4, 23–39.
Grasemann, B., Dabrowski, M., Schöpfer, M.P., 2019. Sense and non-sense of shear reloaded. J. Struct. Geol. 125, 20–28.
Grogan, P., Østvedt-Ghazi, A.M., Larssen, G.B., Fotland, B., Nyberg, K., Dahlgren, S., Eidvin, T., 1999. Structural elements and petroleum geology of the Norwegian sector of the northern Barents Sea. In: In: Fleet, A.J., Boldy, S.A.R. (Eds.), Petroleum Geology of the Northwest Europe: Proceedings of the 5th Conference, vol 5. Geological Society of London, pp. 247–259.
Grujic, D., Hollister, L.S., Parrish, R.R., 2002. Himalayan metamorphic sequence as an orogenic channel: insight from Bhutan. Earth Planet. Sci. Lett. 198, 177–191.
Gudmundsson, A., 2011. Rock Fractures in Geological Processes. Cambridge University Press, Cambridge, 978-0521863926pp. 578.
Hacker, B.R., Gerya, T.V., 2013. Paradigms, new and old, for ultrahigh-pressure tectonism. Tectonophysics 603, 79–88.
Hancock, P.L., Barka, A.A., 1981. Opposed shear senses inferred from neotectonic mesofracture systems in the North Anatolian fault zone. J. Struct. Geol. 3, 383–392.
Hanmer, S., 1986. Asymmetrical pull-aparts and foliation fish as kinematic indicators. J. Struct. Geol. 8, 111–122.
Hanmer, S., Passchier, C.W., 1991. Shear-sense indicators: a review. Geol. Surv. Can. Pap. 90, 1–71.
Hansen, V.L., 1992. Backflow and margin-parallel shear within an ancient subduction complex. Geology 20, 71–74.

Hardman, M., Buchanan, J., Herrington, P., Carr, A., 1993. Geochemical modelling of the East Irish Sea Basin: its influence on predicting hydrocarbon type and quality. In: Parker, J.R. (Ed.), Petroleum Geology of Northwest Europe: Proceedings of the 4th Conference. Geological Society of London, pp. 809–821.
Harris, L.B., Koyi, H.A., Fossen, H., 2002. Mechanisms for folding of high-grade rocks in extensional tectonic settings. Earth Sci. Rev. 59, 163–210.
Hashiguchi, K., 2014. Elastoplasticity Theory, second ed. Springer, Berlin, 978-3-642-00273-1pp. 131–166.
Hatley, E., Carlson, W.D., Stuewe, K., Helper, M., 2009. Assessing the Kinematic Significance of the Plattengneis, a Major Intracrustal Transport Horizon in the Koralpe Region of the Eastern Alps. GSA Abstract.
Hayward, A.B., Graham, R.H., 1989. Some geometrical characteristics of inversion. In: In: Cooper, M.A., Williams, G.D. (Eds.), Inversion Tectonics, vol 44. Geological Societyof London Special Publications, pp. 17–39.
Heidbach, O., Rajabi, M., Cui, X., Fuchs, K., Müller, B., Reinecker, J., Reiter, K., Tingay, M., Wenzel, F., Xie, F., Ziegler, M.O., Zoback, M., 2018. The World Stress Map database release 2016: Crustal stress pattern across scales. Tectonophysics 744, 484–498.
Heinze, B., 2003. Active Intraplate Faulting in the Forearc of North Central Chile (30°–31° S): Implications from Neotectonic Field Studies, GPS Data, and Elastic Dislocation Modeling. GeoForschungsZentrum, Potsdam, Germany Scientific Technical Report 03/07.
Henderson, P., Henderson, G.M., 2009. The Cambridge Handbook of Earth Science Data. Cambridge University Press, Cambridge, 978-0521693172pp. 277.
Henriksen, E., Bjørnseth, H.M., Hals, T.K., Heide, T., Kiryukhina, T., Kløvjan, O.S., Larssen, G.B., Ryseth, A.E., Rønning, K., Sollid, K., Stoupakova, A., 2011. Uplift and erosion of the greater Barents Sea: impact on prospectivity and petroleum systems. In: Geological Society of London Memoirs Vol 35. pp. 271–281.
Herrin, E.A., 2008. Experimental Study of Shear and Compaction Band Formation in Berea Sandstone. Unpublished M.S. Thesis. Texas A & M University, pp. 51.
Hippertt, J.F.M., 1993. 'V'-pull-apart microstructures: a new shear-sense indicator. J. Struct. Geol. 15, 1393–1403.
Hippertt, J., Davis, B., 2000. Dome emplacement and formation of kilometre-scale synclines in a granite–greenstone terrain (Quadrilátero Ferrífero, southeastern Brazil). Precambr.Res. 102, 99–121.
Hippertt, J., Tohver, E., 1999. On the development of zones of reverse shearing in mylonitic rocks. J. Struct. Geol. 21, 1603–1614.
Hobbs, B.E., Ord, A., 2015. Structural Geology: The Mechanics of Deforming Metamorphic Rocks. Elsevier, Amsterdam, 978-0124078208pp. 665.
Hodges, K.V., 2000. Tectonics of the Himalaya and southern Tibet from two perspectives. Geol. Soc. Am. Bull. 112, 324–350.
Holcombe, R.J., Pearson, P.J., Oliver, N.H.S., 1991. Geometry of a Middle Proterozoic extensional decollement in northeastern Australia. Tectonophysics 191, 255–274.
Holdsworth, R.E., Butler, C.A., Roberts, A.M., 1997. The recognition of reactivation during continental deformation. J. Geol. Soc. 154, 73–78.
Holford, S.P., Tuitt, A.K., Hillis, R.R., Green, P.F., Stoker, M.S., Duddy, I.R., Sandiford, M., Tassone, D.R., 2014. Cenozoic deformation in the Otway Basin, southern Australian margin: implications for the origin and nature of post-breakup compression at rifted margins. Basin Res. 26, 10–37.
Holloway, S., Chadwick, R.A., 1986. The Sticklepath-Lustleigh fault zone: tertiary sinistral reactivation of a Variscan dextral strike-slip fault. J. Geol. Soc. 143, 447–452.
Holmes, A.J., Griffith, C.E., Scotchman, I.C., 1999. The Jurassic petroleum system of the West of Britain Atlantic margin–an integration of tectonics, geochemistry and basin modelling. In: In: Fleet, A.J., Boldy, S.A.R. (Eds.), Petroleum Geology of the Northwest Europe: Proceedings of the 5th Conference, vol 5. Geological Society of London, pp. 1351–1365.
Horton, B.K., 2018. Sedimentary record of Andean mountain building. Earth Sci. Rev. 178, 279–309.
Hsiao, L.Y., Graham, S.A., Tilander, N., 2004. Seismic reflection imaging of a major strike-slip fault zone in a rift system: Paleogene structure and evolution of the Tan-Lu fault system, Liaodong Bay, Bohai, offshore China. AAPG Bull. 88, 71–97.
Hudleston, P., 1999. Strain compatibility and shear zones: is there a problem? J. Struct. Geol. 21, 923–932.
Hueck, M., Basei, M.A.S., Wemmer, K., Oriolo, S., Heidelbach, F., Siegesmund, S., 2018a. Evolution of the major Gercino shear zone in the dom feliciano belt, south Brazil, and implications for the assembly of southwestern gondwana. Int. J. Earth Sci. https://doi.org/10.1007/s00531-018-1660-4.
Hueck, M., Oyhantçabal, P., Philipp, R.P., Basei, M.A.S., Siegesmund, S., 2018b. The dom feliciano belt in southern Brazil and Uruguay. In: Siegesmund, S., Oyhantçabal, P., Basei, M.A.S., Oriolo, S. (Eds.), Geology of Southwest Gondwana. Regional Geology Reviews. Springer, Heidelberg, pp. 267–302.
Husson, L., Ricard, Y., 2004. Stress balance above subduction: application to the Andes. Earth Planet. Sci. Lett. 222, 1037–1050.
Iacopini, D., Passchier, C.W., Koehn, D., Carosi, R., 2007. Fabric attractors in general triclinic flow systems and their application to high strain shear zones: a dynamical system approach. J. Struct. Geol. 29, 298–317.
Iaffa, D.N., Sàbat, F., Muñoz, J.A., Mon, R., Gutierrez, A.A., 2011. The role of inherited structures in a foreland basin evolution. The Metán Basin in NW Argentina. J. Struct. Geol. 33, 1816–1828.
Ishii, K., 1992. Partitioning of non-coaxiality in deforming layered rock masses. Tectonophysics 210, 33–43.
Ismail-Zadeh, A., Tackley, P., 2010. Computational Methods for Geodynamics. Cambridge University Press, Cambridge, 978-0521867672pp. 313.
Jaeger, J.C., Cook, N.G., Zimmerman, R., 2009. Fundamentals of Rock Mechanics, fourth ed. Blackwell Publishing, Malden, 978-8126534562pp. 475.
Jain, A.K., Kumar, D., Singh, S., Kumar, A., Lal, N., 2000. Timing, quantification and tectonic modelling of Pliocene–Quaternary movements in the NW Himalaya: evidence from fission track dating. Earth Planet. Sci. Lett. 179, 437–451.
Jamieson, R.A., Beaumont, C., 2013. On the origin of orogens. Geol. Soc. Am. Bull. 125, 1671–1702.
Japas, M.S., Re, G.H., Oriolo, S., Vilas, J.F., 2016. Basement-involved deformation overprinting thin-skinned deformation in the Pampean flat-slab segment of the southern Central Andes, Argentina. Geol. Mag. 153, 1042–1065.
Javadi, H.R., Ashtiani, M.E., Guest, B., Yassaghi, A., Ghassemi, M.R., Shahpasandzadeh, M., Naeimi, A., 2015. Tectonic reversal of the western doruneh fault system: implications for central asian tectonics. Tectonics 34, 2034–2051.
Jessup, M.J., Law, R.D., Searle, M.P., Hubbard, M.S., 2006. Structural evolution and vorticity of flow during extrusion and exhumation of the Greater Himalayan Slab, Mount Everest massif, Tibet/Nepal: implications for orogen-scale flow partitioning. In: In: Law, R.D., Searle, M.P., Godin, L. (Eds.), Channel Flow, Ductile Extrusion and Exhumation in Continental Collision Zone, vol 268. Geological Societyof London Special Publications, pp. 379–413.
Jiang, D., 1994. Flow variation in layered rocks subjected to bulk flow of various kinematic vorticities: theory and geological implications. J. Struct. Geol. 16, 1159–1172.
Johnson, S.E., Lenferink, H.J., Price, N.A., Marsh, J.H., Koons, P.O., West, D.P., Beane, R., 2009. Clast-based kinematic vorticity gauges: the effects of slip at matrix/clast interfaces. J. Struct. Geol. 31, 1322–1339.
Jolivet, L., Dubois, R., Fournier, M., Goffé, B., Michard, A., Jourdan, C., 1990. Ductile extension in alpine Corsica. Geology 18, 1007–1010.
Jolivet, L., Daniel, J.M., Fournier, M., 1991. Geometry and kinematics of extension in alpine corsica. Earth Planet. Sci. Lett. 104, 278–291.
Joshi, G., Agarwal, A., Agarwal, K.K., Srivastava, S., Valdivia, L.A., 2017. Microstructures and strain variation: evidence of multiple splays in the north almora thrust zone, kumaun lesser Himalaya, Uttarakhand, India. Tectonophysics 694, 239–248.
Katz, Y., Weinberger, R., Aydin, A., 2004. Geometry and kinematic evolution of riedel shear structures, capitol reef national Park, Utah. J. Struct. Geol. 26, 491–501.
Kearey, P., Klepeis, K.A., Vine, F.J., 2009. Global Tectonics. John Wiley & Sons, Oxford, 978-8126532957pp. 45–46.
Keep, M., Hansen, V.L., 1994. Deformational styles in the proterozoic pinal schist, pinal peak, Arizona: microstructural and quartz c-Axis Analyses. J. Geol. 102, 229–241.
Kellett, D.A., Cottle, J.M., Larson, K.P., 2019. The South Tibetan Detachment System: history, advances, definition and future directions. In: In: Treloar, P.J., Searle, M.P. (Eds.), Himalayan Tectonics: A Modern Synthesis, vol 483 Geological Societyof London Special Publications. https://doi.org/10.1144/SP483.2.
Khanal, S., Robinson, D.M., Kohn, M.J., Mandal, S., 2015. Evidence for a far-traveled thrust sheet in the Greater Himalayan thrust system, and an alternative model to building the Himalaya. Tectonics 34, 31–52.
Khazaradze, G., Klotz, J., 2003. Short-and long-term effects of GPS measured crustal deformation rates along the south central Andes. J. Geophys. Res. Solid Earth 108. https://doi.org/10.1029/2002JB001879.
Kilian, R., Heilbronner, R., Stünitz, H., 2011. Quartz microstructures and crystallographic preferred orientation: which shear sense do they indicate? J. Struct. Geol. 33, 1446–1466.
King, J., Harris, N., Argles, T., Parrish, R., Zhang, H., 2011. Contribution of crustal anatexis to the tectonic evolution of Indian crust beneath southern Tibet. Geol. Soc. Am. Bull. 123, 218–239.
Kirst, F., Leiss, B., 2017. Kinematics of syn-and post-exhumational shear zones at lago di Cignana (western Alps, Italy): constraints on the exhumation of zermatt–saas (ultra) high-pressure rocks and deformation along the combin fault and dent blanche basal thrust. Int. J. Earth Sci. 106, 215–236.
Kley, J., Monaldi, C.R., 2002. Tectonic inversion in the Santa Barbara System of the central Andean foreland thrust belt, northwestern Argentina. Tectonics 21. https://doi.org/10.1029/2002TC902003.
Klotz, J., Abolghasem, A., Khazaradze, G., Heinze, B., Vietor, T., Hackney, R., Bataille, K., Maturana, R., Viramonte, J., Perdomo, R., 2006. Long-term signals in the present-day deformation field of the Central and Southern Andes and constraints on the viscosity of the Earth's upper mantle. In: Oncken, O., Chong, G., Franz, G., Giese, P., Götze, H., Ramos, V.A., Strecker, M.R., Wigger, P. (Eds.), The Andes. Springer, Berlin, Heidelberg, 978-3-540-48684-8, pp. 65–89.
Kodaira, S., Fujie, G., Yamashita, M., Sato, T., Takahashi, T., Takahashi, N., 2014. Seismological evidence of mantle flow driving plate motions at a palaeo-spreading centre. Nat. Geosci. 7, 371–375.
Koehn, D., Passchier, C.W., 2000. Shear sense indicators in striped bedding-veins. J. Struct. Geol. 22, 1141–1151.
Kohn, M.J., 2008. PTt data from central Nepal support critical taper and repudiate large-scale channel flow of the Greater Himalayan Sequence. Geol. Soc. Am. Bull. 120, 259–273.
Kohn, M.J., 2014. Himalayan metamorphism and its tectonic implications. Annu. Rev. Earth Planet Sci. 42, 381–419.
Kossak-Glowczewski, J., Froitzheim, N., Nagel, T., Pleuger, J., Keppler, R., Leiss, B., Régent, V., 2017. Along-strike shear-sense reversal in the vals-scaradra shear zone at the front of the adula Nappe (central Alps, Switzerland). Swiss J. Geosci. 110, 677–697.
Koyi, H., Schmeling, H., Burchardt, S., Talbot, C., Mukherjee, S., Sjöström, H., Chemia, Z., 2013. Shear zones between rock units with no relative movement. J. Struct. Geol. 50, 82–90.
Krohe, A., 1990. Local variations in quartz [c]-axis orientations in non-coaxial regimes and their significance for the mechanics of S-C fabrics. J. Struct. Geol. 12, 995–1004.
Kruhl, J.H., 1996. Prism- and basal-plane parallel subgrain boundaries in quartz: A microstructural geothermobarometer. J. Metamorph. Geol. 14, 581–589.
Lacombe, O., Amrouch, K., Mouthereau, F., Dissez, L., 2007. Calcite twinning constraints on late Neogene stress patterns and deformation mechanisms in the active Zagros

collision belt. Geology 35, 263–266.
Langille, J., Lee, J., Hacker, B., Seward, G., 2010. Middle crustal ductile deformation patterns in southern Tibet: insights from vorticity studies in Mabja Dome. J. Struct. Geol. 32, 70–85.
Larson, K.P., 2018. Refining the structural framework of the Khimti Khola region, east-central Nepal Himalaya, using quartz textures and c-axis fabrics. J. Struct. Geol. 107, 142–152.
Larson, K.P., Cottle, J.M., 2014. Midcrustal discontinuities and the assembly of the Himalayan midcrust. Tectonics 33, 718–740.
Larson, K.P., Lamming, J.L., Faisal, S., 2014. Microscale strain partitioning? Differential quartz crystallographic fabric development in Phyllite, Hindu Kush, Northwestern Pakistan. Solid Earth 5, 1319.
Laure, D.K., Hudleston, P.J., 1987. Foliated breccias in the active Portuguese Bend landslide complex, California: bearing on melange genesis. J. Geol. 95, 407–422.
Laurich, B., Urai, J.L., Desbois, G., Vollmer, C., Nussbaum, C., 2014. Microstructural evolution of an incipient fault zone in Opalinus Clay: insights from an optical and electron microscopic study of ion-beam polished samples from the Main Fault in the Mt-Terri Underground Research Laboratory. J. Struct. Geol. 67, 107–128.
Law, R.D., Miller, E.L., Little, T.A., Lee, J., 1994. Extensional origin of ductile fabrics in the schist belt, central brooks range, Alaska—II.Microstructural and petrofabric evidence. J. Struct. Geol. 16, 919–940.
Law, R.D., Stahr Iii, D.W., Francsis, M.K., Ashley, K.T., Grasemann, B., Ahmad, T., 2013. Deformation temperatures and flow vorticities near the base of the Greater Himalayan series, Sutlej valley and Shimla klippe, NW India. J. Struct. Geol. 54, 21–53.
Lei, S.H., Park, R.G., 1993. Reversals of movement sense in Lewisian brittle–ductile shear zones at Gairloch, NW Scotland, in the context of Laxfordian kinematic history. Scot. J. Geol. 29, 9–19.
Leloup, P.H., Arnaud, N., Lacassin, R., Kienast, J.R., Harrison, T.M., Trong, T.P., Replumaz, A., Tapponnier, P., 2001. New constraints on the structure, thermochronology, and timing of the Ailao Shan-Red River shear zone, SE Asia. J. Geophys. Res. Solid Earth 106, 6683–6732. https://doi.org/10.1029/2000JB900322.
Lenze, A., Stöckhert, B., 2007. Microfabrics of UHP metamorphic granites in the Dora Maira Massif, western Alps–no evidence of deformation at great depth. J. Metamorph. Geol. 25, 461–475.
Lim, C., Cho, M., 2012. Two-phase contractional deformation of the jurassic daebo orogeny, Chungnam Basin, Korea, and its correlation with the early yanshanian movement of China. Tectonics 31. https://doi.org/10.1029/2011TC002909.
Lisle, R.J., 2013. Shear zone deformation determined from sigmoidal tension gashes. J. Struct. Geol. 50, 35–43.
Lister, G.S., Snoke, A.W., 1984. SC mylonites. J. Struct. Geol. 6, 617–638.
Lister, G.S., Williams, P.F., 1983. The partitioning of deformation in flowing rock masses. Tectonophysics 92, 1–33.
Little, T.A., Hacker, B.R., Brownlee, S.J., Seward, G., 2013. Microstructures and quartz lattice-preferred orientations in the eclogite-bearing migmatitic gneisses of the D'Entrecasteaux Islands, Papua New Guinea. Geochem. Geophys. 14, 2030–2062.
Liu, M., Shen, Y., Yang, Y., 2000. Gravitational collapse of orogenic crust: a preliminary three-dimensional finite element study. J. Geophys. Res. Solid Earth 105, 3159–3173. https://doi.org/10.1029/1999JB900289.
Lloyd, G.E., 2018. Syntectonic quartz vein evolution during progressive deformation. In: In: Bond, C.E., Lebit, H.D. (Eds.), Folding and Fracturing of Rocks: 50 Years of Research since the Seminal Text Book of J. G. Ramsay, vol 487 Geological Society, London Special Publications. https://doi.org/10.1144/SP487.3.
Lopez-Sanchez, M.A., Llana-Fúnez, S., 2018. A cavitation-seal mechanism for ultramylonite formation in quartzofeldspathic rocks within the semi-brittle field (Vivero fault, NW Spain). Tectonophysics 745, 132–153.
Louis, L., Wong, T.F., Baud, P., Tembe, S., 2006. Imaging strain localization by X-ray computed tomography: discrete compaction bands in Diemelstadt sandstone. J. Struct. Geol. 28, 762–775.
MacLeod, C.J., Murton, B.J., 1995. On the sense of slip of the Southern Troodos transform fault zone, Cyprus. Geology 23, 257–260.
Mancktelow, N.S., Pennacchioni, G., 2005. The control of precursor brittle fracture and fluid–rock interaction on the development of single and paired ductile shear zones. J. Struct. Geol. 27, 645–661.
Manickavasagam, R.M., Jain, A.K., Singh, S., Asokan, A., 1999. Metamorphic evolution of the northwest Himalaya, India: pressure-temperature data, inverted metamorphism, and exhumationin the Kashmir, Himachal, and Garhwal Himalayas. In: In: Macfarlane, A., Sorkhabi, R.B., Quade, J. (Eds.), Himalaya and Tibet: Mountain Roots to Mountain Tops: Geol., vol 328. Soc. Am. Sp. Pap., pp. 179–198.
Mao-Hong, Y., Guo-Wei, M., Hong-Fu, Q., Yong-Qiang, Z., 2006. Generalized Plasticity. Springer-Verlag Berlin Heidelberg, 978-3-540-30433-3pp. 122–153.
Marques, F.O., Nogueira, C.R., 2008. Normal fault inversion by orthogonal compression: sandbox experiments with weak faults. J. Struct. Geol. 30, 761–766.
Marques, F.O., Schmid, D.W., Andersen, T.B., 2007. Applications of inclusion behaviour models to a major shear zone system: the Nordfjord-Sogn Detachment Zone in western Norway. J. Struct. Geol. 29, 1622–1631.
Martin, A.J., 2017. A review of definitions of the Himalayan Main Central Thrust. Int. J. Earth Sci. 106, 2131–2145.
Maruyama, T., Lin, A., 2004. Slip sense inversion on active strike-slip faults in southwest Japan and its implications for Cenozoic tectonic evolution. Tectonophysics 383, 45–70.
Mattern, F., 2001. Permo-silesian movements between baltica and western Europe: tectonics and 'basin families' Terra. Nova 13, 368–375.
Mattern, F., Scharf, A., 2018. Postobductional extension along and within the frontal range of the eastern Oman mountains. J. Asian Earth Sci. 154, 369–385.
Małkowski, P., Ostrowski, Ł., Brodny, J., 2018. Analysis of Young's modulus for Carboniferous sedimentary rocks and its relationship with uniaxial compressive strength using different methods of modulus determination. J. Sust. Min. 17, 145–157.
Means, W.D., 1989. Stretching faults. Geology 17, 893–896.
Means, W.D., 1990. One-dimensional kinematics of stretching faults. J. Struct. Geol. 12, 267–272.
Means, W.D., Hobbs, B.E., Lister, G.S., Williams, P.F., 1980. Vorticity and non-coaxiality in progressive deformations. J. Struct. Geol. 2, 371–378.
Mercier, J.L., Sebrier, M., Lavenu, A., Cabrera, J., Bellier, O., Dumont, J.F., Machrare, J., 1992. Changes in the tectonic regime above a subduction zone of Andean type: The Andes of Peru and Bolivia during the Pliocene-Pleistocene. J. Geophys. Res. Solid Earth 97, 11945–11982. https://doi.org/10.1029/90JB02473.
Menegon, L., Pennacchioni, G., 2010. Local shear zone pattern and bulk deformation in the Gran Paradiso metagranite (NW Italian Alps). Int. J. Earth Sci. 99, 1805–1825.
Michels, Z.D., Kruckenberg, S.C., Davis, J.R., Tikoff, B., 2015. Determining vorticity axes from grain-scale dispersion of crystallographic orientations. Geology 43, 803–806.
Michibayashi, K., Gerbert-Gaillard, L., Nicolas, A., 2000. Shear sense inversion in the Hilti mantle section (Oman ophiolite) and active mantle uprise. Mar. Geophys. Res. 21, 259–268.
Miller, C., Klötzli, U., Frank, W., Thöni, M., Grasemann, B., 2000. Proterozoic crustal evolution in the NW Himalaya (India) as recorded by circa 1.80 Ga mafic and 1.84 Ga granitic magmatism. Precambrian Res. 103, 191–206.
Misra, A.A., Mukherjee, S., 2015. Tectonic Inheritance in Continental Rifts and Passive Margins. Springer, Berlin, 978-3-319-20576-2pp. 88.
Misra, A.A., Bhattacharya, G., Mukherjee, S., Bose, N., 2014. Near N–S paleo-extension in the western Deccan region, India: does it link strike-slip tectonics with India–Seychelles rifting? Int. J. Earth Sci. 103, 1645–1680.
Mortimer, N., Campbell, H.J., Tulloch, A.J., King, P.R., Stagpoole, V.M., Wood, R.A., Rattenbury, M.S., Sutherland, R., Adams, C.J., Collot, J., Seton, M., 2017. Zealandia: Earth's hidden continent. GSA Today (Geol. Soc. Am.) 27, 27–35.
Mortimer, N., Gans, P.B., Meffre, S., Martin, C.E., Seton, M., Williams, S., Turnbull, R.E., Quilty, P.G., Micklethwaite, S., Timm, C., Sutherland, R., Bache, F., Collot, J., Maurizot, P., Rouillard, P., Rollet, N., 2018. In: In: Sensarma, S., Storey, B.C. (Eds.), Large Igneous Provinces from Gondwana and Adjacent Regions. Regional Volcanism of Northern Zealandia: Post-gondwana Break-Up Magmatism on an Extended, Submerged Continent, vol 463. Geological Societyof London Special Publications, pp. 199–226.
Mpodozis, C., Allmendinger, R.W., 1993. Extensional tectonics, cretaceous Andes, northern Chile (27 S). Geol. Soc. Am. Bull. 105, 1462–1477.
Mukherjee, S., 2007. Geodynamics, Deformation and Mathematical Analysis of Metamorphic Belts of the NW Himalaya; Unpublished PhD Thesis. Indian Institute of Technology Roorkee, pp. 263pp.
Mukherjee, S., 2011. Mineral fish: their morphological classification, usefulness as shear sense indicators and genesis. Int. J. Earth Sci. 100, 1303–1314.
Mukherjee, S., 2012a. Tectonic implications and morphology of trapezoidal mica grains from the Sutlej section of the Higher Himalayan Shear Zone, Indian Himalaya. J. Geol. 120, 575–590.
Mukherjee, S., 2012b. Simple shear is not so simple! Kinematics and shear senses in Newtonian viscous simple shear zones. Geol. Mag. 149, 819–826.
Mukherjee, S., 2013a. Higher Himalaya in the Bhagirathi section (NW Himalaya, India): its structures, backthrusts and extrusion mechanism by both channel flow and critical taper mechanisms. Int. J. Earth Sci. 102, 1851–1870.
Mukherjee, S., 2013b. Deformation Microstructures in Rocks. Springer Science & Business Media, 978-3-642-25608-0pp. 116.
Mukherjee, S., 2014a. Review of flanking structures in meso- and micro-scales. Geol. Mag. 151, 957–974.
Mukherjee, S., 2014b. Atlas of Shear Zone Structures in Meso-Scale. Springer, Berlin, 978-3-319-00089-3pp. 124 Heidelberg.
Mukherjee, S., 2015a. Atlas of Structural Geology. Elsevier, Amsterdam, 9780124201521pp. 57.
Mukherjee, S., 2015b. A review on out-of-sequence deformation in the Himalaya. In: In: Mukherjee, S., Carosi, R., van der Beek, P.A., Mukherjee, B.K., Robinson, D.M. (Eds.), Tectonics of the Himalaya, vol 412. Geological Society of London Special Publications, pp. 1–13.
Mukherjee, S., 2017. Review on symmetric structures in ductile shear zones. Int. J. Earth Sci. 106, 1453–1468.
Mukherjee, S., 2019. Kinematics of pure shear ductile deformation within rigid walls: new analyses. In: Billi, A., Fagereng, A. (Eds.), Problems and Solutions in Structural Geology and Tectonics. Series Editor: Mukherjee S, Developments in Structural Geology and Tectonics Book Series. Elsevier9780128140482, .
Mukherjee, S., Khonsari, M.M., 2018. Inter-book normal fault-related shear heating in brittle bookshelf faults. Mar. Pet. Geol. 97, 45–48.
Mukherjee, S., Koyi, H.A., 2010a. Higher Himalayan Shear Zone, Zanskar section- microstructural studies & extrusion mechanism by a combination of simple shear & channel flow. Int. J. Earth Sci. 99, 1083–1110.
Mukherjee, S., Koyi, H.A., 2010b. Higher Himalayan Shear Zone, Sutlej section- structural geology & extrusion mechanism by various combinations of simple shear, pure shear & channel flow in shifting modes. Int. J. Earth Sci. 99, 1267–1303.
Mukherjee, S., Mulchrone, K.F., 2012. Estimating the viscosity and Prandtl number of the Tso Morari crystalline gneiss dome, Indian western Himalaya. Int. J. Earth Sci. 101, 1929–1947.
Mukherjee, S., Pal, P., 2000. Tectonic structures of the Karakoram metamorphic belt, its significance in the geodynamic evolution. Unpublished Report. In: Summer Undergraduate Research Award. University of Roorkee.
Mukherjee, S., Punekar, J., Mahadani, T., Mukherjee, R., 2015. A review on intrafolial folds and their morphologies from the detachments of the western Indian Higher

Himalaya. In: Mukherjee, S., Mulchrone, K.F. (Eds.), Ductile Shear Zones: from Micro- to Macro-Scales. Wiley Blackwell, 978-1-118-84496-0, pp. 182–205.
Mulch, A., Cosca, M.A., 2004. Recrystallization or cooling ages: in situ UV-laser 40Ar/39Ar geochronology of muscovite in mylonitic rocks. J. Geol. Soc. 161, 573–582.
Mulchrone, K.F., Mukherjee, S., 2015. Shear senses and viscous dissipation of layered ductile simple shear zones. Pure Appl. Geophys. 172, 2635–2642.
Mulchrone, K.F., Mukherjee, S., 2016. Kinematics and shear heat pattern of ductile simple shear zones with 'slip boundary condition' Int. J. Earth Sci. 105, 1015–1020.
Mulchrone, K.F., Mukherjee, S., 2019. Kinematics of ductile shear zones with deformable or mobile walls. J. Earth Sys. Sci (in press).
Navabpour, P., Barrier, E., 2012. Stress states in the Zagros fold-and-thrust belt from passive margin to collisional tectonic setting. Tectonophysics 581, 76–83.
Navabpour, P., Angelier, J., Barrier, E., 2007. Cenozoic post-collisional brittle tectonic history and stress reorientation in the High Zagros Belt (Iran, Fars Province). Tectonophysics 432, 101–131.
Navabpour, P., Angelier, J., Barrier, E., 2008. Stress state reconstruction of oblique collision and evolution of deformation partitioning in W-Zagros (Iran, Kermanshah). Geophys. J. Int. 175, 755–782.
Navabpour, P., Barrier, E., McQuillan, H., 2014. Oblique oceanic opening and passive margin irregularity, as inherited in the Zagros fold-and-thrust belt. Terra. Nova 26, 208–215.
Nemčok, M., 2016. Rifts and Passive Margins: Structural Architecture, Thermal Regimes, and Petroleum Systems. Cambridge University Press, New York, 978-1107025837pp. 607.
Nemčok, M., Gayer, R., Miliorizos, M., 1995. Structural analysis of the inverted Bristol Channel Basin: implications for the geometry and timing of fracture porosity. In: In: Buchanan, J.G.,, Buchanan, P.G. (Eds.), Basin Inversion, vol 88. Geological Society of London Special Publications, pp. 355–392.
Neves, S.P., Santos, T.A., Medeiros, P.C., Amorim, L.Q., Casimiro, D.C., 2018. Interference fold patterns in regional unidirectional stress fields: a result of local kinematic interactions. J. Struct. Geol. 115, 304–310.
Ngako, V., Affaton, P., Nnange, J.M., Njanko, T., 2003. Pan-African tectonic evolution in central and southern Cameroon: transpression and transtension during sinistral shear movements. J. Afr. Earth Sci. 36, 207–214.
Nicolas, A., Boudier, F., 2008. Large shear zones with no relative displacement. Terra. Nova 20, 200–205.
Nortje, G.S., Oliver, N.H.S., Blenkinsop, T.G., Keys, D.L., McLellan, J.G., Oxenburgh, S., 2011. New faults v. fault reactivation: implications for fault cohesion, fluid flow and copper mineralization, Mount Gordon Fault Zone, Mount Isa District, Australia. In: In: Fagereng, Å., Toy, V.G., Rowland, J.V. (Eds.), Geology of the Earthquake Source: A Volume in Honour of Rick Sibson, vol 359. Geological Societyof London Special Publications, pp. 287–311.
Olson, J.E., Pollard, D.D., 1991. The initiation and growth of en echelon veins. J. Struct. Geol. 13, 595–608.
Ord, A., 1991. Deformation of rock: a pressure-sensitive, dilatant material. Pure Appl. Geophys. 137, 337–366.
Ord, A., Vardoulakis, I., Kajewski, R., 1991. Shear band formation in Gosford sandstone. Int. J. Rock Mech. Min. Sci. Geomech. Abstr. 28, 397–409.
Oriolo, S., Wemmer, K., Oyhantçabal, P., Fossen, H., Schulz, B., Siegesmund, S., 2018. Geochronology of shear zones–A review. Earth Sci. Rev. 185, 665–683.
Pamplona, J., Rodrigues, B.C., Llana-Fúnez, S., Simões, P.P., Ferreira, N., Coke, C., Rodrigues, J., 2015. Structure and variscan evolution of malpica–lamego ductile shear zone (NW of iberian peninsula). In: Mukherjee, S.M., Mulchrone, K.F. (Eds.), Ductile Shear Zones: from Micro-to Macro-Scales. 978-1-118-84496-0, pp. 206–223.
Parsons, A.J., Coleman, M.J., Ryan, J.J., Zagorevski, A., Joyce, N.L., Gibson, H.D., Larson, K.P., 2018. Structural evolution of a crustal-scale shear zone through a decreasing temperature regime: the Yukon River shear zone, Yukon-Tanana terrane, Northern Cordillera. Lithosphere 10, 760–782.
Passchier, C.W., 1982. Mylonitic deformation in the Saint-Bathélem massif, French Pyrenees, with emphasis on the genetic relationship between ultramylonite and pseudotachylyte. In: GUA Papers of Geology, Series Vol 1. pp. 173pp.
Passchier, C.W., 1983. The reliability of asymmetric c-axis fabrics of quartz to determine sense of vorticity. Tectonophysics 99, T9–T18.
Passchier, C.W., 1984. The generation of ductile and brittle shear bands in a low-angle mylonite zone. J. Struct. Geol. 6, 273–281.
Passchier, C.W., 1998. Monoclinic model shear zones. J. Struct. Geol. 20, 1121–1137.
Passchier, C.W., 2001. Flanking structures. J. Struct. Geol. 23, 951–962.
Passchier, C., Coelho, S., 2006. An outline of shear-sense analysis in high-grade rocks. Gondwana Res. 10, 66–76.
Passchier, C.W., Platt, J.P., 2017. Shear zone junctions: of zippers and freeways. J. Struct. Geol. 95, 188–202.
Passchier, C.W., Simpson, C., 1986. Porphyroclast systems as kinematic indicators. J. Struct. Geol. 8, 831–843.
Passchier, C.W., Speck, P.J., 1994. The kinematic interpretation of obliquely-transected porphyroblasts: an example from the Trois Seigneurs Massif, France. J. Struct. Geol. 16, 971–984.
Passchier, C.W., Trouw, R.A.J., 2005. Microtectonics, second ed. Springer Heidelberg, 978-3-540-29359-0pp. 366.
Passchier, C.W., Williams, P.R., 1996. Conflicting shear sense indicators in shear zones; the problem of non-ideal sections. J. Struct. Geol. 18, 1281–1284.
Passchier, C.W., Myers, J.S., Kröner, A., 1990. Field Geology of High-Grade Gneiss Terrains. Springer - Verlag, 978-3-642-76013-6pp. 150.
Paterson, M.S., Wong, T.F., 2005. Experimental Rock Deformation-The Brittle Field. Springer, New York, 978-3-540-26339-5pp. 347.
Peacock, D.C.P., Sanderson, D.J., 2018. Structural analyses and fracture network characterisation: seven pillars of wisdom. Earth Sci. Rev. 184, 13–28.
Pei, Y., Paton, D.A., Knipe, R.J., Wu, K., 2015. A review of fault sealing behaviour and its evaluation in siliciclastic rocks. Earth Sci. Rev. 150, 121–138.
Pennacchioni, G., 2005. Control of the geometry of precursor brittle structures on the type of ductile shear zone in the Adamello tonalites, Southern Alps (Italy). J. Struct. Geol. 27, 627–644.
Pennacchioni, G., Mancktelow, N.S., 2018. Small-scale ductile shear zones: neither extending, nor thickening, nor narrowing. Earth Sci. Rev. 184, 1–12.
Pennacchioni, G., Zucchi, E., 2013. High temperature fracturing and ductile deformation during cooling of a pluton: the Lake Edison granodiorite (Sierra Nevada batholith, California). J. Struct. Geol. 50, 54–81.
Peresson, H., Decker, K., 1997. Far-field effects of late Miocene subduction in the eastern carpathians: E-W compression and inversion of structures in the alpine--carpathian-pannonian region. Tectonics 16, 38–56.
Perez, N.D., Horton, B.K., McQuarrie, N., Stuebner, K., Ehlers, T.A., 2016. Andean shortening, inversion and exhumation associated with thin-and thick-skinned deformation in southern Peru. Geol. Mag. 153, 1013–1041.
Petit, J.P., 1987. Criteria for the sense of movement on fault surfaces in brittle rocks. J. Struct. Geol. 9, 597–608.
Phillipson, S.E., 2003. The control of coal bed decollement-related slickensides on roof falls in North American Late Paleozoic coal basins. Int. J. Coal Geol. 53, 181–195.
Piazolo, S., Bons, P.D., Griera, A., Llorens, M.G., Gomez-Rivas, E., Koehn, D., Wheeler, J., Gardner, R., Godinho, J.R.A., Lebensohn, R.A., 2019. A review of numerical modelling of the dynamics of microstructural development in rocks and ice: Past, present and future. J. Struct. Geol. 125, 111–123.
Pieri, M., Burlini, L., Kunze, K., Stretton, I., Olgaard, D.L., 2001. Rheological and microstructural evolution of Carrara marble with high shear strain: results from high temperature torsion experiments. J. Struct. Geol. 23, 1393–1413.
Pinheiro, R.V., Holdsworth, R.E., 1997. Reactivation of Archaean strike-slip fault systems, Amazon region, Brazil. J. Geol. Soc. 154, 99–103.
Pirouz, M., Simpson, G., Bahroudi, A., Azhdari, A., 2011. Neogene sediments and modern depositional environments of the Zagros foreland basin system. Geol. Mag. 148, 838–853.
Platt, J.P., Passchier, C.W., 2016. Zipper junctions: a new approach to the intersections of conjugate strike-slip faults. Geology 44, 795–798.
Poliakov, A.N.B., Herrmann, H.J., 1994. Self-organized criticality of plastic shear bands in rocks. Geophys. Res. Lett. 21, 2143–2146.
Popov, A.A., Sobolev, S.V., 2008. SLIM3D: a tool for three-dimensional thermomechanical modeling of lithospheric deformation with elasto-visco-plastic rheology. Phys. Earth Planet. In. 171, 55–75.
Puelles, P., Abalos, B., Gil Ibarguchi, J.I., Rodríguez, J., 2018. Scales of deformation partitioning during exhumation in a continental subduction channel: a petrofabric study of eclogites and gneisses from NW Spain (Malpica-Tui Allochthonous Complex). J. Metamorph. Geol. 36, 225–254.
Rajabi, M., Sherkati, S., Bohloli, B., Tingay, M., 2010. Subsurface fracture analysis and determination of in-situ stress direction using FMI logs: an example from the Santonian carbonates (Ilam Formation) in the Abadan Plain, Iran. Tectonophysics 492, 192–200.
Rajesh, K.G., Chetty, T.R.K., 2006. Structure and tectonics of the achankovil shear zone, southern India. Gondwana Res. 10, 86–98.
Rajlich, P., 1993. Riedel shear: a mechanism for crenulation cleavage. Earth Sci. Rev. 34, 167–195.
Ramos, V.A., 2010. The tectonic regime along the Andes: present-day and Mesozoic regimes. Geol. J. 45, 2–25.
Ramsay, J.G., Huber, M.I., 1987. The Techniques of Modern Structural Geology, vol. 2. Academic Press, London, 978-0125769228pp. 529–530.
Ramsay, J.G., Lisle, R.J., 2000. The techniques of modern structural geology. In: Continuum Mechanics in Structural Geology, vol. 3. Academic Press, London, 978-0125769235, pp. 701–1061.
Rapa, G., Groppo, C., Mosca, P., Rolfo, F., 2016. Petrological constraints on the tectonic setting of the Kathmandu Nappe in the langtang–gosainkund–helambu regions, Central Nepal Himalaya. J. Metamorph. Geol. 34, 999–1023.
Redmond, J.L., 1972. Null combination in fault interpretation. AAPG (Am. Assoc. Pet. Geol.) Bull. 56, 150–158.
Regenauer-Lieb, K., Yuen, D.A., 2003. Modeling shear zones in geological and planetary sciences: solid- and fluid-thermal–mechanical approaches. Earth Sci. Rev. 63, 295–349.
Rekha, S., Bhattacharya, A., Chatterjee, N., 2014. Tectonic restoration of the Precambrian crystalline rocks along the west coast of India: correlation with eastern Madagascar in East Gondwana. Precambrian Res. 252, 191–208.
Rey, P.F., Müller, R.D., 2010. Fragmentation of active continental plate margins owing to the buoyancy of the mantle wedge. Nat. Geosci. 3, 257.
Rey, P., Vanderhaeghe, O., Teyssier, C., 2001. Gravitational collapse of the continental crust: definition, regimes and modes. Tectonophysics 342, 435–449.
Richards, A.P., 2004. Isotopic Mapping of Major Tectonic Structures, Dissertation. The Open University.
Richards, A., Argles, T., Harris, N., Parrish, R., Ahmad, T., Darbyshire, F., Draganits, E., 2005. Himalayan architecture constrained by isotopic tracers from clastic sediments. Earth Planet. Sci. Lett. 236, 773–796.
Robin, P.Y.F., Cruden, A.R., 1994. Strain and vorticity patterns in ideally ductile transpression zones. J. Struct. Geol. 16, 447–466.
Robinson, D.M., DeCelles, P.G., Garzione, C.N., Pearson, O.N., Harrison, T.M., Catlos, E.J., 2003. Kinematic model for the main central thrust in Nepal. Geology 31, 359–362.
Romeo, I., Capote, R., Lunar, R., Cayzer, N., 2007. Polymineralic orientation analysis of magmatic rocks using Electron Back-Scatter Diffraction: implications for igneous fabric origin and evolution. Tectonophysics 444, 45–62.

Rosenberg, C.L., Kissling, E., 2013. 3D insight into Alpine collision: lower plate or upper plate indentation. Geology 41, 1219–1222.
Roy, P., Jain, A.K., Singh, S., 2010. Microstructures of mylonites along the Karakoram shear zone, tangste valley, pangong mountains, Karakoram. J. Geol. Soc. India 75, 679–694.
Ruh, J.B., Vergés, J., 2018. Effects of reactivated extensional basement faults on structural evolution of fold-and-thrust belts: insights from numerical modelling applied to the Kopet Dagh Mountains. Tectonophysics 746, 493–511.
Ruiz-Fuentes, A., Aerden, D.G.A.M., 2018. Transposition of foliations and superposition of lineations during polyphase deformation in the Nevado-Filabride complex: tectonic implications. Int. J. Earth Sci. 107, 1975–1988.
Sagripanti, L., Vera, E.A.R., Gianni, G.M., Folguera, A., Harvey, J.E., Farías, M., Ramos, V.A., 2015. Neotectonic reactivation of the western section of the Malargüe fold and thrust belt (Tromen volcanic plateau, Southern Central Andes). Geomorphology 232, 164–181.
Samant, H., Pundalik, A., D'souza, J., Sheth, H., Lobo, K.C., D'souza, K., Patel, V., 2017. Geology of the Elephanta Island fault zone, western Indian rifted margin, and its significance for understanding the Panvel flexure. J. Earth Sys. Sci. 126, 9.
Samanta, S.K., Mandal, N., Chakraborty, C., 2002. Development of different types of pull-apart microstructures in mylonites: an experimental investigation. J. Struct. Geol. 24, 1345–1355.
Sander, B., 1911. Über Zusammenhänge zwischen Teilbewegung und Gefüge in Gesteinen. Mineral. Petrogr. Mittl. 30, 281–314.
Sarkarinejad, K., Azizi, A., 2008. Slip partitioning and inclined dextral transpression along the Zagros Thrust System, Iran. J. Struct. Geol. 30, 116–136.
Sarkarinejad, K., Pash, R.R., Motamedi, H., Yazdani, M., 2018. Deformation and kinematic evolution of the subsurface structures: Zagros foreland fold-and-thrust belt, northern Dezful Embayment, Iran. Int. J. Earth Sci. 107, 1287–1304.
Sawaguchi, T., 2004. Deformation history and exhumation process of the horoman peridotite complex, hokkaido, Japan. Tectonophysics 379, 109–126.
Scharf, A., Mattern, F., Pracejus, B., 2019. Two new microscopic ductile kinematic indicators from the Oman Mountains. J. Struct. Geol. 119, 107–117.
Schlichting, H., Gersten, K., 2017. Boundary–Layer Theory, ninth ed. Springer, Berlin, Heidelberg, pp. 814.
Schlunegger, F., Kissling, E., 2015. Slab rollback orogeny in the Alps and evolution of the Swiss Molasse basin. Nat. Commun. 6, 8605.
Schmid, D.W., Podladchikov, Y.Y., 2005. Mantled porphyroclast gauges. J. Struct. Geol. 27, 571–585.
Schmidt, C.J., Astini, R.A., Costa, C.H., Gardini, C.E., Kraemer, P.E., 1995. Cretaceous rifting, alluvial fan sedimentation, and Neogene inversion, southern Sierras Pampeanas, Argentina. In: In: Tankard, A.J., Suarez, R., Welsink, H.J. (Eds.), Petroleum Basins of South America: Am. Assoc. Petrol. Geol. Mem, vol 62. pp. 341–358.
Schulte, D.O., Ring, U., Thomson, S.N., Glodny, J., Carrad, H., 2014. Two-stage development of the paparoa metamorphic core complex, west coast, south island, New Zealand: hot continental extension precedes sea-floor spreading by ~ 25 my. Lithosphere 6, 177–194.
Schultz, R.A., Okubo, C.H., Fossen, H., 2010. Porosity and grain size controls on compaction band formation in Jurassic Navajo Sandstone. Geophys. Res. Lett. 37. https://doi.org/10.1029/2010GL044909.
Scisciani, V., Tavarnelli, E., Calamita, F., 2002. The interaction of extensional and contractional deformations in the outer zones of the Central Apennines, Italy. J. Struct. Geol. 24, 1647–1658.
Searle, M.P., Alsop, G.I., 2007. Eye-to-eye with a mega–sheath fold: a case study from Wadi Mayh, northern Oman Mountains. Geology 35, 1043–1046.
Searle, M.P., Cottle, J.M., Streule, M.J., Waters, D.J., 2010. Crustal melt granitoids and migmatites along the Himalaya: melt source, segregation, transport and granite emplacement mechanisms. Trans. Roy. Soc. Edinb. 100, 219–233.
Sébrier, M., Mercier, J.L., Mégard, F., Laubacher, G., Carey-Gailhardis, E., 1985. Quaternary normal and reverse faulting and the state of stress in the central Andes of south Peru. Tectonics 4, 739–780.
Sébrier, M., Lavenu, A., Fornari, M., Soulas, J.P., 1988. Tectonics and uplift in central Andes (Peru, Bolivia and northern Chile) from eocene to present. Geodynamique 3, 85–106.
Sen, K., Das, S., Mukherjee, B.K., Sen, K., 2013. Bimodal stable isotope signatures of Zildat Ophiolitic Mélange, Indus Suture Zone, Himalaya: implications for emplacement of an ophiolitic mélange in a convergent setup. Int. J. Earth Sci. 102, 2033–2042.
Sengupta, S., Chatterjee, S.M., 2015. Microstructural variations in quartzofeldspathic mylonites and the problem of vorticity analysis using rotating porphyroclasts in the Phulad Shear Zone, Rajasthan, India. In: Mukherjee, S.M., Mulchrone, K.F. (Eds.), Ductile Shear Zones: from Micro-to Macro-Scales. 978-1-118-84496-0, pp. 128–140.
Seranne, M., 1992. Late palaeozoic kinematics of the møre-trøndelag fault zone and adjacent areas, central Norway. Nor. Geol. Tidsskr. 72, 141–158.
Shelley, D., 1995. Asymmetric shape preferred orientations as shear-sense indicators. J. Struct. Geol. 17, 509–517.
Shipton, Z.K., Cowie, P.A., 2003. A conceptual model for the origin of fault damage zone structures in high-porosity sandstone. J. Struct. Geol. 25, 333–344.
Sibson, R.H., 1985. A note on fault reactivation. J. Struct. Geol. 7, 751–754.
Sibson, R.H., 2001. Seismogenic framework for hydrothermal transport and ore deposition. In: In: Richards, J.,P., Tosdal, R.M. (Eds.), Structural Controls on Ore Genesis, vol 14. Rev. Econ. Geol. Soc. Econ. Geol. Littleton, CO, pp. 25–47.
Sigmundsson, F., Einarsson, P., Bilham, R., Sturkell, E., 1995. Rift-transform kinematics in south Iceland: deformation from global positioning system measurements, 1986 to 1992. J. Geophys. Res. Solid Earth 100, 6235–6248.
Simpson, C., De Paor, D.G., 1993. Strain and kinematic analysis in general shear zones. J. Struct. Geol. 15, 1–20.
Singh, S., Jain, A.K., 1993. Deformational and strain patterns of the Jutogh Nappe along the Sutlej valley in jeori-wangtu region. J. Himal. Geol. 4, 41–55.
Smith, S.A.F., Tesei, T., Scott, J.M., Collettini, C., 2017. Reactivation of normal faults as high-angle reverse faults due to low frictional strength: experimental data from the Moonlight Fault Zone, New Zealand. J. Struct. Geol. 105, 34–43.
Soliva, R., Schultz, R.A., Ballas, G., Taboada, A., Wibberley, C., Saillet, E., Benedicto, A., 2013. A model of strain localization in porous sandstone as a function of tectonic setting, burial and material properties; new insight from Provence (southern France). J. Struct. Geol. 49, 50–63.
Sousa, J., 2008. Kinematic analysis of mylonitic rocks, southern ruby mountains, SW Montana: evidence for proterozoic orogenic crustal thickening and topographic collapse. Undergrad. Rev. 4, 57–63.
Spanos, D., Xypolias, P., Koukouvelas, I., 2015. Vorticity analysis in calcite tectonites: an example from the Attico-Cycladic massif (Attica, Greece). J. Struct. Geol. 80, 120–132.
Sternai, P., Jolivet, L., Menant, A., Gerya, T., 2014. Driving the upper plate surface deformation by slab rollback and mantle flow. Earth Planet. Sci. Lett. 405, 110–118.
Stewart, S.A., Argent, J.D., 2000. Relationship between polarity of extensional fault arrays and presence of detachments. J. Struct. Geol. 22, 693–711.
Stipp, M., Stünitz, H., Heilbronner, R., Schmid, S.M., 2002a. The eastern Tonale fault zone: a 'natural laboratory'for crystal plastic deformation of quartz over a temperature range from 250 to 700 C. J. Struct. Geol. 24, 1861–1884.
Stipp, M., Stünitz, H., Heilbronner, R., Schmid, S.M., 2002b. Dynamic recrystallization of quartz: correlation between natural and experimental conditions. In: In: De Meer, S., Drury, M.R., De Bresser, J.H.P., Pencock, G.M. (Eds.), Deformation Mechanisms, Rheology and Tectonics: Current Status and Future Perspectives, vol 200. Geological Society, London, pp. 171–190 Special Publications.
Stöckhert, B., Duyster, J., 1999. Discontinuous grain growth in recrystallised vein quartz—implications for grain boundary structure, grain boundary mobility, crystallographic preferred orientation, and stress history. J. Struct. Geol. 21, 1477–1490.
Sulem, J., Vardoulakis, I., Papamichos, E., Oulahna, A., Tronvoll, J., 1999. Elasto-plastic modelling of red wildmoor sandstone. Mechanics of cohesive-frictional materials. An Int. J. Exp. Mod. Comp. Mat. Struct. 4, 215–245.
Sümer, Ö., 2015. Evidence for the reactivation of a pre-existing zone of weakness and its contributions to the evolution of the Küçük Menderes Graben: a study on the Ephesus Fault, Western Anatolia, Turkey. Geodin. Acta 27, 130–154.
Szeliga, W.M., 2010. Historical and Modern Seismotectonics of the Indian Plate with an Emphasis on its Western Boundary with the Eurasian Plate. Ph.D. Thesis. University of Colorado at Boulder.
Tadmor, E.B., Miller, R.E., Elliott, R.S., 2012. Continuum Mechanics and Thermodynamics: from Fundamental Concepts to Governing Equations. Cambridge University Press, Cambridge, 978-1107008267pp. 350.
Tanaka, H., 1992. Cataclastic lineations. J. Struct. Geol. 14, 1239–1252.
Tapponnier, P., Peltzer, G.L.D.A.Y., Le Dain, A.Y., Armijo, R., Cobbold, P., 1982. Propagating extrusion tectonics in Asia: New insights from simple experiments with plasticine. Geology 10, 611–616.
Tavani, S., Corradetti, A., Sabbatino, M., Morsalnejad, D., Mazzoli, S., 2018. The Mesozoic-Cenozoic fracture pattern of the Lurestan region, Iran: the role of rifting, convergence, and differential compaction in the development of pre-orogenic oblique fractures in the Zagros Belt. Tectonophysics 749, 104–119.
Tavarnelli, E., 1999. Normal faults in thrust sheets: pre-orogenic extension, post-orogenic extension, or both? J. Struct. Geol. 21, 1011–1018.
ten Grotenhuis, S.M., Trouw, R.A.J., Passchier, C.W., 2003. Evolution of mica fish in mylonitic rocks. Tectonophysics 372, 1–21.
Tian, X., Buck, W.R., 2019. Lithospheric thickness of volcanic rifting margins: constraints from seaward dipping reflectors. J. Geophys. Res. Solid Earth 124. https://doi.org/10.1029/2018JB016733.
Tibaldi, A., Bonali, F.L., 2018. Contemporary recent extension and compression in the central Andes. J. Struct. Geol. 107, 73–92.
Tikoff, B., Fossen, H., 1993. Simultaneous pure and simple shear: the unifying deformation matrix. Tectonophysics 217, 267–283.
Tikoff, B., Teyssier, C., 1994. Strain modeling of displacement-field partitioning in transpressional orogens. J. Struct. Geol. 16, 1575–1588.
Tjia, H.D., 1964. Slickenslides and fault movements. Geol. Soc. Am. Bull. 75, 683–686.
Torvela, T., Mänttäri, I., Hermansson, T., 2008. Timing of deformation phases within the South Finland shear zone, SW Finland. Precambr. Res. 160, 277–298.
Tourigny, G., Schwerdtner, W.M., 1991. Metre-scale band structures and associated veins in Archean metavolcanics: aubelle gold mine, central Canada. J. Struct. Geol. 13, 913–918.
Treagus, S.H., 1983. A theory of finite strain variation through contrasting layers, and its bearing on cleavage refraction. In: Cobbold, P.R., Schwerdtner, W.M., Treagus, S.H. (Eds.), Strain Patterns in Rocks. Pergamon Press, Oxford, 9781483190624, pp. 351–368.
Trouw, R.A., Passchier, C.W., Wiersma, D.J., 2010. Atlas of Mylonites-And Related Microstructures. Springer Heidelberg, 978-3-642-03608-8pp. 322.
Turcotte, D., Schubert, G., 2014. Geodynamics, third ed. Cambridge University Press, Cambridge, 978-0521186230pp. 642.
Turner, J.P., Williams, G.A., 2004. Sedimentary basin inversion and intra-plate shortening. Earth Sci. Rev. 65, 277–304.
Twiss, R.J., Gefell, M.J., 1990. Curved slickenfibers: a new brittle shear sense indicator with application to a sheared serpentinite. J. Struct. Geol. 12, 471–481.
Twiss, R.J., Moores, E.M., 2007. Structural Geology, second ed. W. H. Freeman & Company, New York, 978-0716749516pp. 736.
Uliana, M.A., Arteaga, M.E., Legarreta, L., Cerdán, J.J., Peroni, G.O., 1995. Inversion structures and hydrocarbon occurrence in Argentina. In: In: Buchanan, J.G., Buchanan, P.G. (Eds.), Basin Inversion, vol 88. Geological Society of London Special

Publications, pp. 211–233.
Upreti, B.N., Le Fort, P., 1999. Lesser Himalayan crystalline nappes of Nepal: problem of their origin. In: In: Macfarlane, A., Quade, J., Sorkhabi, R. (Eds.), 328. Geological Society of America Special Paper, pp. 225–238.
Väisänen, M., Skyttä, P., 2007. Late Svecofennian shear zones in southwestern Finland. GFF 129, 55–64.
van der Wal, D., Vissers, R.L.M., Drury, M.R., Strating, E.H., 1992. Oblique fabrics in porphyroclastic Alpine-type peridotites: a shear-sense indicator for upper mantle flow. J. Struct. Geol. 14, 839–846.
van der Wal, D., Vissers, R.L., 1996. Structural petrology of the Ronda peridotite, SW Spain: deformation history. J. Petrol 37, 23–43.
Vannay, J.C., Sharp, Z.D., Grasemann, B., 1999. Himalayan inverted metamorphism constrained by oxygen isotope thermometry. Contrib. Mineral. Petrol. 137, 90–101.
Vannay, J.C., Grasemann, B., Rahn, M., Frank, W., Carter, A., Baudraz, V., Cosca, M., 2004. Miocene to Holocene exhumation of metamorphic crustal wedges in the NW Himalaya: evidence for tectonic extrusion coupled to fluvial erosion. Tectonics 23. https://doi.org/10.1029/2002TC001429.
Vejbæk, O.V., Andersen, C., 2002. Post mid-Cretaceous inversion tectonics in the Danish Central Graben–regionally synchronous tectonic events. Bull. Geol. Soc. Den. 49, 93–204.
Vermeer, P.A., De Borst, R., 1984. Non-associated plasticity for soils, concrete and rock. Heron 29, 1–64.
Vernon, R.H., 2018. A Practical Guide to Rock Microstructure, second ed. Cambridge University Press, 978-1108427241pp. 431.
Wallis, D., Parsons, A.J., Hansen, L.N., 2019. Quantifying geometrically necessary dislocations in quartz using HR-EBSD: application to chessboard subgrain boundaries. J. Struct. Geol. 125, 235–247.
Wang, Y., Zhou, L., Liu, S., Li, J., Yang, T., 2018. Post-cratonization deformation processes and tectonic evolution of the North China Craton. Earth-Sci. Rev. 177, 320–365.
Watkinson, I., Elders, C., Hall, R., 2008. The kinematic history of the khlong marui and ranong faults, southern Thailand. J. Struct. Geol. 30, 1554–1571.
Webb, A.A.G., Schmitt, A.K., He, D., Weigand, E.L., 2011. Structural and geochronological evidence for the leading edge of the Greater Himalayan Crystalline complex in the central Nepal Himalaya. Earth Planet. Sci. Lett. 304, 483–495.
Webster, R.E., Chebli, G.A., Fischer, J.F., 2004. General Levalle basin, Argentina: a frontier Lower Cretaceous rift basin. AAPG Bull. 88, 627–652.
Wennberg, O.P., 1996. Superimposed fabrics due to reversal of shear sense: an example from the Bergen Arc Shear Zone, western Norway. J. Struct. Geol. 18, 871–889.
Wernicke, B., Axen, G.J., 1988. On the role of isostasy in the evolution of normal fault systems. Geology 16, 848–851.
Wheeler, J., 1987. The determination of true shear senses from the deflection of passive markers in shear zones. J. Geol. Soc. 144, 73–77.
White, S.H., Bretan, P.G., Rutter, E.H., 1986. Fault-zone reactivation: kinematics and mechanisms. Phil. Trans. Roy. Soc. Lond. 317, 81–97.
Wiatr, T., Reicherter, K., Papanikolaou, I., Fernández-Steeger, T., Mason, J., 2013. Slip vector analysis with high resolution t-LiDAR scanning. Tectonophysics 608, 947–957.
Wibberley, C.A., McCaig, A.M., 2000. Quantifying orthoclase and albite muscovitisation sequences in fault zones. Chem. Geol. 165, 181–196.
Williams, G.D., Powell, C.M., Cooper, M.A., 1989. Geometry and kinematics of inversion tectonics. In: In: Cooper, M.A., Williams, G.D. (Eds.), Inversion Tectonics, vol 44. Geological Society of London Special Publications, pp. 3–15.
Winocur, D.A., Litvak, V.D., Ramos, V.A., 2015. Magmatic and tectonic evolution of the Oligocene Valle del Cura basin, main Andes of Argentina and Chile: evidence for generalized extension. In: In: Sepúlveda, S.A., Giambiagi, L.B., Moreiras, S.M., Pinto, L., Tunik, M., Hoke, G.D., Farías, M. (Eds.), Geodynamic Processes in the Andes of Central Chile and Argentina, vol 399. Geological Society of London Special Publications, pp. 109–130.
Wörner, G., Uhlig, D., Kohler, I., Seyfried, H., 2002. Evolution of the West Andean Escarpment at 18 S (N. Chile) during the last 25 Ma: uplift, erosion and collapse through time. Tectonophysics 345, 183–198.
Wong, T.F., David, C., Zhu, W., 1997. The transition from brittle faulting to cataclastic flow in porous sandstones: Mechanical deformation. J. Geophys. Res. Solid Earth 102, 3009–3025.
Xypolias, P., 2010. Vorticity analysis in shear zones: a review of methods and applications. J. Struct. Geol. 32, 2072–2092.
Xypolias, P., Koukouvelas, I.K., 2001. Kinematic vorticity and strain rate patterns associated with ductile extrusion in the Chelmos Shear Zone (External Hellenides, Greece). Tectonophysics 338, 59–77.
Xypolias, P., Spanos, D., Chatzaras, V., Kokkalas, S., Koukouvelas, I., 2010. Vorticity of flow in ductile thrust zones: examples from the Attico-Cycladic Massif (Internal Hellenides, Greece). In: In: Law, R.D., Butler, R.W.H., Holdsworth, R.E., Krabbendam, M., Strachan, R.A. (Eds.), Continental Tectonics and Mountain Building: the Legacy of Peach and Horne, vol 335. Geological Societyof London Special Publications, pp. 687–714.
Xypolias, P., Chatzaras, V., Beane, R., Papadopoulou, S., 2013. Heterogeneous constrictional deformation in a ductile shear zone resulting from the transposition of a lineation-parallel fold. J. Struct. Geol. 52, 44–59.
Yin, A., 2006. Cenozoic tectonic evolution of the Himalayan orogen as constrained by along-strike variation of structural geometry, exhumation history, and foreland sedimentation. Earth Sci. Rev. 76, 1–131.
Yin, A., Pappalardo, R.T., 2015. Gravitational spreading, bookshelf faulting, and tectonic evolution of the South Polar Terrain of Saturn's moon Enceladus. Icarus 260, 409–439.
Zhang, J., Cunningham, D., 2012. Kilometer-scale refolded folds caused by strike-slip reversal and intraplate shortening in the Beishan region, China. Tectonics 31. https://doi.org/10.1029/2011TC003050.
Zhang, Y., Hobbs, B.E., Ord, A., Mühlhaus, H.B., 1996. Computer simulation of single-layer buckling. J. Struct. Geol. 18, 643–655.
Zhang, J., Li, J., Ma, Z., Ren, W., 2011. Structural traces of secondary faults (fractures) along the main faults and their reliability as kinematic indicators. Acta Geol. Sin. Engl. Edn. 85, 1137–1149.
Zhao, S., Li, S., Li, X., Somerville, I., Cao, H., Liu, X., Wang, P., 2017. Structural analysis of ductile shear zones in the North Qinling Orogen and its implications for the evolution of the Proto-Tethys Ocean. Geol. J 52, 202–214.
Zhu, M., Graham, S., McHargue, T., 2009. The red river fault zone in the yinggehai basin, south China sea. Tectonophysics 476, 397–417.
Zoback, M.D., 2007. Reservoir Geomechanics. Cambridge University Press, New York, 978-0521146197pp. 340–377.
Zuza, A.V., Yin, A., 2016. Continental deformation accommodated by non-rigid passive bookshelf faulting: an example from the Cenozoic tectonic development of northern Tibet. Tectonophysics 677, 227–240.